A Study of Environment Noise in Ultra-Wideband Indoor Position Tracking

---

A Dissertation
Presented to
the Graduate School of
Clemson University

In Partial Fulfillment
of the Requirements for the Degree
Doctor of Philosophy
Electrical Engineering

---

by
William Charles Suski, II
May 2012

Accepted by:
Dr. Adam Hoover, Committee Chair
Dr. Richard Brooks
Dr. John Gowdy
Dr. Eric Muth

Abstract

This work is motivated by the problem of improving the accuracy of indoor ultra-wideband (UWB) position tracking through the study of the environment noise that affects such a system. Current systems can provide accuracy in the range of 30-100 cm in a small building, suitable for applications that require rough room-level precision such as asset tracking and surveillance. Our long-term goal is to improve the accuracy to 1 cm or better, expanding potential applications to telepresence, augmented reality, training and entertainment.

This work investigates the possibility of systematically observing the measurement noise of an UWB position tracking system and building a map of it throughout a facility. In order to understand the effect of environment noise on UWB indoor positioning and in turn filter out the effects of this noise, it is important to have an idea of what this measurement noise looks like in a real world scenario. In this work, an understanding of the measurement noise is gained by taking many measurements using a commercially-available UWB positioning system installed in a real world scenario and analyzing these measurements in various ways. To the author's knowledge, no one has used such an exhaustive approach to analyze measurement noise in UWB indoor positioning. The results of this work show that the measurement noise that affects a UWB indoor position tracking system can be effectively modeled using a weighted sum of Gaussians, is stable over time and is locally similar. Furthermore, a particle filter augmented with a measurement noise map is proposed to improve position tracking accuracy. Finally, a metric is proposed that can be used to quantify expected system performance based on sensor location, sensor orientation and facility floorplan. Using this metric, a procedure is developed to determine the parameters, i.e. sensor position, sensor orientation and potentially others, of the physical installation of the UWB tracking system that will produce minimum measurement error based on sensor geometry and physical facility constraints.

Acknowledgments

A number of people have made significant contributions to the completion of this dissertation in one way or another. First, I would like to sincerely thank my advisor, Dr. Adam Hoover, for the countless hours that he has spent brainstorming various ideas, reviewing and critiquing my writing and providing encouragement when things were not going as planned. Spending a few minutes discussing a problem with you always helped put my mind at ease. Second, I would be remiss if I did not mention the significant contributions to this work provided by Salil Banerjee. The hours that were spent collecting data, installing and re-installing various system components and collecting data again were certainly more enjoyable and efficient as a team than they would have been alone. I'd also like to thank the other members of my committee Dr. Richard Brooks, Dr. John Gowdy and Dr. Eric Muth for their time spent reviewing this document and providing valuable input. I'd also like to thank my parents, Bill and Mary Suski, for encouraging me to pursue this endeavor in the first place. Finally, I would like to thank my fiance, Kari Kertis, for her love, insight, willingness to put up with my late nights and countless hours spent watching me sit in front of a computer. If not for you, I would probably still be sitting in a cubicle in Maryland!

Table of Contents

List of Tables

Table **Page**

List of Figures

Figure **Page**

Chapter 1

Introduction

This work is motivated by the problem of improving the accuracy of indoor ultra-wideband (UWB) position tracking. Current systems can provide accuracy in the range of 30-100 cm in a small building [1], suitable for applications that require rough room-level precision such as asset tracking and surveillance. Our long-term goal is to improve the accuracy to 1 cm or better, expanding potential applications to telepresence, augmented reality, training and entertainment. This work is inspired by the methods that have been used to improve global navigation satellite system (GNSS) tracking accuracy over the past several decades [2]. The accuracy has improved from 100 m to better than 1 m which has expanded its original ship and airspace navigation applications to include civilian vehicle navigation and automated farming [3]. The methods used to improve accuracy include augmentations, such as differential and inertial systems [4], and systematic modeling of error sources such as atmospheric effects, timing jitter, and satellite constellation [5]. The Kalman filter and related signal processing approaches are typically used with error models to reduce the noise and improve the accuracy [4]. UWB indoor position tracking is a much newer technology but similar in operation a to GNSS, using many of the same principles such as trilateration. However, the scale of the problem (building-sized versus Earth-sized) affects the potential error sources in new and interesting ways. In this work, new noise models are developed for sources of error in a UWB indoor position tracking system and consider new augmentation methods. A variation on the particle filter is used to implement our ideas. Improved accuracy in position tracking is used to evaluate performance.

The following sections provide background on GNSS's, local positioning systems, UWB,

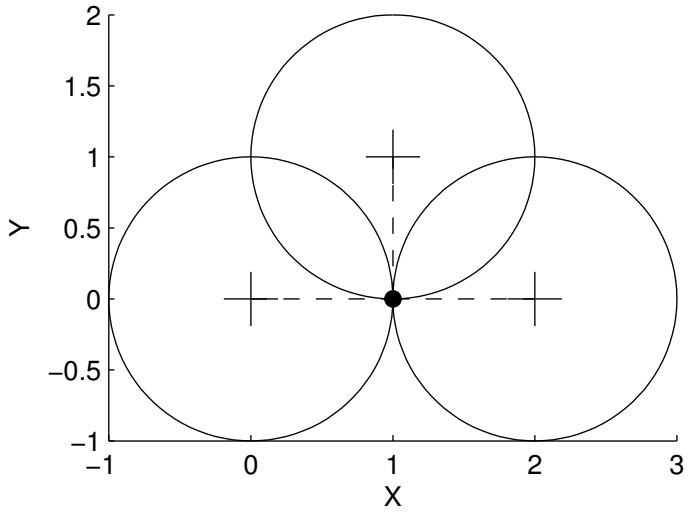

Figure 1.1: GNSS range calculation in two dimensions.

current UWB positioning work and the particle filter.

1.1 Global Positioning System

The Global Positioning System (GPS) is an active GNSS developed by the U.S. Department of Defense beginning in the 1970s. It is one of only two truly global satellite navigation systems, along with the Russian GLONASS system [3]. The basic idea behind a GNSS is that the range or distance from a transmitter to a receiver can be calculated by measuring the time that it takes for a radio frequency (RF) signal to propagate from transmitter to receiver and multiplying by the speed of light. Figure 1.1 shows this concept. A single range measurement places the receiver on a known circle (sphere in 3D) from the transmitter. Using several transmitters, the position of the receiver can be calculated by finding the intersection of the circles, a process called *trilateration*. There are several variations on this principle including time of arrival (TOA), time difference of arrival (TDOA) and angle of arrival (AOA). Each of these varies somewhat in how the range is calculated, but the overall principle is the same.

There are many sources of noise in the GPS, including geometric satellite positions, clock errors, ephemeris errors, atmospheric distortion and multipath [3]. Each of these affects the accuracy of range measurements, thus affecting the accuracy of the trilateration. For example, multipath errors can cause a reflection to be detected instead of the direct path and therefore incorrectly

estimate the time of flight. This leads to an increased range estimate which results in errors in the trilateration calculation. In the modern GPS, these noise sources are modeled and filtered to improve the accuracy of the calculated position [6].

Several augmentation methods have also been combined with GPS to improve its accuracy. An augmentation method brings other sources of information into the range calculation. For example, differential GPS uses a local (to the receiver), Earthbound tower that has a more expensive, more precise clock than the receiver, to obtain another distance measurement [6]. It is assumed that the tower's position has been carefully surveyed and is known more precisely than its GPS estimate. Together, these sources of information can be used to improve the position accuracy. The Wide Area Augmentation System (WAAS) uses a ground-based segment to correct for errors in GPS signals and transmits that information to capable GPS receivers via geostationary satellites [6]. A simpler example is in place in modern vehicle navigation systems. These systems incorporate road maps and positions calculated by pure GPS are filtered or map-matched towards the nearest road location [7, 8, 9].

1.2 Local Positioning Systems

A local positioning system (LPS) is similar in principle to a GNSS but is intended to work in a building-sized area. The GPS and other GNSSs do not transmit with enough power to penetrate inside buildings, so an LPS is intended to provide a similar capability in GPS-denied areas. One requirement of an LPS system is that it must broadcast a signal that can penetrate through interior walls, furniture, and the standard clutter of a building in such a way that accurate range calculations and, in turn, trilateration is possible. Installation of such a system can be a challenge because sensors must be mounted and cables run taking into consideration security, convenience of placement, coverage area and precise determination of sensor positions. This task can be especially difficult in older structures.

Several different technologies have been explored for LPSs including augmented GPS, RFID, cellular-based systems, UWB, wireless local area networks (WLAN), Bluetooth, proprietary ultra high frequency solutions and infrared [10]. Other methods include camera-based systems, ultrasound and laser-based systems [11]. Inertial navigation systems are also used in LPSs [12]. Although GPS is the predominant positioning technology today, this work is focused on systems that function

indoors. Regular GPS signals do not penetrate external walls well and are therefore unsuitable for this type of application. Also, technologies such as RFID, Bluetooth, infrared, ultrasound and laser-based systems do not have the range required to cover an entire building or even an entire floor of a building. Therefore, this work does not focus on these types of systems.

1.3 Ultra-Wideband

Our work makes use of an ultra-wideband (UWB) LPS. This technology has shown the most promise towards meeting the challenges of indoor position tracking, including ease of installation, functional range and potential accuracy.

UWB generally refers to a very short RF pulse which distributes signal power across a wide range of frequencies. The United States Federal Communications Commission began permitting the use of UWB systems in 2002 [13]. Their rules require that UWB systems not disrupt other wireless systems and therefore a strict power limit is in place. UWB has been researched or is being developed for several applications including communications, RADAR, imaging and sensor network systems [14]. This work is only concerned with the application of UWB to indoor position tracking. UWB is ideally suited to indoor position tracking because of its wide bandwidth and short duration. Compared to a traditional narrowband RF signal, it is more likely that some portion of a UWB signal's transmitted spectrum will pass through all obstacles between the transmitter and receiver with minimum attenuation and delay [15]. Furthermore, the short duration of a UWB pulse provides good time resolution which minimizes the effects of multipath interference [16] and allows for high-resolution ranging [15]. Once a signal is detected, the receiver is challenged with processing the received pulse in order to measure precise signal time-of-flight. An accurate range estimate to the transmitter can be determined by multiplying the time-of-flight by the speed of light. With multiple range estimates to the transmitter, trilateration calculations can be made in a manner similar to those performed by GPS.

1.4 UWB Indoor Position Tracking Systems

Since accuracy is our motivating factor, this section overviews related work in terms of position tracking accuracy and evaluation. Additional technical aspects of the works are discussed

Table 1.1: UWB local positioning system comparison table. The abbreviation "Comm." denotes commercial systems.

	System	Test Range	Accuracy	Measurements	Noise
Comm.	Ubisense [17]	-	15 - 30 cm	-	-
	Dart [18]	-	<30 cm	-	-
	Plus [19]	-	<1 m	-	-
	Thales [20]	-	<1 m	-	-
Research	Mahfouz, et al. [21]	<1 m ?	1 - 43 mm	-	[2,3,4,5,6]
	Zhang, et al. [22]	7 x 4 x 1 cm	2 - 6 mm	5,000 - 6,000	[2,3,4,5,6]
	Yang, et al. [23]	<1 m ?	<30 mm	~ 2,000	[2,3,4,5]
	Low, et al. [24]	4 - 24 m	1 - 4 cm	167	[2,3,5]
	Yan, et al. [25]	2 - 15 m	2 - 18 cm	400	[2,3,4,5]
	Fontana, et al. [26]	~ 30 x 13 m	<31 cm	7,883	All
	Guoping and Rao [27]	5 × 6 m	>30 cm	~ 40,000	[2,3,4,5,6]
	Waldmann, et al. [28, 29]	<2.5 m	3 cm	-	[2,3,4,5,6]
	Correal, et al. [30]	20 x 20 x 6 m	2 - 38 cm	3,000	[2,3,4,5]
	Zetik, et al. [31]	0.02 cm - 4 m	0.4 - 0.8 mm	200 - 300	[2,3,4,5]
	Meier, et al. [32]	2 x 2 x 2 m	<1 mm	-	[2,3,4,5]
	Oh, et al. [33]	~ 8 × 8 m	<30 cm	300 - 400	[2,3,4,5]
	MacGougan, et al. [34]	35 x 43 m	<10 cm	-	[3,4,5]
	Steiner and Wittneben [35]	7 x 15 m	43 - 93 cm	~ 14,000	[2,4]
Simulation	Denis, et al. [36]	16 x 16 m	27 - 74 cm	-	[1,2,3,5]
	Jing, et al. [37]	-	<4 cm	-	[1,5]
	Chung and Ha [38]	10 m	<6 m	-	[2,5]
	Shen, et al. [39]	300 x 300 cm	2 - 300 cm	-	[1,3,6]
	Morelli, et al. [40]	40 x 30 m	-	-	[1,5]
	Yu and Oppermann [41]	40 x 30 x 5 m	<3 m	-	[3,5,6]

[1] non-line-of-sight (NLOS)
[2] multipath
[3] synchronization
[4] antenna effects
[5] peak detection
[6] sensor placement

here and in subsequent chapters in this dissertation. The goal of this section is to give the reader an overview of the current state of the art.

The current state of UWB indoor position tracking works is summarized in Table 1.1. Reported system accuracies range from less than 1 mm to greater than 5 m, a span of more than three orders of magnitude. Obviously, these evaluations were performed under different conditions, but the plethora of results is not easily interpreted. For many works, numerical accuracy is reported but the testing conditions are vague or unreported. Details such as the size of the test area or the environmental conditions are sometimes absent. In some cases, repeatability metrics are reported instead of accuracies, which adds to the complexity in the literature.

For commercial systems, reported accuracies range from 15 cm to 1 m by the companies selling them [20, 19, 17, 18]. The methods by which these numbers were measured are unavailable. Since the motivating factor is sales, a simple estimate of performance (e.g., a single number) is

generally all that is given. Perhaps recognizing the ambiguity of the issue, many performance estimates use a qualifying phrase such as "better than 30 cm" (denoted by the $<$ symbol). However, it is not clear if this provides a maximum bound on error, or if it is an estimate of average error, or has some other meaning.

Research systems are often constructed in order to test the effect of a particular condition or noise source upon accuracy. For example, Mahfouz, et al. [21] studied the effects of sampling rate limitations, iterative receiver-side peak detection, component timing synchronization, antenna phase-center variation, and base station configuration. Tests were performed using a custom system over a small (1 - 2 m) unobstructed area in order to isolate the impact of each condition. Precise (less than 1 mm) ground truth positions were established using a commercial optical tracking system. Depending on the conditions, average errors as low as 1 mm were obtained. Further research, reported in [22], decreased system complexity and focused on a noise source referred to as the "shoulder" effect. RMS errors between 2 and 6 mm were reported for three-dimensional tracking. Related research in [23] reported errors less than 30 mm using a selective correlation algorithm. While these tests are encouraging and show the ultimate accuracy that may be obtainable with UWB tracking, they are not indicative of the actual accuracies obtainable for building-wide applications today.

Low, et al. [24] developed an algorithm to improve the calculation of the time-of-flight using a combination match filtering and peak search technique. This algorithm reduces the impact of inter-symbol interference and multipath on the range calculation. The technique was tested in line-of-sight (LOS) conditions across six different environments including large, open spaces and small, dense office spaces. In each environment, measurements were made at 20 - 36 locations and mean errors from 0.5 to 4 cm were reported. This evaluation considers realistic environments to encourage multipath errors, but ignores NLOS errors which can create large positive biases in the range measurements.

Many research works focus on developing a proof-of-concept system, such as to meet some specification. Fontana, et al. [26] presented an FCC approved, UWB position tracking system. The system was evaluated in both indoor and outdoor environments with the bulk of the evaluation being performed in a 30 $\times$ 15 m laboratory area including NLOS and multipath error sources. The outdoor experiment tested operating range only and reported a range as far as 183 m. In the reported indoor experiment, 7,883 position estimates were collected over 2.2 hours at a single tag location. The authors reported an accuracy of less than 30 cm. This evaluation shows that a

position tracking system can be developed that meets FCC requirements for UWB signals. While this proof-of-concept evaluation was performed in a realistic environment, the reported results do not acknowledge the vast differences in tracking accuracy that occur in different locations across a typical indoor facility.

Another FCC compliant UWB localization system was described in [27]. The goal of this work is to develop a low-cost UWB localization system by performing parallel edge detection, using a 1-bit sampler and determining position from time-difference of arrival (TDOA) values using simpler calculations. The evaluation considered stationary and moving tags within a 5 $\times$ 6 m facility in multipath conditions. LOS/NLOS conditions are not reported. The authors report approximately 30 cm two-dimensional error for certain locations within the facility but much greater error when further from the UWB sensors. Only three sensors are employed in the evaluation.

An UWB localization system was developed based on short pulses of frequency modulated continuous wave (FMCW) signals in [28] and a short multipath mitigation technique is added to the system in [29]. The system has a maximum operating range of 20 m. The evaluation took place in a 5 $\times$ 3.5 m laboratory under LOS conditions. One-dimensional measurements were taken by the system in 5 cm increments over a 2.5 m range. An average ranging error of about 3 cm is reported. This evaluation is quite small, does not consider NLOS conditions and only considers one-dimensional positioning. Short multipath is mitigated using a feed-forward neural network, but only simulation results are reported for this technique.

Correal, et al. [30] developed and evaluated a system for performing UWB positioning based on relative location. This system uses pair-wise range measurements to add information from neighboring transmitters with unknown location to the classical positioning problem. The experimental evaluation was performed in an office area (10 x 11 m) in LOS conditions. 500 point-to-point range measurements were collected at 6 locations within the facility. The authors report errors in the 2 - 38 cm range. This measurement campaign, while somewhat realistic, is small and does not take into account the significant effects of NLOS conditions.

Using a UWB system that transmits long spreading sequences instead of short pulses, Zetik, et al. [31] examined one-dimensional range resolution as well as two and three dimensional positioning accuracy. The range resolution was tested under ideal conditions by connecting the transmitter and receiver to a mechanical delay line. The two dimensional positioning experiment was performed over a 2 $\times$ 4 m area without any obstacles, e.g. walls, people, etc. Furthermore, the transmitter

and receiver elements were synchronized avoiding most synchronization error. The tag traversed a specific path and position estimates were made along the way. While no true error measurement is reported, the experiments are reported to be repeatable with a standard deviation of just 1.5 cm in both directions. Although multipath conditions likely existed in the test environment, NLOS conditions were not considered. Also, the coverage area of the system was limited when compared to real-world applications.

Another system employing spreading sequences was developed by Meier, et al. [32]. This prototype system contains three receivers and a single transmitter and was evaluated in a laboratory under LOS conditions. The evaluation is mainly proof-of-concept for three-dimensional positioning. A Kalman filter is used to improve the performance and achieve errors in the sub-millimeter range.

The IEEE released the 802.15.4a IR-UWB physical layer specification in March of 2007. This specification describes a low data rate communication and ranging/positioning system. Oh, et al. in [33] developed a coherent IR-UWB system that meets this specification. The system was evaluated for one-dimensional positioning in a hallway at ten distances from 1 to 19 m. Average ranging errors from 1 to 20 cm were reported for 5000 measurements at each distance. Two-dimensional positioning results were also evaluated. 300 measurements were recorded by four reference nodes with the mobile node (tag) in a single location. Position error of less than 30 cm was reported for this experiment.

MacGougan, et al. [34] combined GPS with a UWB positioning system to demonstrate improvements in GPS positioning accuracy when in urban canyons or deep mines with degraded satellite coverage. An extended Kalman filter was used to track a number of GPS and UWB parameters including bias and scale factors for each UWB receiver. The UWB system was placed in an outdoor environment covering an area approximately 35 $\times$ 43 m with LOS conditions. Both static and dynamic tests were performed. In the static test, the GPS+UWB system was placed at a specific known location within the area covered by three UWB receivers and data was collected for four minutes with both good and artificially degraded satellite coverage. The authors reported horizontal RMS errors between 14 and 24 mm and vertical RMS errors between 25 and 279 mm. In the dynamic test, the system traverses a path in both good and artificially degraded GPS conditions. The good GPS condition portion of the test is used to determine UWB and bias scale conditions. The authors report errors better than 10 cm for most of the kinematic testing with the GPS+UWB system under degraded GPS conditions. The GPS-only system was unable to produce a solution

under these conditions.

Yan, et al. in [25] propose a framework for determining location using a least-squares technique. They transform the three-dimensional localization problem into a one-dimensional problem and solve it iteratively. The experimental data used in this work is a set of 400 UWB range measurements collected under LOS conditions at distances from 2 to 15 m. The ground truth information for the positions was determined using a laser tool. RMS errors between 2 and 18 cm are reported. The authors achieved a reduction in computations of approximately 67% using their method when compared to classical non-linear least squares methods.

Position estimation based on location fingerprinting is an area of research that has received significant attention. This positioning method assumes that each location within a facility has a unique set of observable values that can be used to determine the location of a sensor based on these observed values. Steiner and Wittneben consider this type of indoor positioning method in [35] using an UWB energy detection receiver. The evaluation covered 22, 27 $\times$ 56 cm regions within a 7 $\times$ 15 m indoor environment. The positioning accuracy is determined through simulation using real UWB channel measurements. The evaluation considered position accuracy based on number of training vectors, sampling frequency and number of regions included. This method is quite different from previous positioning methods considered. However, such methods would benefit from a larger measurement campaign than was reported in [35].

Bayesian filtering techniques, such as the Kalman or particle filter, have been used extensively for UWB tracking in indoor environments. Denis, et al. [36] applied two different Bayesian filters to simulated data based on a deterministic UWB propagation model. The goal of this work was to track time-of-arrival (TOA) biases created by NLOS conditions and use these biases to improve tracking accuracy. The model was able to achieve error less than 0.5 m in a two-dimensional tracking simulation. These techniques show promise but have not been proven in real-world scenarios.

Jing, et al. [37] considered waveform distortion caused by UWB signals passing through various materials. The goal was to focus on the bias error caused by incorrect peak detection due to the distortion cause by NLOS conditions. They evaluated the effects of this type of noise by simulating the effects of different materials and material thicknesses. These simulations isolate NLOS noise sources, but similar experimental work is needed.

Chung, et al. [38] developed and reported results from another simulated ranging, i.e. one-dimensional positioning, system. This simulation focused on improving TOA estimation using a train

of UWB pulses instead of just one. The UWB system itself was modeled using a known indoor UWB channel model, transmitter and receiver. The authors performed ten experiments containing 1000 pulses for averaging over a 10 m distance and reported errors less than 6 m. Again, this evaluation focuses on improving a single error source and does not address the real-world positioning problem.

A method for determining whether a measurement from a receiver is LOS or NLOS is proposed in [39]. The simulated results are based on randomly placing receivers or reference nodes in a simulated facility 1000 times and determining the RMS location errors. The authors report errors between 2 and 300 cm. This evaluation focuses on the detection of NLOS nodes, but simulates its results. Real-world scenarios would likely provide different results.

Another method for tracking LOS and NLOS conditions as well as determining tag location was developed in [40]. This work uses hidden Markov models to estimate both position and LOS/NLOS condition. Simulations are run considering ranging only as well as a two-dimensional real-world positioning scenario. The authors included NLOS conditions due to walls and multipath effects into the simulations. Specific error values are not reported, but maps are shown that give an idea of the distribution of errors for comparison between positioning techniques.

A comparison of two position calculation methods is considered in [41]. The first method directly calculates the tag position using TDOA measurements which produces two possible solutions, one of which is typically unreasonable. The second method minimizes an objective function of squared range errors to produce an optimal position estimate. This method iteratively produces a single solution. The authors simulated the placement of four and five sensors within a $40 \times 30 \times 5$ m facility. Zero mean, Gaussian distributed noise is added to TOA values to evaluate the performance of the two methods. Error values between 0.25 and 3 m are reported.

Based on the preceding summaries, it can be seen that the literature regarding UWB positioning contains a wide array of systems, evaluation techniques and reported accuracies. Each work contains an evaluation of system accuracy under specific conditions. Some focus on isolating and mitigating a single noise source while others are more proof-of-concept oriented. In general, this work is different from others in that it is motivated by how the error sources can be modeled and filtered in practice. The natural clutter of an indoor environment is not avoided, and NLOS distortions and multipath errors are expected. Overall measurement noise is an aggregate of all of the sources of error that affect a system. In the case of positioning systems, it is the noise that affects the final position estimate generated by the system. This is different from noise on a single

range measurement because that noise has now been propagated through to position estimation.

1.5 Filtering

Filtering is the process of estimating the unknown state of a system from a set of noisy measurements or observations and the system's dynamic model. A system's state and dynamic model can be made up of any number of variables and is in no way limited to position and velocity information. It can be used to estimate the past, present and future states of a dynamic system [42]. The following sections describe the various components of filtering along with the Kalman filter, recursive Bayesian estimation and the particle filter.

1.5.1 State Space Approach

The state space approach to filtering estimates variables of interest along with their covariances. For example, if one were tracking two-dimensional position and velocity, the state vector $\mathbf{x}_t$ gives the best estimate of position and velocity at time t and is written as shown in Equation 1.1 where x_t and y_t represent the objects position and $\dot{x}_t$ and $\dot{y}_t$ represent the objects velocity at time t. Note that state variables are traditionally represented as a vector.

$$\mathbf{x}_t = \begin{bmatrix} x_t \\ \dot{x}_t \\ y_t \\ \dot{y}_t \end{bmatrix} \tag{1.1}$$

In the state space approach, the variables of interest are always assumed to lie on a distribution, rather than at a specific value. This allows for the representation of uncertainty about their values. This uncertainty is represented by covariance matrices which will be described later.

1.5.2 State Transition Equations

State transition equations describe the expected behavior of the system over a period of time from t to $t+1$. These equations must be first order Markovian, i.e. the set of next possible states must be dependent only upon the current state. For example, Equation 1.2 gives the function $\mathbf{f}(\cdot)$ that governs state transitions for a two-dimensional constant velocity model where T is the sensing

interval and $\mathbf{w}$ is a normally distributed random vector with zero mean and covariance matrix Q shown in Equation 1.3 where σ_x^2 and σ_y^2 are the variances in x and y and σ_{xy}^2 is the cross correlation.

$$\mathbf{f}(\mathbf{x}_t, \mathbf{w}_t) = \begin{bmatrix} x_{t+1} = x_t + T \cdot \dot{x}_t \\ \dot{x}_{t+1} = \dot{x}_t + w_{x,t} \\ y_{t+1} = y_t + T \cdot \dot{y}_t \\ \dot{y}_{t+1} = \dot{y}_t + w_{y,t} \end{bmatrix} \tag{1.2}$$

$$Q = \begin{bmatrix} 0 & 0 & 0 & 0 \\ 0 & \sigma_x^2 & 0 & \sigma_{xy}^2 \\ 0 & 0 & 0 & 0 \\ 0 & \sigma_{xy}^2 & 0 & \sigma_y^2 \end{bmatrix} \tag{1.3}$$

These equations can also be represented in matrix notation as shown in Equation 1.4 where A is the state transition matrix shown in Equation 1.5 and $\mathbf{w}_t$ is as shown in Equation 1.6.

$$\mathbf{f}(\mathbf{x}_t, \mathbf{w}_t) = \begin{bmatrix} \mathbf{x}_{t+1} = A\mathbf{x}_t + \mathbf{w}_t \end{bmatrix} \tag{1.4}$$

$$A = \begin{bmatrix} 1 & T & 0 & 0 \\ 0 & 1 & 0 & 0 \\ 0 & 0 & 1 & T \\ 0 & 0 & 0 & 1 \end{bmatrix} \tag{1.5}$$

$$\mathbf{w}_t = \begin{bmatrix} 0 \\ w_{x,t} \\ 0 \\ w_{y,t} \end{bmatrix} \tag{1.6}$$

Dynamic noise allows for changes to the dynamics of the system. In the case of a constant velocity model, the dynamic noise acts upon the velocity creating non-zero acceleration.

1.5.3 Observation Equations

The observation equations are used to describe the portion of the state that can be observed. Let's say that two-dimensional position is the only portion of the state that the system can observe, then the observation equations would be described by the function $\mathbf{g}(\cdot)$ shown in Equation 1.7 where $\mathbf{z}_t$ is the 2×1 observation vector and $\boldsymbol{\nu}_t$ is the 2×1 observation noise vector.

$$\mathbf{g}(\mathbf{x}_t, \boldsymbol{\nu}_t) = \begin{bmatrix} z_{x,t+1} = x_t + \nu_{x,t} \\ z_{y,t+1} = y_t + \nu_{y,t} \end{bmatrix} \tag{1.7}$$

These equations can also be represented in matrix notation as shown in Equation 1.8 where H is the observation matrix shown in Equation 1.9 and $\boldsymbol{\nu}_t$ is the vector shown by Equation 1.10.

$$\mathbf{g}(\mathbf{x}_t, \boldsymbol{\nu}_t) = \begin{bmatrix} \mathbf{z}_{t+1} = H\mathbf{x}_t + \boldsymbol{\nu}_t \end{bmatrix} \tag{1.8}$$

$$H = \begin{bmatrix} 1 & 0 & 0 & 0 \\ 0 & 0 & 1 & 0 \end{bmatrix} \tag{1.9}$$

$$\boldsymbol{\nu}_t = \begin{bmatrix} \nu_{x,t} \\ \nu_{y,t} \end{bmatrix} \tag{1.10}$$

In this example, the observation noise corrupts the true position (x_t, y_t) additively. The observation noise vector $\boldsymbol{\nu}_t$ is a sample from a two-dimensional Gaussian random variable with covariance matrix R as shown in Equation 1.11.

$$R = \begin{bmatrix} \sigma^2_{\nu_x} & \sigma^2_{\nu_{xy}} \\ \sigma^2_{\nu_{xy}} & \sigma^2_{\nu_y} \end{bmatrix} \tag{1.11}$$

1.5.4 Kalman Filter

Applying the Kalman filter [43] to a set of measurement data is an iterative process. An iteration occurs for each piece of measurement data available and each iteration has five steps. First, the Kalman gain matrix is calculated using Equation 1.12, where P_t^- is the predicted state covariance matrix from the previous iteration, H is the observation matrix and R is the observation

noise covariance matrix.

$$K_t = P_t^- H^T (H P_t^- H^T + R)^{-1} \tag{1.12}$$

Next, the outputs are calculated as part of the update phase. The outputs include the current state at time t, $\hat{\mathbf{x}}_t$, and the predictor covariance, P_t. Equation 1.13 shows the update equation for the current state, where $\mathbf{z}_t$ is the newest measurement and $\hat{\mathbf{x}}_t^-$ is the predicted state from the previous iteration.

$$\hat{\mathbf{x}}_t = \hat{\mathbf{x}}_t^- + K_t(\mathbf{z}_t - H_t \hat{\mathbf{x}}_t^-) \tag{1.13}$$

The state update equation gives an idea of how the Kalman filter behaves in practice. $(\mathbf{z}_t - H_t \hat{\mathbf{x}}_t^-)$ is the measurement *innovation* or the residual. This gives the difference between the estimated measurement and the actual measurement. Therefore, the Kalman gain K_t weights the residual. As the measurement error covariance R goes to zero, K_t goes towards H^{-1} and the filter trusts the measurement more. On the other hand, as the a priori predictor covariance P_t^- goes to zero, K_t also goes to zero and the filter trusts the state estimate more [44]. The predictor covariance is updated using Equation 1.14, where I is the identity matrix.

$$P_t = (I - K_t H) P_t^- \tag{1.14}$$

Finally, the predictions for the next measurement are calculated. These matrices will be used to calculate the gain, state and predictor covariances in the next iteration. The next predicted state, $\hat{\mathbf{x}}_t^-$, is calculated using Equation 1.15, where A is the state transition matrix based on the state transition equations $\mathbf{f}(\cdot)$ of the dynamic model.

$$\hat{\mathbf{x}}_t^- = A \hat{\mathbf{x}}_{t-1} \tag{1.15}$$

The next predictor covariance is calculated using Equation 1.16, where Q is the dynamic noise matrix.

$$P_t^- = A P_{t-1} A^T + Q \tag{1.16}$$

These equations comprise one iteration through the Kalman filtering process. After these calculations, all of the time variables are incremented by one and the process is repeated.

The Kalman filter calculates the optimal state only when the state transition and observation equations are linear and the dynamic and measurement noise is normally distributed. The extended Kalman filter (EKF) allows for non-linear state transition and observation by linearizing the problem using Jacobian matrices [42]. The Jacobians are calculated at each time step.

The unscented transform [45] is an improvement on the EKF that calculates sigma points from the state and covariance matrices, transforming them through the state transition equations and then rebuilding the state and covariance matrices.

The Kalman filter is only intended for linear systems. The EKF and unscented transform work on non-linear systems. However, all three assume Gaussian state and observation distributions. These methods all break down if the distributions are not Gaussian or if they are intractable. In these cases, a more general theory that applies to generic distributions is necessary.

1.5.5 Recursive Bayesian Estimation

Recursive Bayesian estimation can be written using Bayes rule as shown in Equation 1.17.

$$p(\mathbf{x}_{0:t}|\mathbf{z}_{0:t}) = \frac{p(\mathbf{x}_t|\mathbf{x}_{t-1})p(\mathbf{z}_t|\mathbf{x}_t)}{p(\mathbf{z}_t|\mathbf{z}_{0:t-1})}p(\mathbf{x}_{0:t-1}|\mathbf{z}_{0:t-1}) \tag{1.17}$$

This equation is applicable for any distribution but is easily handled for the case of Gaussian distributions due to the multiplications of exponentials. It is also worth noting that recursive Bayesian estimation defaults to the Kalman filter for Gaussian distributions.

1.5.6 Particle Filter

The particle filter [46] is a Monte Carlo approximation to Equation 1.17. Approximation is necessary because often the distributions are intractable or difficult to deal with analytically. Therefore, the distributions are instead modeled using a set of weighted states referred to as particles. The weight of each particle describes the accuracy of the "guess."

1.5.7 Basic Particle Filter Algorithm

The basic particle filter (BPF) approximates complex distributions using a set of particles. A set of particles is a collection of M state space variables with a weight assigned to each. A distribution is approximated by a set of particles χ, shown in Equation 1.18, where M is the number of particles, $\mathbf{x}_t^m$ is the state of particle m and w_t^m is the weight assigned to particle m, both at time t.

$$\chi = \{\mathbf{x}_t^m, w_t^m\}_{m=1}^M \tag{1.18}$$

The particle states are updated according to the state transition equation $\mathbf{f}$ as shown in Equation 1.2. Sequential importance sampling is used with the prior importance function [46] which gives the weight update function shown in Equation 1.19 where w_{t-1}^m is the weight of particle m at time $t-1$ and $p(\mathbf{z}_t|\mathbf{x}_t^m)$ is the probability of the measurement $\mathbf{z}_t$ given the state of particle m, all at time t.

$$w_t^m = w_{t-1}^m \cdot p(\mathbf{z}_t|\mathbf{x}_t^m) \tag{1.19}$$

A two-dimensional normal distribution with mean at $\mathbf{x}_t$ and covariance matrix, Σ_n, is used as the measurement noise model and is calculated as shown in Equation 1.20.

$$p(\mathbf{z}_t|\mathbf{x}_t^m) = \frac{1}{2\pi\sqrt{|\Sigma_n|}} e^{-\frac{1}{2}(\mathbf{z}_t - \boldsymbol{\mu}_{\mathbf{x}_t^m})^T \Sigma_n^{-1} (\mathbf{z}_t - \boldsymbol{\mu}_{\mathbf{x}_t^m})} \tag{1.20}$$

Next, the particle weights are normalized and the expected value is computed using Equations 1.21 and 1.22 respectively. Finally, the coefficient of variation (CV) and effective sample size (ESS) are computed [47] and resampling is performed if necessary. The sampling method that has been chosen is referred to as "select with replacement" by Rekleitis in [48].

$$w_t^m = \frac{w_t^m}{\sum_{\hat{m}=1}^M w_t^{\hat{m}}} \tag{1.21}$$

$$E(\mathbf{x}_t) = \sum_{m=1}^M w_t^m \cdot \mathbf{x}_t^m \tag{1.22}$$

The CV and ESS are calculated according to Equations 1.23 and 1.24. Throughout this

work, resampling is performed when the ESS is determined to be less than $0.5 \times M$, i.e. half of the particles' weights have gone to zero.

$$ESS = \frac{M}{1 + CV} \tag{1.23}$$

$$CV = \frac{1}{M} \sum_{m=1}^{M} \left(M \cdot w_t^m - 1 \right)^2 \tag{1.24}$$

The particle filter is applicable to problems with linear or non-linear state and observation equations, as well as any dynamic and observation noise distributions.

1.5.8 Particle Filter Example

This section describes a simulated system where the one-dimensional position of a magnet is to be estimated from a noisy magnetic field strength sensor.

1.5.8.1 Simulated System

The simulated system consists of two magnets of equal strength, a field strength sensor and a clothesline. The sensor is attached to the clothesline and can be moved in the x direction from $-x_{max}$ to x_{max}. The magnets, m_1 and m_2, are fixed at x_{m_1} and x_{m_2} respectively. The layout of each of the elements of the system is shown in Figure 1.2.

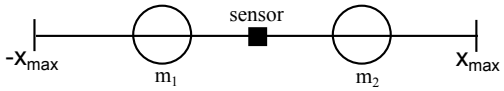

Figure 1.2: Diagram of the simulated system.

The sensor moves along the clothesline over time according to the dynamic model shown in Equations 1.25 and 1.26 where x_t is the position of the sensor, $\dot{x}_t$ is the sensor velocity, T is the time between measurements, $U(-\dot{x}_{max}, \dot{x}_{max})$ is a uniformly distributed random variable between $-\dot{x}_{max}$ and $\dot{x}_{max}$, t_l is the low threshold and t_h is the high threshold. The low threshold is used to slow the sensor down as it approaches $|x_{max}|$ and the high threshold reverses the direction of the

velocity when the sensor is very close to $|x_{max}|$.

$$x_t = x_{t-1} + \dot{x}_t T \tag{1.25}$$

$$\dot{x}_{t+1} = \begin{cases} \dot{x}_t + U(-\dot{x}_{max}, \dot{x}_{max}) & |x_t| < t_l \\ 0.9 \cdot \dot{x}_t & t_l \leq |x_t| < t_h \\ -\dot{x}_t & |x_t| \geq t_h \end{cases} \tag{1.26}$$

The output of the simulated system is a set of sensor location values, x_t, for $t = 0 : 199$. A plot of these values can be seen in Figure 1.3. In this plot, $x_0 = 0$, $\dot{x}_0 = 0$ and $x_{max} = 200$. The time between measurements, T, is considered to be $1\,s$. The maximum velocity allowed, $\dot{x}_{max}$, is set to 5 and t_l and t_h are $0.5 \cdot x_{max} = 100$ and $0.9 \cdot x_{max} = 180$ respectively. The magnets are located at $x_{m_1} = -100$ and $x_{m_2} = 100$.

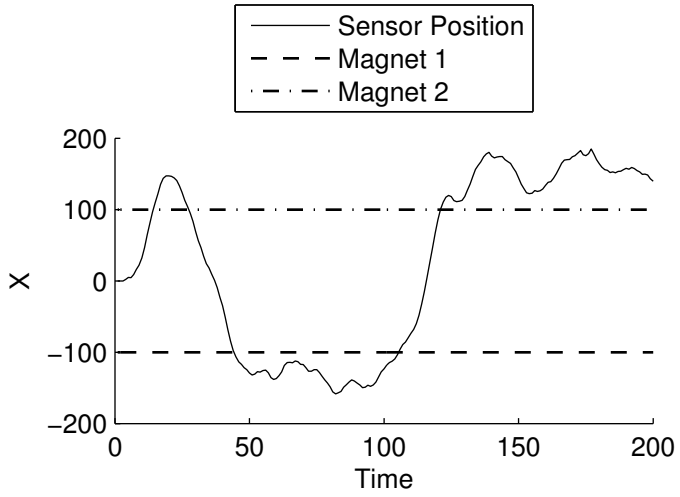

Figure 1.3: Plot of the sensor location over time.

1.5.8.2 Simulated Sensor

A simulated sensor was developed to take measurements of the field strength present at the current location of the sensor. The field strength is determined by summing the values of two different Gaussian probability density functions (PDFs) each associated with a particular magnet. Equation 1.27 shows the PDFs used to calculate the field strength where x_{m_i} is the location of the

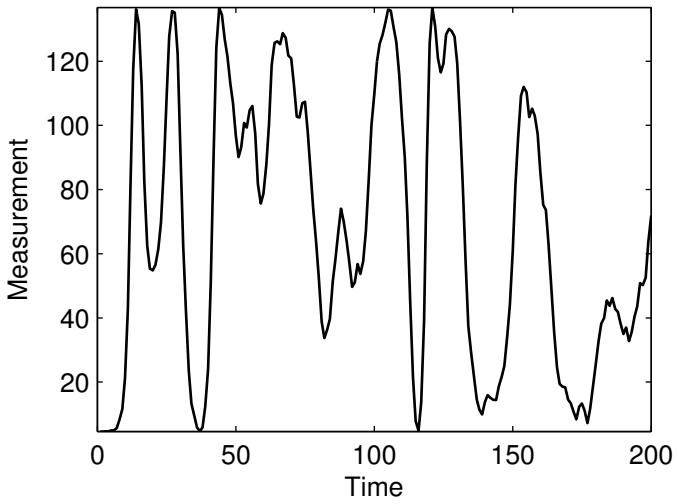

Figure 1.4: Plot of the measurements returned by the field strength sensor based on the sensor trajectory shown in Figure 1.3 without measurement noise.

magnet and σ_m is the standard deviation.

$$f(x_t|\mu_i, \sigma_m) = \frac{1}{\sqrt{2\pi\sigma_m^2}} e^{\frac{-(x_t - x_{m_i})^2}{2\sigma_m^2}}, \ i = 1, 2 \tag{1.27}$$

Using Equation 1.27, each sensor measurement, y_t, is calculated according to Equation 1.28, where $N(0, \sigma_s)$ is a zero-mean Gaussian distributed random variable with standard deviation σ_s. The multiplier of 5000 is used to increase the size of the measurements to avoid values that are too close to zero and the random variable is added to simulate measurement noise generated by the sensor.

$$y_t = 5000 \cdot [f(x_t|\mu_1, \sigma_m) + f(x_t|\mu_2, \sigma_m)] + N(0, \sigma_s) \tag{1.28}$$

Figure 1.4 shows the measurements generated by the simulated sensor for the sensor path shown in Figure 1.3 without measurement noise. This plot shows eight obvious peaks that correspond with the eight times that the sensor passed over or approached a magnet in Figure 1.3. Also, the extreme minimums of Figure 1.4 can be seen to correspond to the points in time where the sensor passed well beyond m_2 in Figure 1.3.

In Figure 1.5, the same measurements are plotted, but this time with measurement noise added to the sensor. The measurement noise effects the sensor as described in Section 1.5.8.2. The

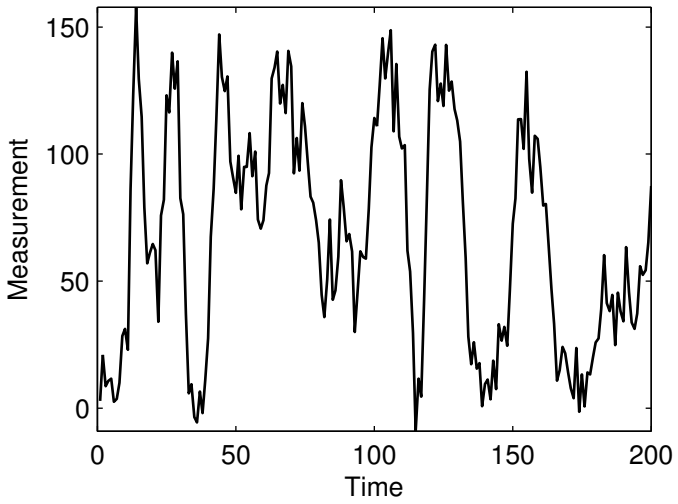

Figure 1.5: Plot of the measurements returned by the field strength sensor based on the sensor trajectory shown in Figure 1.3 with measurement noise.

noise added is Gaussian distributed with a mean of 0 and a standard deviation, σ_s, of 0.75. It can be seen from Figure 1.5 that the addition of noise affects the field strength peaks. The particle filter can be used to mitigate the effect of the measurement noise, balanced against the expected range of dynamic noise.

1.5.9 Particle Filter Results

The particle filter is used to filter the output of the simulated field strength sensor described in Section 1.5.8.2 with the goal of being able to track the location of the sensor based on the dynamic model and the field strength measurement provided by the sensor. $M = 1000$ particles are initialized with a state of $x_0^m = 0 \ \forall \ m$ and a weight of $w_0^m = \frac{1}{1000} \ \forall \ m$. Resampling using the select with replacement algorithm is performed when the ESS drops below $0.9 \cdot M = 900$. Figure 1.6 shows a plot of the true sensor position along with the filtered position output of the particle filter. It is important to note that this is the output of a single run. Additional runs would produce different outputs due to the random nature of the particle filter. The filtered position closely tracks the true position throughout much of the plot. However, in a number of locations the filtered position is a mirror image of the true position. This is due to the ambiguity in the system. It is difficult to determine based only on the dynamic model and measurements which magnet the sensor is located near due to the symmetry of the problem.

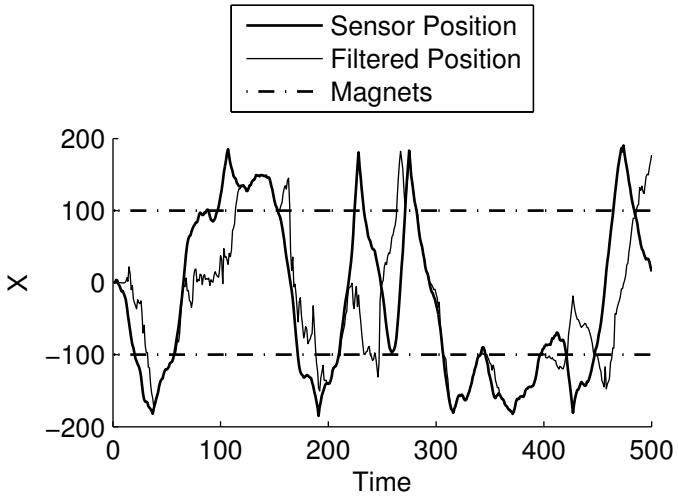

Figure 1.6: Plot of the true sensor location along with the filtered location estimate.

Chapter 2

Environment Noise

UWB indoor positioning works by measuring range and/or angle estimates from a set of fixed points to a moving terminal (MT) [49]. The set of measurements is then used to calculate position through multilateration or multiangulation [50]. Error sources for a single UWB range measurement include multipath, NLOS, clock drift and interference [51]. Range estimates can be improved by several techniques, for example, through averaging multiple measurements [38], improved peak detection [52], and signal pulsing [29]. Instead of solving for a unique range estimate, the RSS profile can be tracked over time to detect LOS to NLOS transitions [40, 53]. Statistics concerning the error sources, such as NLOS bias, can be included in the state matrix for each range estimate used in positioning [36, 54, 55]. A similar approach has been shown to help reduce the effect of multipath in GPS tracking [56]. Errors in timing synchronization can be refined simultaneously with position estimation [57]. Multipath interference, sampling rate limitations, tag synchronization and antenna phase-center variation are addressed in [21]; further work in [22] combined carrier-based and energy detection-based UWB signals.

Figure 2.1 show three diagrams that describe what the author means by the term measurement noise. In Figure 2.1a, the actual motion or ground truth information for a path traversed through this hypothetical facility is indicated by the thick line. Figure 2.1b shows the same hypothetical facility with a flow field plotted in each room. The flow field describes how a raw measurement is corrupted by noise sources in the measurement system and the actual environment. A raw measurement is a measurement that comes directly from the UWB positioning system without any type of filtering applied. Measurements in the room on the top left are pushed predominantly up and

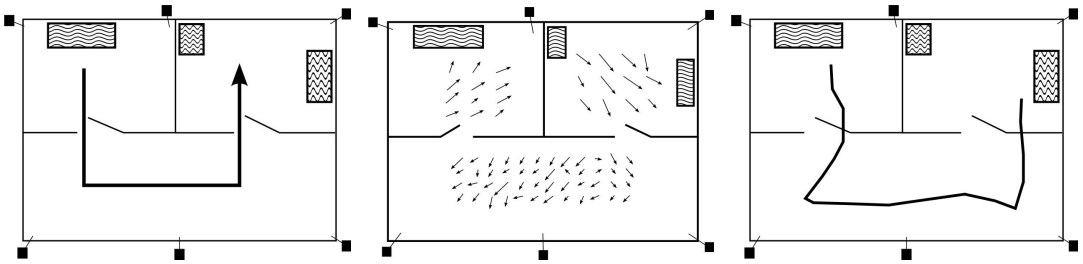

(a) Actual motion (b) Environment noise (c) Raw measurements

Figure 2.1: Graphical depiction of environment noise. Thicker lines represent the actual motion (left) and raw measurements (right).

to the right. Measurements in the bottom room are pushed predominantly down and to the right or left depending on the area of the room. Measurements in the room on the top right are pushed predominantly down and to the right. The particular flow field can be caused by NLOS conditions, multipath, sensor geometry and/or sensor orientation. Environment noise is different from the noise that corrupts individual range measurements although noise on range measurements contributes to environment noise. Environment noise aggregates all of the sources of error together *after* position estimation is performed from a set of range measurements. Up until now, it has been unknown what this type of noise looks like throughout a real world installation of a UWB positioning system. The noise could be single or multi-modal, Gaussian or Rayleigh. It may change frequently over time or it may be stable. It may vary wildly with small changes in position or be locally similar.

While all of the methods just discussed can improve UWB tracking accuracy, it is reasonable to assume that some amount of error will still occur, especially in challenging indoor environments where multipath and NLOS are the rule rather than the exception [58]. This work investigates the possibility of systematically observing the measurement noise and building a map of it throughout the area of interest. In order to understand the effect of environment noise on UWB indoor positioning and in turn filter out the effects of this noise, it is important to have an idea of what this measurement noise looks like in a real world scenario. In this work, an understanding of the measurement noise is gained by taking many measurements using a commercially-available UWB positioning system installed in a real world scenario and analyzing these measurements in various ways. To the author's knowledge, no one has used such an exhaustive approach to analyze measurement noise in UWB indoor positioning. Overall, it is desired to determine the degree and quality of measurement noise in a typical room-to-building sized environment; if the noise is stable over time; and if the noise is

locally similar.

2.1 Test Facilities

This work consists of measurements made throughout two different test facilities. The Shoothouse test facility, referred to as the Shoothouse facility, was closed part way through this work. The UWB tracking system portion of the facility was then relocated. The second location is referred to as the Riggs facility. The following sections describe each of these facilities.

2.1.1 Shoothouse Facility

The Shoothouse facility is an approximately 13 × 10 m indoor facility that was built as part of the Military Operations in Urban Terrain (MOUT) project at Clemson University [59, 60]. It consists of a painted concrete slab floor, a number of polyvinyl chloride (PVC) walls, and an exposed steel roof. Ten UWB receivers are distributed throughout the test area. A two-dimensional floor plan of the area is shown in Figure 2.2. Figures 2.3 and 2.4 are photos of the Shoothouse facility. The facility is configured into six different test rooms and two hallways as labeled on Figure 2.2. Table 2.1 gives the dimensions and area of each room, hallway and the full facility.

Table 2.1: Dimensions and areas of the Shoothouse facility.

Room	**X (m)**	**Y (m)**	**Area (m^2)**
1	3.67	3.58	13.14
2	3.73	3.58	13.35
3	3.68	3.58	13.17
4	3.24	3.62	11.73
5	3.32	3.54	11.75
6	3.28	3.54	11.61
Hallway 1	7.27	1.17	8.51
Hallway 2	1.17	9.72	11.37
All	12.49	9.72	121.90

2.1.2 Riggs Facility

The second test facility, used for a majority of this work, encompasses part of a hallway and an open lab space. The installation was designed so that the measurement noise would be similar to

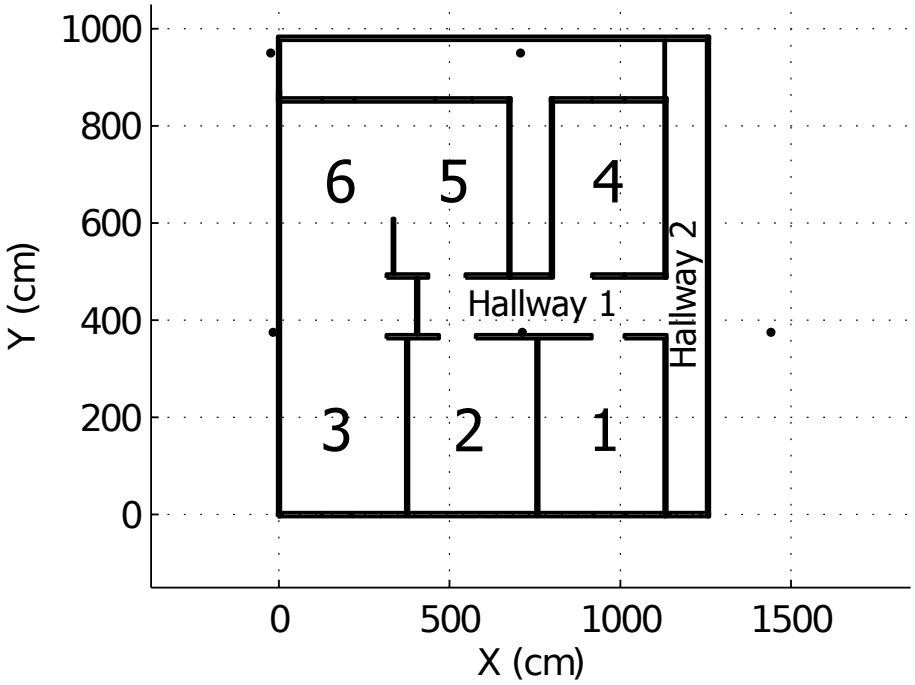

Figure 2.2: Floorplan of the Shoothouse test facility. Solid lines indicate walls. Circles indicate metal poles.

Figure 2.3: Overhead photo of Shoothouse facility.

Figure 2.4: Photo of the Shoothouse facility's main hallway.

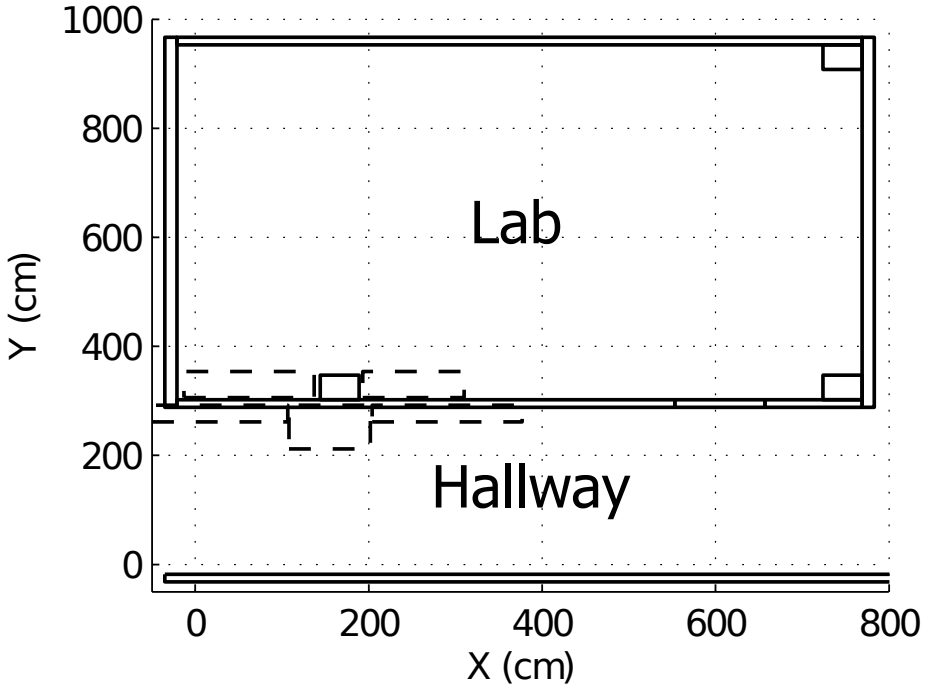

Figure 2.5: Floor plan of the Riggs facility. Walls are indicated by the solid lines and large objects by the dashed lines.

that of a standard office environment. It is an approximately 8 × 10 m area of Clemson University's Riggs Hall. This facility will be referred to as the Riggs facility. Eight UWB receivers are distributed throughout the test area. A two-dimensional floor plan of the area is shown in Figure 2.5. It can be seen from this figure that a block wall runs through the area dividing the lab (upper section) from the hallway (lower section). Also, there are a number of obstructions indicated by dashed lines. These obstructions include: wooden and metal cabinets, metal mailboxes and a vending machine. Figure 2.6 is a photo of the Riggs facility. The floor in the lab is carpet over concrete and the floor in the hallway is linoleum tile over concrete. The sensors are all installed above a dropped ceiling with standard mineral fiber tiles. Therefore, this installation is entirely non-line-of-sight (NLOS) but the dropped ceiling will affect each sensor equally. Table 2.2 gives the dimensions and area of each room, hallway and the full facility.

Figure 2.6: Photo of the Riggs facility.

Table 2.2: Dimensions and areas of the Riggs facility.

Room	**X (m)**	**Y (m)**	**Area (m^2)**
Lab	7.90	6.51	51.43
Hallway	8.18	3.06	25.03
All	8.04	9.71	78.07

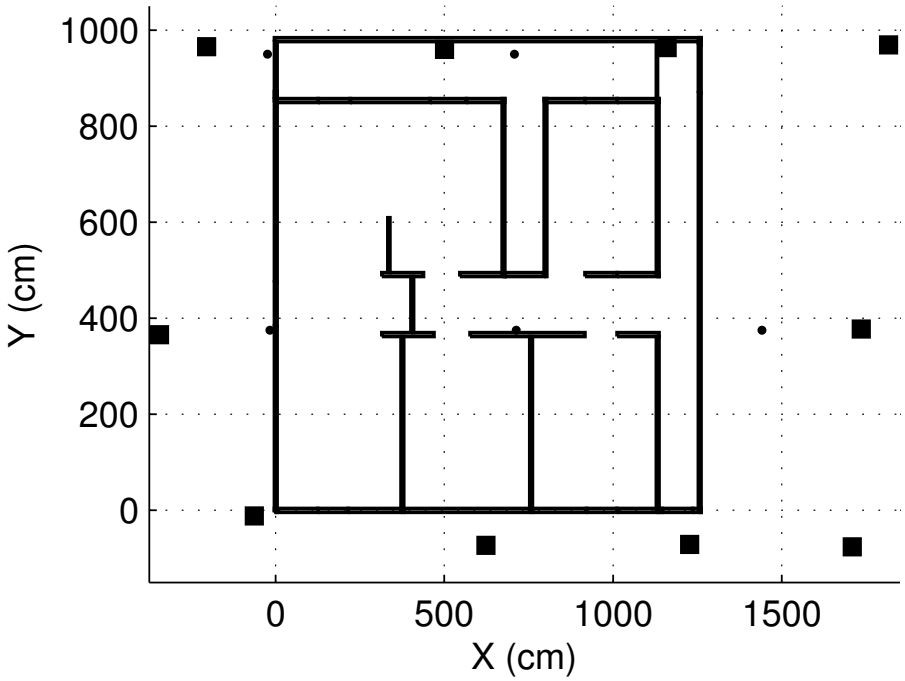

Figure 2.7: Floorplan of the Shoothouse test facility. Filled squares indicate sensor locations. Solid lines indicate walls. Circles indicate metal poles.

2.2 Ubisense System

Ubisense, Inc. is a U.K.-based company that produces UWB positioning systems marketed towards indoor asset and people tracking applications. They have 400 customers worldwide, many of which are researchers, as of 2010 [61]. Their UWB real-time location system is used to generate data for this work, although our methods could be applied to any geolocation system. Mobile Ubisense tags transmit UWB pulses which are detected by the fixed sensors. Range estimates to the tags are determined using angle of arrival (AOA) and time-difference of arrival (TDOA) techniques which allows the system to calculate position estimates with as few as two sensors reporting measurements [62, 63].

The sensor locations are fixed at known locations. These locations are based on relative coordinate systems defined within the test facilities. Figures 2.7 and 2.8 show floorplans of the two test facilities along with squares indicating Ubisense sensor locations. The relative location of each sensor was determined using tape measures, laser squares and laser distance measurement tools. These ground truth sensor locations are used by the Ubisense system to calculate tag location.

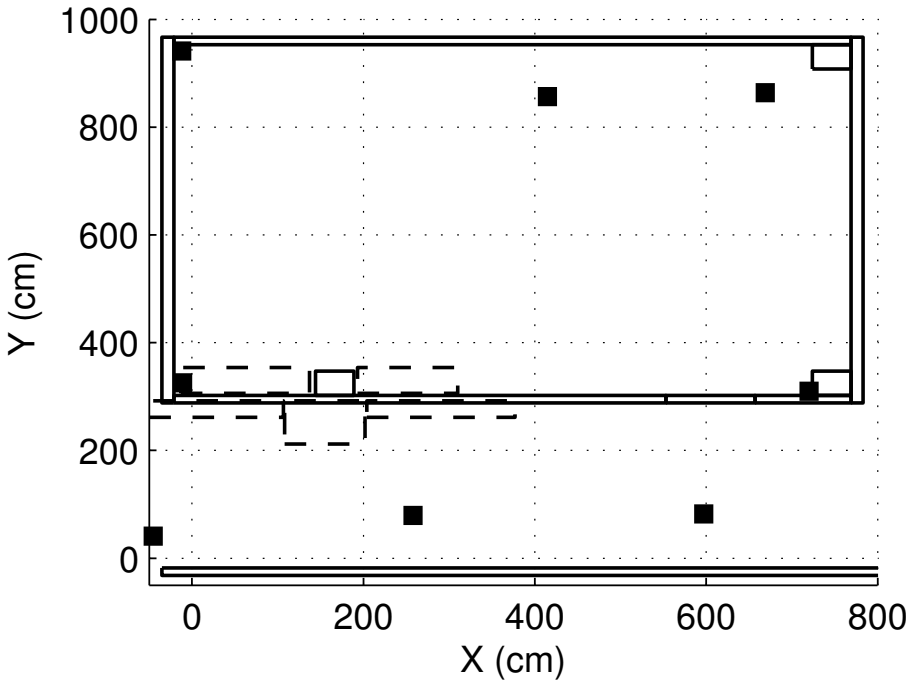

Figure 2.8: Floor plan of the Riggs facility. The sensor locations are indicated by the filled squares. Walls are indicated by the solid lines and large objects by the dashed lines.

Ubisense Series 7000 IP sensors were installed in each facility using C-clamps and cable ties. Figure 2.9 shows the installation of a sensor in the Shoothouse facility. Figure 2.10 shows the installation of a sensor in the Riggs facility. It is worth noting again that the sensors are installed above a dropped ceiling that contains wiring and other building infrastructure components. Ubisense UWB transmitter tags are the mobile portion of the system. Figure 2.11 is a photo of a Ubisense Series 7000 compact tag. This tag model was used throughout this work.

An example of a four-sensor Ubisense system installation is shown in Figure 2.12. The Ubisense UWB transmitter tag is shown as the circle labeled "Tx". The sensors are the squares labeled as "Rx". Measurement and configuration information is communicated via the Ethernet network which consists of a gigabit switch (labeled as "Switch") and category 5 cabling. Sensors maintain accurate timing information through the use of the separate timing network. The timing network maintains high accuracy through the use of category 6 cabling and the timing calibration process which determines propagation delay between sensors. The Ubisense Location Engine software is executed and data is stored for offline analysis on the personal computer (labeled as "PC").

Figure 2.9: Photo of a sensor installed in the Shoothouse facility.

Figure 2.10: Photo of a sensor installed in the Riggs facility.

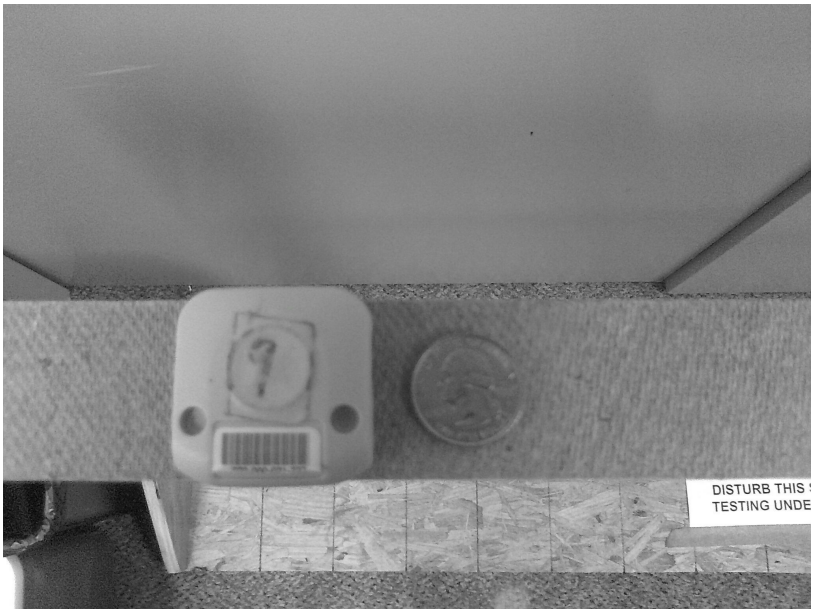

Figure 2.11: Photo of a Ubisense UWB transmitter tag.

Further information regarding the Ubisense system and its installation and calibration process can be found in [17, 63].

2.3 Measurement Collection

To gain knowledge of the overall measurement noise affecting these installations, measurements were taken at ground truth locations in a dense grid throughout each test facility. The ground truth positions were determined relative to the coordinate system and in the same manner as discussed for the sensors in Section 2.2. A stand, shown in Figure 2.13, was built to accurately place the tags at known locations. It was placed on the coordinate system defined on the floors of the test facilities to ensure accurate ground truth. Based on the methods used to determine these ground truth locations, the coordinate systems are believed to be accurate to within 1 cm. Figures 2.14 and 2.15 show the ground truth locations where measurements were taken with unfilled squares. In the Shoothouse facility, measurements were taken at 7,931 locations. In the basement facility, measurements were taken at 3,272 locations. A space of 10 cm separates each collection location and 500 measurements were collected at each location. This results in over 5.6 million total measurements being taken. A number of gaps can be seen in the measurement locations shown in Figure 2.15.

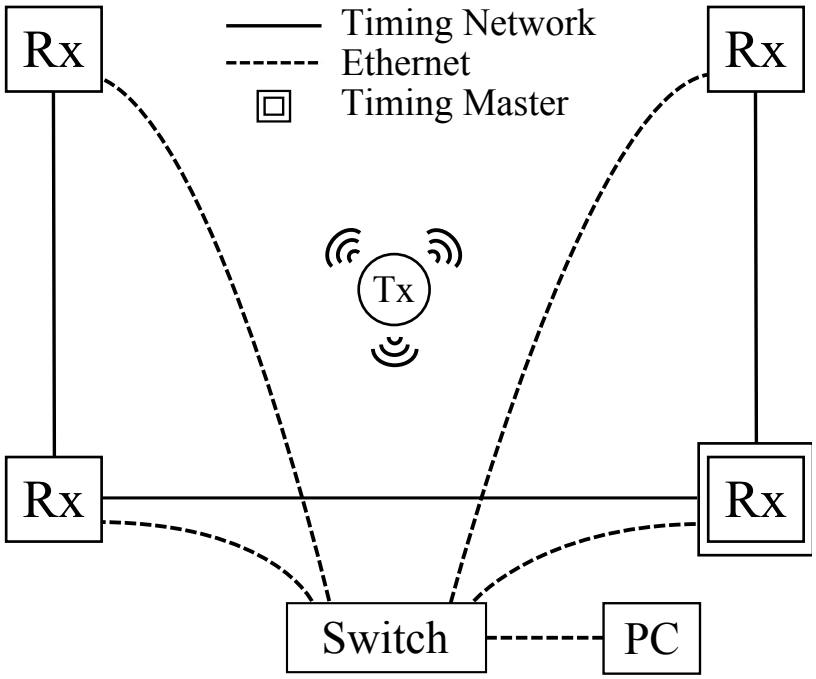

Figure 2.12: Example four-sensor installation of the Ubisense system.

These are locations where the tracking system does not regularly report measurements due to the installation.

2.4 Observed Measurement Noise

Figure 2.16 shows an example set of 500 measurements collected at (480, 540) cm within the Riggs facility. It is worth noting that this measurement data forms a distinct cluster and is largely shifted down and to the left from the ground truth location indicated by the large cross symbol. Figure 2.17 shows another set of 500 measurements collected at (620, 430) cm within the test facility. This measurement data is different from that of Figure 2.16 because it clearly forms multiple clusters. Figures 2.16 and 2.17 are representative of the types of noise seen throughout the test facilities.

In our 5 million observations, the majority of locations showed measurement noise similar in quality to that shown in Figures 2.16 and 2.17, with a number of distinct clusters varying from 1 to as many as 6.

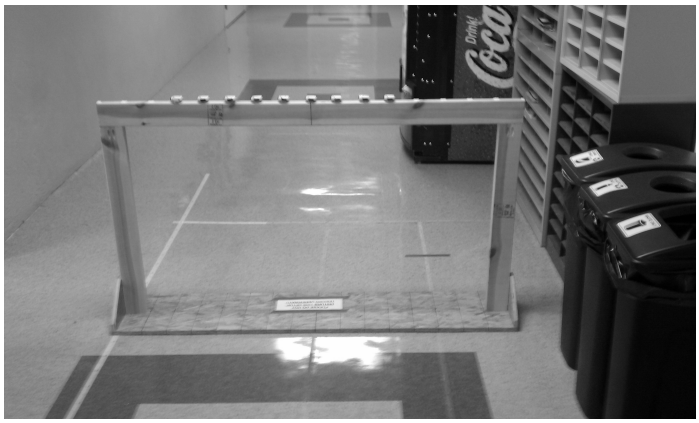

Figure 2.13: Stand with tags positioned in the corridor during collection of model data.

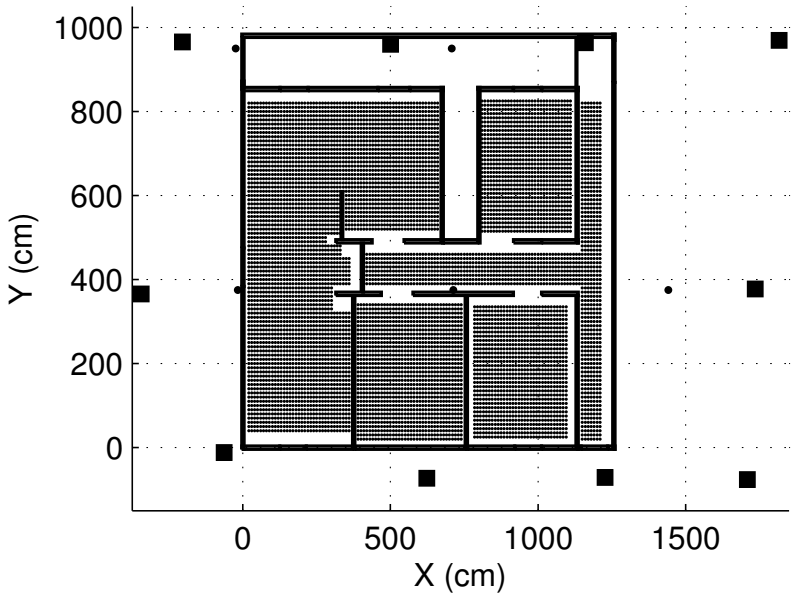

Figure 2.14: Floor plan of the Shoothouse test facility. Filled squares indicate sensor locations. Unfilled squares indicate locations surveyed. Solid lines indicate walls.

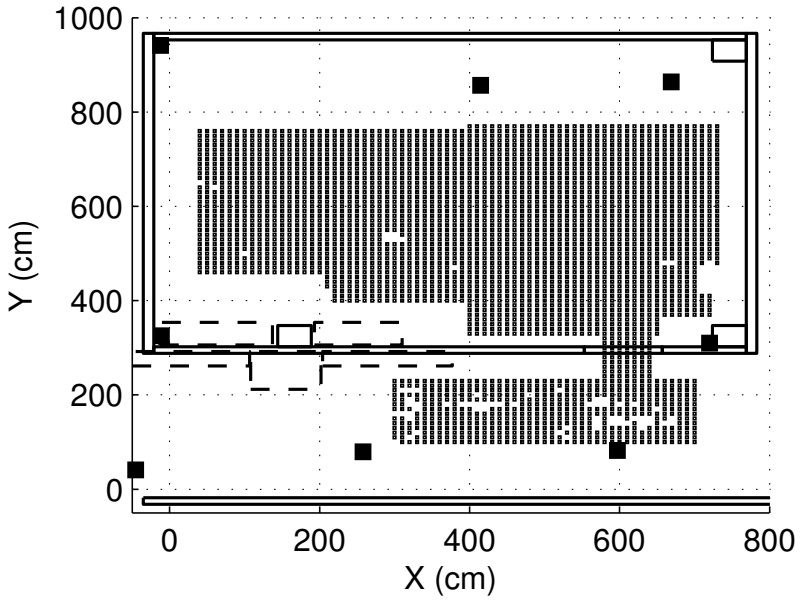

Figure 2.15: Floor plan of the test area. The sensor locations are indicated by the filled squares. The locations surveyed to generate the measurement noise model are the smaller, unfilled squares. Walls are indicated by the solid lines and large objects by the dashed lines.

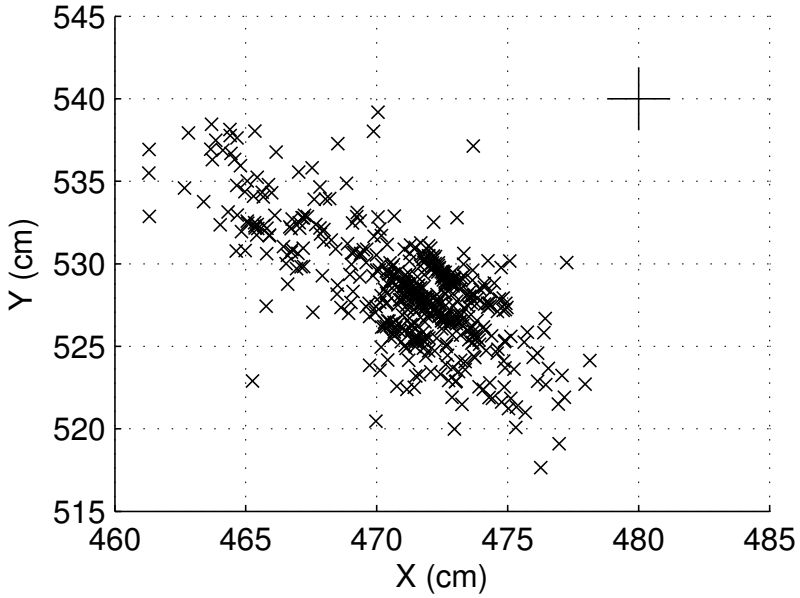

Figure 2.16: Measurements taken at location (480, 540) cm.

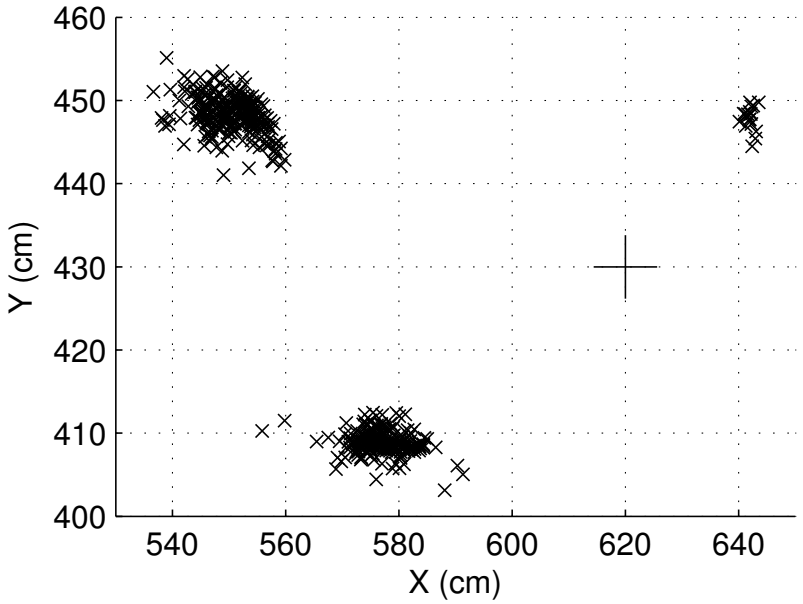

Figure 2.17: Measurements taken at location (620, 430) cm.

2.5 Measurement Model

The measurement model assumes that all measurements generated by the UWB positioning system are corrupted by some type of measurement noise. It is assumed that this measurement noise is sampled from a 2×1 random vector $\boldsymbol{\nu}$, given by Equation 2.1.

$$\boldsymbol{\nu} = \begin{bmatrix} \nu_x \\ \nu_y \end{bmatrix} \tag{2.1}$$

This assumption leads to the set of measurement equations shown in Equation 2.2 where x_t and y_t are the location components of the current state $\mathbf{x}_t$, described in Section 3.2.

$$\mathbf{z}_t = \mathbf{g}(\mathbf{x}_t, \boldsymbol{\nu}_t) = \begin{bmatrix} z_{x,t} = x_t + \nu_{x,t} \\ z_{y,t} = y_t + \nu_{y,t} \end{bmatrix} \tag{2.2}$$

2.6 Measurement Noise Model

Based on 5.6 million observations, it was determined that a multi-modal Gaussian distribution could sufficiently model the observed measurement noise. Therefore, a weighted mixture

of Gaussians is adopted for the measurement noise model similar to that described in [64]. The measurement noise $\boldsymbol{\nu}$ is assumed to be a bivariate, multi-modal Gaussian random variable (RV). The probability density function (PDF) of this type of RV is made up of weighted PDFs of multiple uni-modal, bivariate Gaussian RVs and described by Equation 2.3. This PDF is often referred to as a mixture of Gaussians and has been previously used to model measurement noise for frequency demodulation as well as joint channel estimation and symbol detection [65]. This equation has five parameters for each mode: the means, $\mu_{x,i}$ and $\mu_{y,i}$, the standard deviations, $\sigma_{x,i}$ and $\sigma_{y,i}$, and the correlation coefficient, $\rho_{x,y,i}$.

$$\begin{aligned} p_i(z_x, z_y|x, y) &= \frac{1}{2\pi\sigma_{x,i}\sigma_{y,i}\sqrt{1-\rho_{x,y,i}^2}} \exp\left(\frac{-1}{2(1-\rho_{x,y,i}^2)}\right. \\ &\quad \left[\frac{(z_x-\mu_{x,i})^2}{\sigma_{x,i}^2} + \frac{(z_y-\mu_{y,i})^2}{\sigma_{y,i}^2}\right. \\ &\quad \left.\left. -\frac{2\rho_{x,y,i}(z_x-\mu_{x,i})(z_y-\mu_{y,i})}{\sigma_{x,i}\sigma_{y,i}}\right]\right) \end{aligned} \tag{2.3}$$

By defining a 2×1 measurement vector $\mathbf{z}$ as shown in Equation 2.4, Equation 2.3 can be written in matrix notation as shown in Equation 2.5 where $\boldsymbol{\mu}_{\mathbf{x},i}$ is the 2×1 mean vector and $\Sigma_{\mathbf{x},i}$ is the 2×2 covariance matrix shown in Equation 2.6. Note that the symbol $|\cdot|$ represents the matrix determinant.

$$\mathbf{z} = \begin{bmatrix} z_x \\ z_y \end{bmatrix} \tag{2.4}$$

$$p_i(\mathbf{z}|\mathbf{x}) = \frac{1}{2\pi\sqrt{|\Sigma_{\mathbf{x},i}|}} e^{-\frac{1}{2}(\mathbf{z}-\boldsymbol{\mu}_{\mathbf{x},i})^T \Sigma_{\mathbf{x},i}^{-1}(\mathbf{z}-\boldsymbol{\mu}_{\mathbf{x},i})} \tag{2.5}$$

$$\Sigma_{\mathbf{x},i} = \begin{bmatrix} \sigma_{x,i}^2 & \rho_{\mathbf{x},i}\sigma_{x,i}\sigma_{y,i} \\ \rho_{\mathbf{x},i}\sigma_{x,i}\sigma_{y,i} & \sigma_{y,i}^2 \end{bmatrix} \tag{2.6}$$

Using Equation 2.3, the PDF of $\boldsymbol{\nu}$ can be defined as shown in Equation 2.7 where $I_{x,y}$ is the number of modes and $\omega_{x,y,i}$ is the weight value associated with the ith mode. The $\omega_{x,y,i}$ values must sum to one for $p_{\boldsymbol{\nu}}(z_x, z_y|x, y)$ to be a valid PDF. Figure 2.18 shows an example of a two-dimensional,

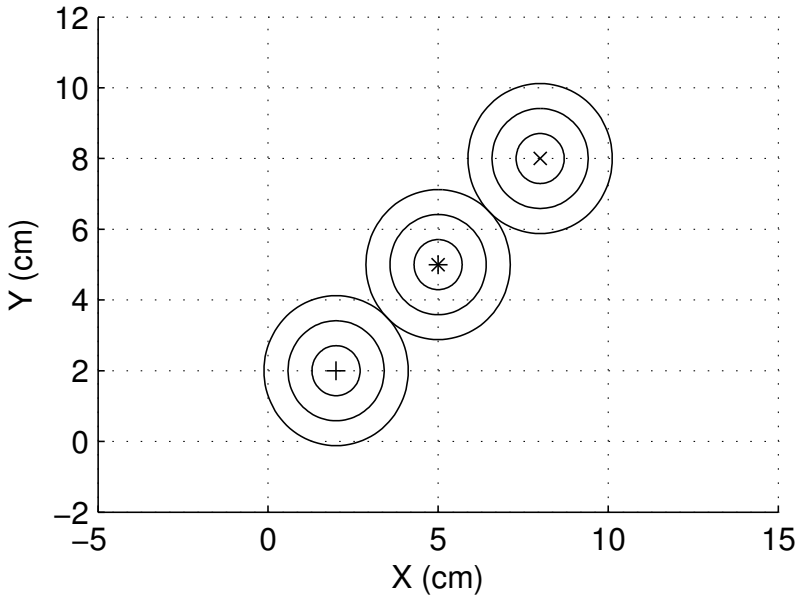

Figure 2.18: Contour plot of a two-dimensional, tri-modal Gaussian PDF with $\mu_{x,i} = \mu_{y,i} = \{2, 5, 8\}$, $\sigma_{x,i} = \sigma_{y,i} = 0.5$ and $\rho_{x,y,i} = 0$ for $i = 1, 2, 3$.

tri-modal Gaussian PDF with means $\mu_{x,i} = \mu_{y,i} = \{2, 5, 8\}$, $\sigma_{x,i} = \sigma_{y,i} = 0.5$ and $\rho_{x,y,i} = 0$ for $i = 1, 2, 3$. The contour lines are at one, two and three standard deviations from the mean.

$$p_{\boldsymbol{\nu}}(z_x, z_y|x, y) = \sum_{i=1}^{I_{x,y}} \omega_{x,y,i} \cdot p_i(z_x, z_y|x, y) \tag{2.7}$$

Equation 2.7 can be written in matrix notation as shown in Equation 2.8 where $\omega_{\mathbf{x},i}$ is the weight and $I_{\mathbf{x}}$ is the number of modes.

$$p_{\boldsymbol{\nu}}(\mathbf{z}|\mathbf{x}) = \sum_{i=1}^{I_{\mathbf{x}}} \omega_{\mathbf{x},i} \cdot p_i(\mathbf{z}|\mathbf{x}) \tag{2.8}$$

2.7 Generating The Measurement Noise Map

It is assumed that there exists a PDF, $p_{\boldsymbol{\nu}}(\mathbf{z}|\mathbf{x})$, described by Equation 2.8, for each possible location within the trackable area of the test facility. Since it would be impossible to collect the infinite number of measurements that this model requires, measurements have been collected at discrete locations as described in Section 2.3. Local similarity of the measurement noise is assumed between discrete locations. The model parameters that are calculated for each location make up the

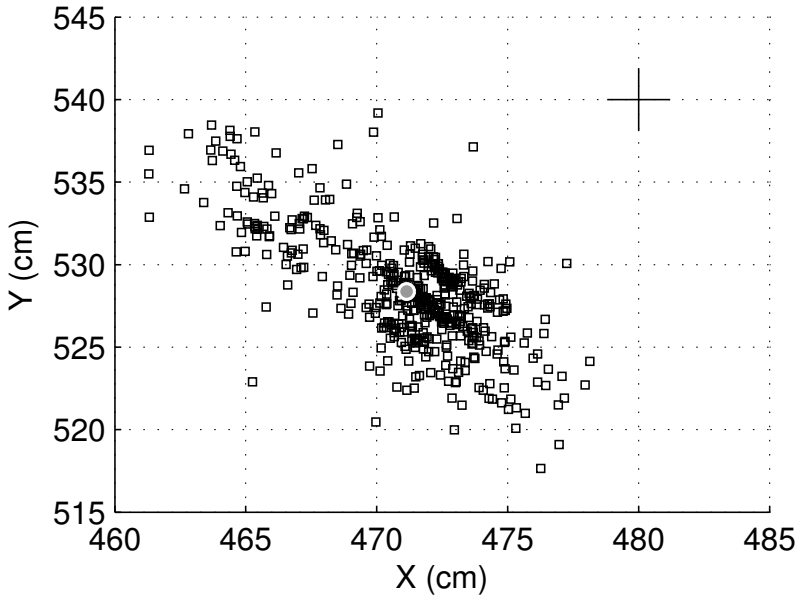

Figure 2.19: Measurements from (480, 540) cm clustered using DBSCAN with $\epsilon = 30$ and $k = 10$. Cluster mean indicated by the gray circle.

measurement noise map.

Equation 2.8 requires that four parameters be calculated from the collected measurements: $I_{\mathbf{x}}$, $\boldsymbol{\mu}_{\mathbf{x},i}$, $\Sigma_{\mathbf{x},i}$ and $\omega_{\mathbf{x},i}$. The first, $I_{\mathbf{x}}$, is the number of clusters present in the data at the location given by $\mathbf{x}$. It is determined using the density-based spatial clustering for applications with noise (DBSCAN) algorithm developed by Ester, et al. in [66]. This algorithm was selected because it does not require the number of clusters to be specified a priori as is the case for other common data clustering algorithms, such as K-means. DBSCAN requires two parameters: ϵ, the neighborhood size and k, the minimum number of points necessary to be considered a cluster. Clustered versions of the example set of measurements shown in Figures 2.16 and 2.17 are shown in Figures 2.19 and 2.20 respectively. It can be seen that a single cluster, whose mean is indicated by the gray circle is found in Figure 2.19. However, three cluster means are shown in Figure 2.20.

The cluster mean vector, $\boldsymbol{\mu}_{\mathbf{x},i}$ is calculated for each cluster $i = 1, 2, \ldots, I_{\mathbf{x}}$ found by DBSCAN using Equation 2.9 where x and y are the location components of the state space variable $\mathbf{x}$, $\mathbf{z}_i^n$ is the nth 2×1 measurement vector assigned to cluster i from the measurements taken at location (x, y) cm. $N_{\mathbf{x},i}$ denotes the number of measurements collected at location (x, y) cm that are assigned

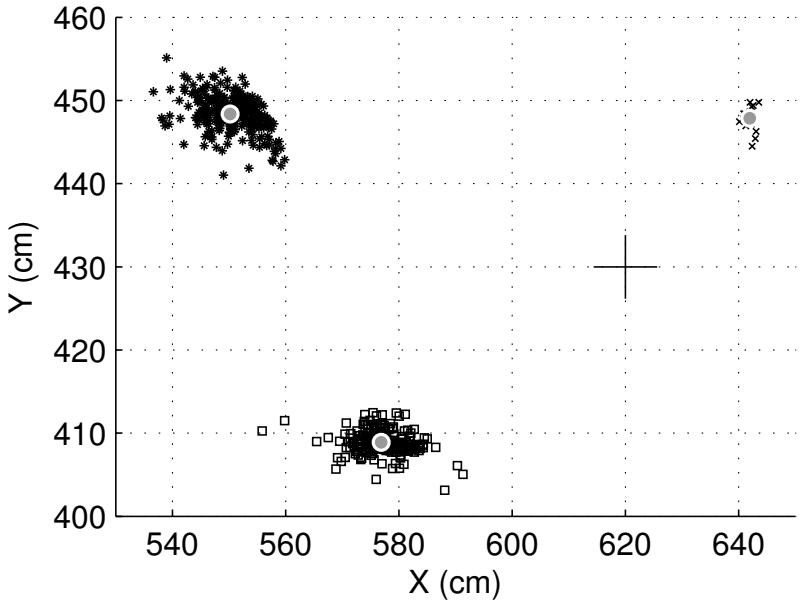

Figure 2.20: Measurements from (620, 430) cm clustered using DBSCAN with $\epsilon = 30$ and $k = 10$. Cluster means indicated by the gray circles.

to cluster i.

$$\boldsymbol{\mu}_{\mathbf{x},i} = \begin{bmatrix} \mu_{x,i} \\ \mu_{y,i} \end{bmatrix} = \frac{1}{N_{\mathbf{x},i}} \left(\sum_{n=1}^{N_{\mathbf{x},i}} \mathbf{z}_i^n \right) - \begin{bmatrix} x \\ y \end{bmatrix} \tag{2.9}$$

$\Sigma_{\mathbf{x},i}$ is the 2×2 unbiased covariance matrix for cluster i at the location given by $\mathbf{x}$ and is calculated as shown in Equation 2.10.

$$\Sigma_{\mathbf{x},i} = \frac{1}{N_{\mathbf{x},i} - 1} \sum_{n=1}^{N_{\mathbf{x},i}} (\mathbf{z}_i^n - \boldsymbol{\mu}_{\mathbf{x},i})(\mathbf{z}_i^n - \boldsymbol{\mu}_{\mathbf{x},i})^T \tag{2.10}$$

The final parameter, $\omega_{\mathbf{x},i}$, is a weight value associated with cluster i at the location given by $\mathbf{x}$. It is calculated by dividing the number of measurements assigned to the cluster by the total number of measurements taken at that location, N, which is 500 throughout this work. Equation 2.11 shows this calculation.

$$\omega_{\mathbf{x},i} = \frac{N_{\mathbf{x},i}}{N} \tag{2.11}$$

These four parameters are used in conjunction with Equation 2.8 to determine the prob-

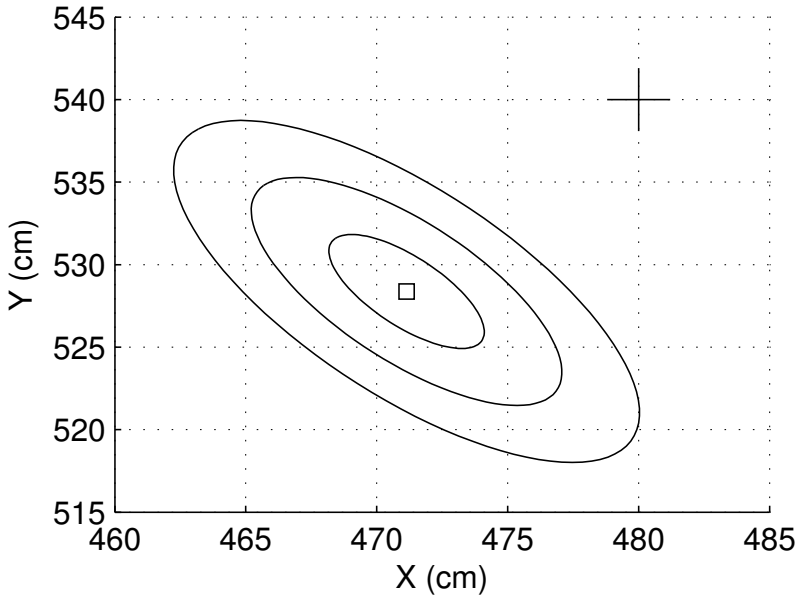

Figure 2.21: Model generated from example measurements collected at (480, 540) cm. The ellipses show one, two and three standard deviations from the mean for each cluster.

ability that a measurement was generated by a tag at a specific location. Contour plots of the measurement noise model generated for the example set of measurements shown previously in Figures 2.19 and 2.20 are shown in Figures 2.21 and 2.22 respectively. The contour lines are at one, two and three standard deviations from the mean.

2.8 Measurement Noise Map

Figures 2.23 and 2.24 show maps of the number of clusters determined by the DBSCAN algorithm at all measurement locations within each test facility. It can be seen from these figures that the measurement noise typically contains only one cluster but that multiple clusters occur near walls and the boundaries of the trackable area. More specifically, 83% of the locations surveyed in the Shoothouse facility and 68% of the locations surveyed in the basement facility have a single cluster. It is believed that the difference in the percentage of uni-modal locations is due to the large number of locations within the Riggs facility that exhibit high measurement noise. These locations are primarily located within the hallway. The poor measurement quality is likely caused by the NLOS conditions created by the block wall that separates locations in the hallway from the

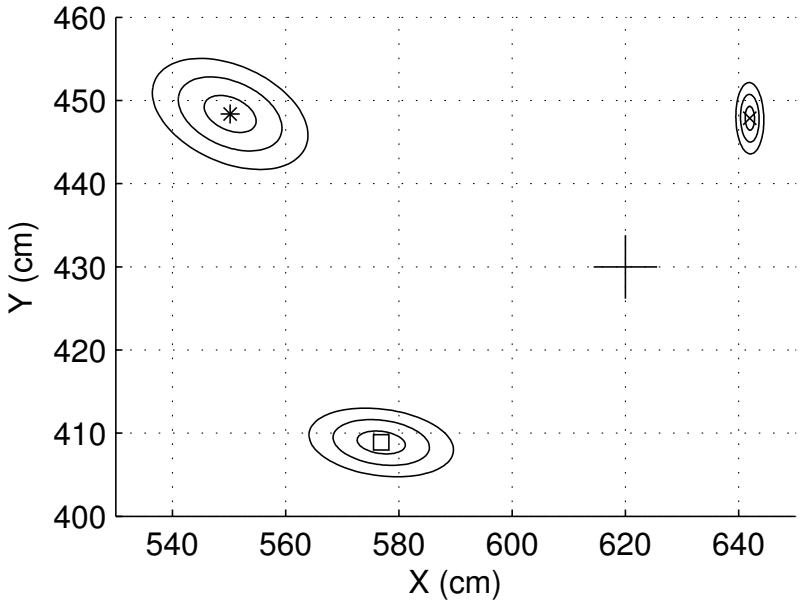

Figure 2.22: Model generated from example measurements collected at (620, 430) cm. The ellipses show one, two and three standard deviations from the mean for each cluster.

bulk of the sensors. This type of measurement noise behavior is taken into account by the use of a multi-modal Gaussian model.

Figures 2.25 and 2.26 show the average error vector for every fourth collection location in each facility. It can be seen that measurements taken at different areas within each facility are biased away from the ground truth location in different directions and with different magnitudes. The proposed map–based measurement noise model accounts for this location-dependent bias.

2.9 Stability Over Time

The validity of the measurement noise model developed in this work depends on the assumption that the measurement noise remains relatively constant over time. If the noise changes significantly from hour to hour or day to day, the model calculated from measurements collected at a specific time will no longer be valid at a later date. To test for stability over time, measurements were taken in a subset of the trackable area of the basement facility over two months to compare the measurement noise models over time. Measurements were collected in 10 cm intervals as described in Section 2.3 in the range of (310 - 470, 540 - 630) cm on three consecutive days and then again

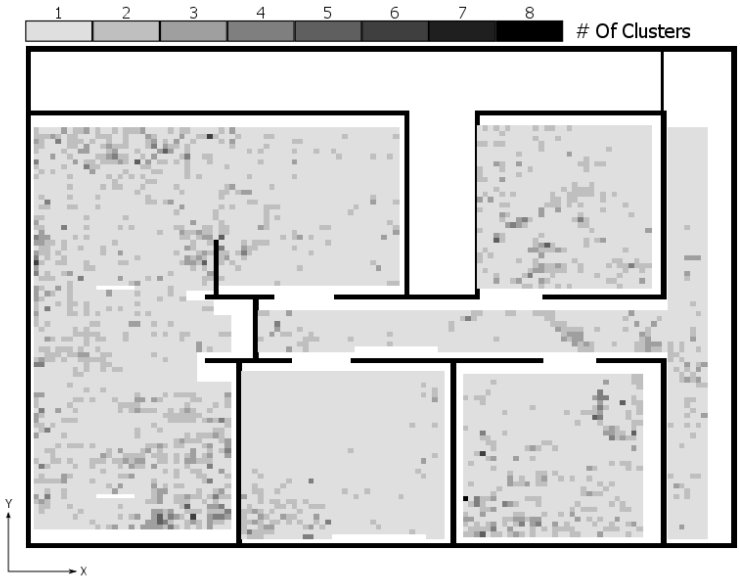

Figure 2.23: Contour plot of the number of clusters determined by the DBSCAN algorithm at each measurement location within the Shoothouse facility, $\epsilon = 30$ cm and $k = 10$. The large gray area indicates one cluster.

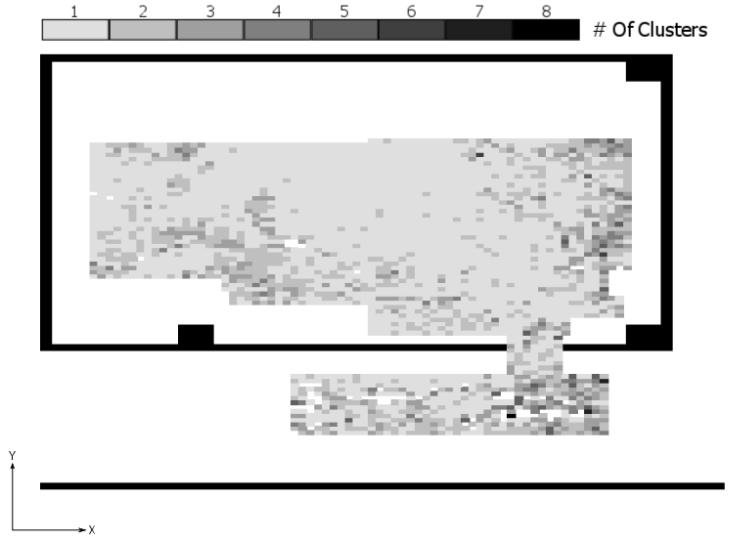

Figure 2.24: Contour plot of the number of clusters determined by the DBSCAN algorithm at each measurement location within the test facility, $\epsilon = 30$ cm and $k = 10$. The large gray area indicates one cluster.

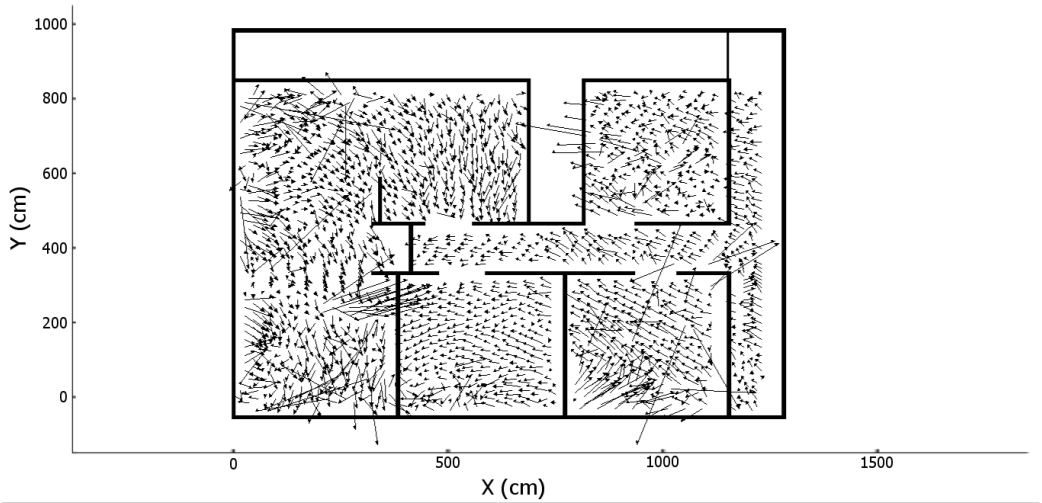

Figure 2.25: Plot of error vectors in the Shoothouse facility.

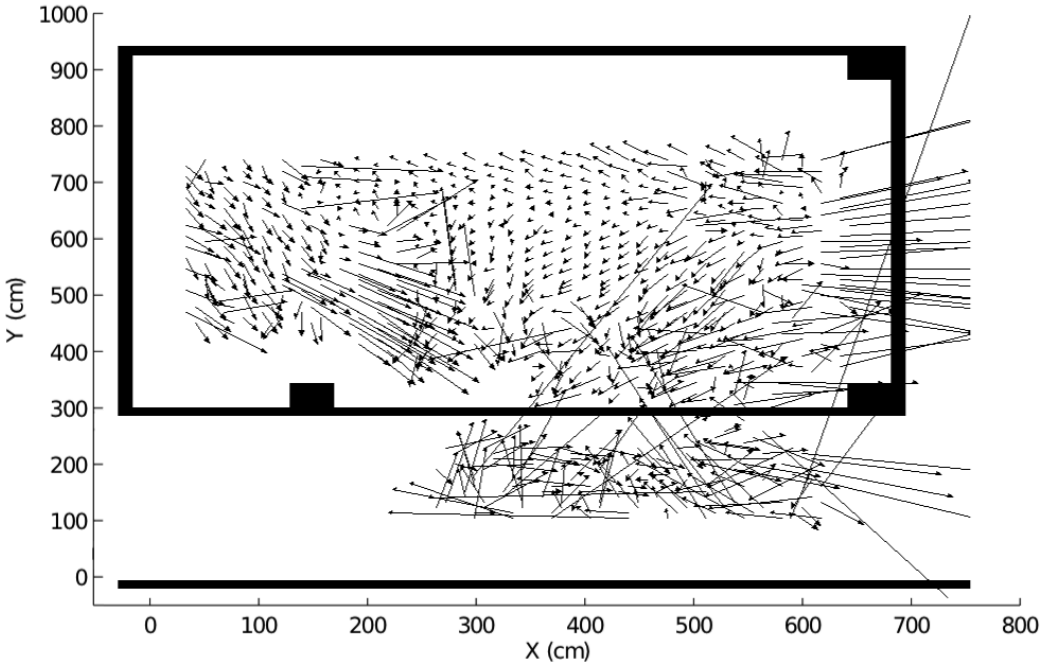

Figure 2.26: Plot of error vectors in the Riggs facility.

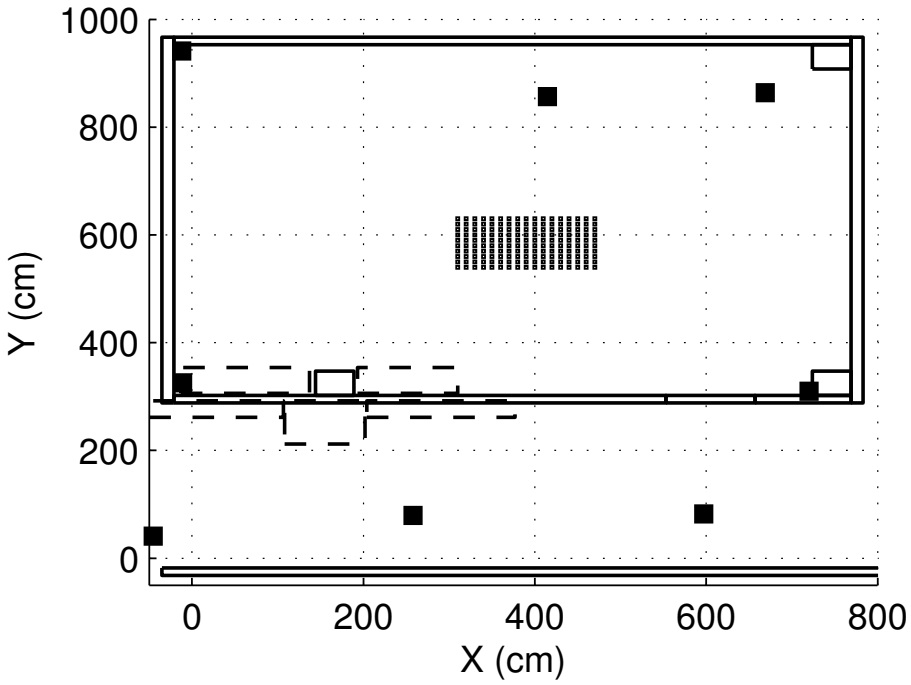

Figure 2.27: Plot of subset of locations collected over two months to test for stability over time.

two months later. Figure 2.27 is a plot of the locations that were surveyed.

Figure 2.28 is a plot of the model generated for measurements collected at (470, 590) cm on these four days. It can be seen from this figure that all cluster means (+, *, x and diamond symbols) are south and west of the ground truth location, denoted by the large cross symbol in the upper right. The ellipses shown are each three standard deviations from the respective mean according to the sample covariance matrices and can be seen to significantly overlap one another. Figure 2.28 is representative of the type of change in model that is seen across the area surveyed. One way of quantifying the change in cluster mean over time is to consider the average. The average change in cluster mean over time is 3.7 cm with a standard deviation of 3.1 cm. This is small compared to the average error, which is approximately 20 cm.

2.10 Local Similarity

Local similarity refers to the differences in measurement noise from one position to another within a small area. It is assumed that the measurement noise does not change significantly from

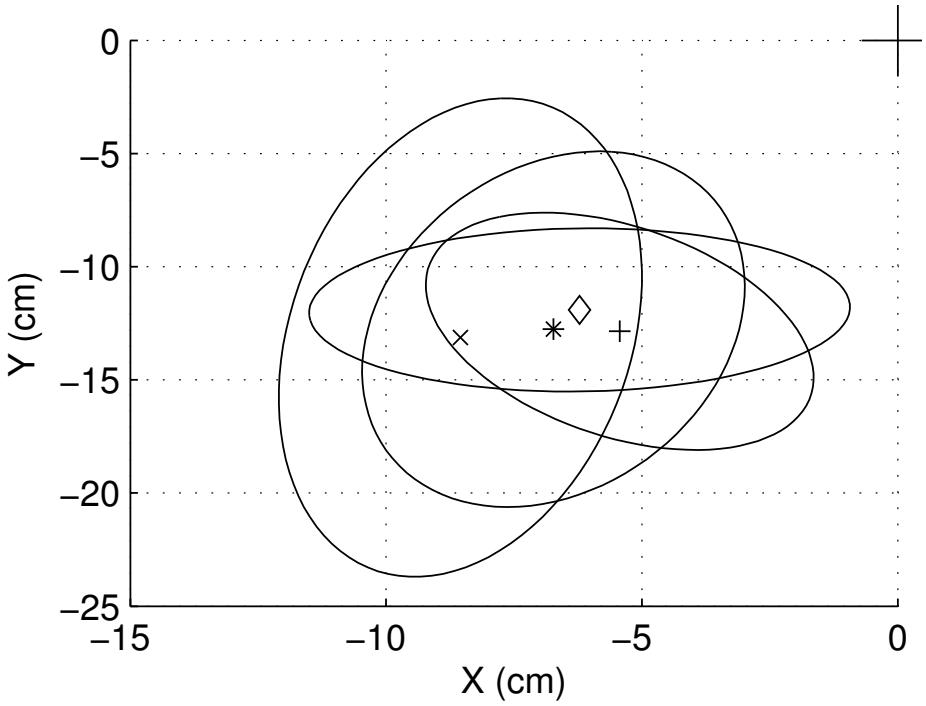

Figure 2.28: Zoomed in plot of model data collected on three consecutive days and then again two months later. The cluster means are indicated by the +, *, x and diamond symbols.

one measurement location to the next, i.e. within 10 cm. Therefore, the model for the measurement location closest to the state is used as the model for that state because it is not possible to have model data for all states. To test this assumption, measurements were taken at 1 cm intervals in a subset of the trackable area and now compare them to determine the validity of the local similarity assumption. Figure 2.29 is a plot of four sets of model data. The model indicated by the small cross symbol is the one measured at the given location. The model indicated by the asterisk is the model from the nearest measurement location on the measurement noise map. It can be seen that the means from all four locations are close to each other and that there is significant overlap of the ellipses. While this is a limited test, it does provide some confidence in the assumption of local similarity.

2.11 Environment Noise Conclusions

Based on the results of the previous sections, it can be concluded that the environment noise present in a UWB local positioning system shows evidence of stability over time and local similarity.

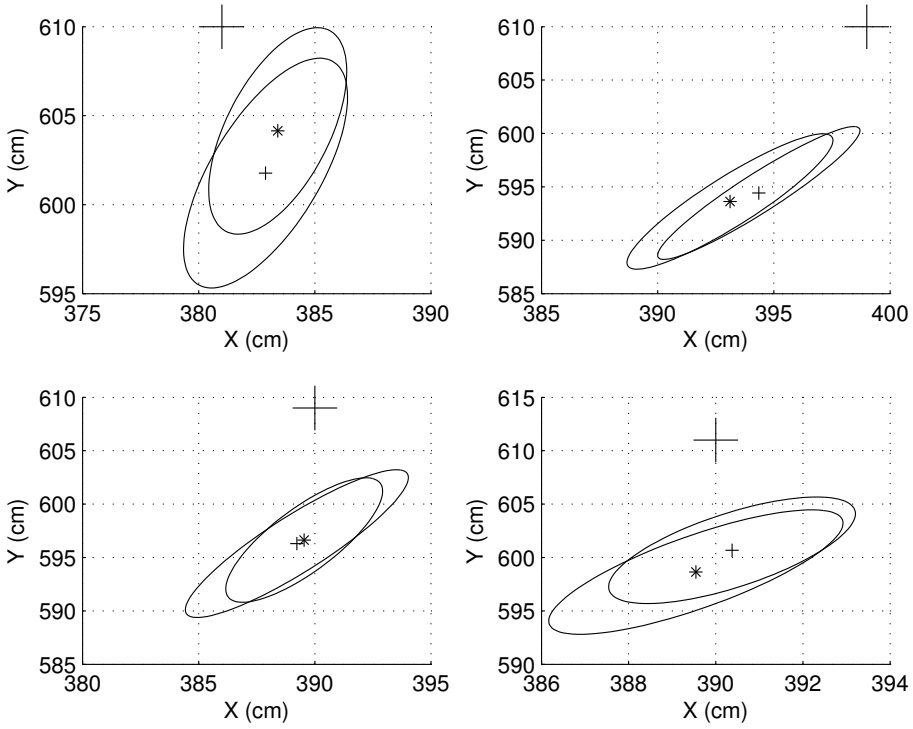

Figure 2.29: Zoomed in plot of the measured model (small cross) and adjusted model (asterisk) at (381, 610), (399, 610), (390, 609), (390, 611) cm in the top left, top right, bottom left and bottom right respectively.

Furthermore, the noise is shown to be single or multi-modal with a single mode being present in approximately 70% of the locations surveyed within two facilities. It has also been shown that the environment noise can be modeled using a weighted sum of two-dimensional Gaussian random variables. The presence of multi-modal environment noise is an unexpected result. Because the noise has been found to be non-Gaussian, the Kalman filter and extended Kalman filters are no longer optimal because they work on the assumption that measurement and process noise are both Gaussian. Therefore, the particle filter is an ideally-suited method for filtering measurements from this type of system.

Chapter 3

Augmented Particle Filter

The previous chapter describes two measurement campaigns undertaken to analyze environment noise throughout a test facility. As part of this analysis, a map of facility-wide measurement noise was created. In this chapter, a particle filter augmented with this measurement noise map is proposed to improve position tracking accuracy. The particle filter is a technique for implementing recursive Bayesian estimation through Monte Carlo approximation [67, 68]. It has become a popular alternative to the Kalman and extended Kalman filters for applications with non-Gaussian noise [46] and is ideally suited to filter the multi-modal measurement noise observed during the analysis described in the previous chapter.

3.1 Related Work

Improved tracking accuracy through map augmentation has been studied in a number of previous works. In [69], two map augmented particle filters are proposed. The first uses street maps to improve vehicle positioning accuracy with wheel speed sensor measurements. The second uses digital terrain elevation maps to improve aircraft positioning accuracy with an inertial navigation system. Similarly, Karlsson and Gustafsson augmented a particle filter with a map of distance measurements to determine the location of surface and underwater marine vessels [70]. This method is proposed as an alternative to GPS navigation. In [71], Davidson, et al. augmented a particle filter with building floor plan data to improve the accuracy of indoor pedestrian navigation using gyroscopes and accelerometers.

Maps of measurements have also been used in location fingerprinting methods. For example, in UWB indoor positioning, a map of pre-observed received signal strength (RSS) values has been used to match against current measurements to estimate position [35]. A similar technique is shown in [72] that estimates position based on features of wideband channel impulse responses in a mine. These methods use pattern matching to determine position. In this chapter, the idea of using a particle filter framework that incorporates a map of pre-observed measurement *noise* is introduced. This allows the filter to adapt to local variations in measurement noise.

3.2 Dynamic Model

For tracking purposes, a two-dimensional constant velocity dynamic model is used. Equation 3.1 shows the state space variable $\mathbf{x}_t$ for this type of model. It has four components: the two-dimensional position at time t, x_t and y_t, and the two-dimensional velocity at time t, $\dot{x}_t$ and $\dot{y}_t$.

$$\mathbf{x}_t = \begin{bmatrix} x_t \\ \dot{x}_t \\ y_t \\ \dot{y}_t \end{bmatrix} \tag{3.1}$$

Equation 3.2 gives the function $\mathbf{f}$ that governs state transitions for this model where δ_t is the sensing interval and σ_d is the standard deviation of the zero mean, normally distributed dynamic noise. Throughout this work, the sensing interval is assumed to be 1. From $\mathbf{f}$, the state space equations for this model can be written as shown in Equation 3.3.

$$\mathbf{f} = \begin{bmatrix} x_t = x_{t-1} + \delta t \cdot \dot{x}_{t-1} \\ \dot{x}_t = \dot{x}_{t-1} + \mathcal{N}(0, \sigma_d) \\ y_t = y_{t-1} + \delta t \cdot \dot{y}_{t-1} \\ \dot{y}_t = \dot{y}_{t-1} + \mathcal{N}(0, \sigma_d) \end{bmatrix} \tag{3.2}$$

$$\mathbf{x}_t = \mathbf{f}(\mathbf{x}_{t-1}, \sigma_d) \tag{3.3}$$

3.3 Measurement Noise Map Augmented Particle Filter

This work proposes the use of a measurement noise map, described in Section 2.7, within the weight update phase of the BPF. This will be referred to as the measurement noise map augmented particle filter (MNMAPF). The use of weighted sums of Gaussians to approximate multi-modal noise distributions in a particle filter was previously considered in [65], where examples were shown for both dynamic and measurement noise. Our filter is similar to this approach in that it uses weighted sums of Gaussians to approximate multi-modal measurement noise distributions. However, our approach uses a facility-wide map to account for location-dependent differences in measurement noise. It is important to note that our map-based method can be used with measurement noise models other than sums of Gaussians. Furthermore, our method could be applied to problems other than UWB position tracking. The key is to capture location-dependent differences in measurement noise in the map prior to filtering and then apply it as shown here.

Similar to the BPF described in Section 1.5.7, the MNMAPF approximates complex distributions using a set of particles. A set of particles is a collection of M state space variables with a weight assigned to each [67]. A distribution is approximated by a set of particles χ, shown in Equation 3.4, where M is the number of particles, $\mathbf{x}_t^m$ is the state of particle m and w_t^m is the weight assigned to particle m, both at time t.

$$\chi = \{\mathbf{x}_t^m, w_t^m\}_{m=1}^{M} \tag{3.4}$$

The particle states are updated according to the state transition equations $\mathbf{f}$ as shown in Equation 3.2. This is a two-dimensional, constant velocity dynamic model. The prior importance function is chosen to simplify the sequential importance sampling weight update equation to that shown in Equation 3.5 where w_{t-1}^m is the weight of particle m at time $t-1$ and $p(\mathbf{z}_t|\mathbf{x}_t^m)$ is the probability of the measurement $\mathbf{z}_t$ given the state of particle m, all at time t.

$$w_t^m = w_{t-1}^m \cdot p(\mathbf{z}_t|\mathbf{x}_t^m) \tag{3.5}$$

The measurement noise model used in the weight update step of the MNMAPF is selected from the measurement noise map based on the location components of the mth particle's state. More simply stated, the model parameters for the map position nearest the particle location are

used in the weight update step. Equations 3.6 and 3.7 show analytically how $p(\mathbf{z}_t|\mathbf{x}_t^m)$ is generated using our map-based measurement noise model where $p_i(\mathbf{z}_t|\mathbf{x}_t^m)$ is the unimodal Gaussian PDF for each cluster at the map location nearest $\mathbf{x}_t^m$.

$$p(\mathbf{z}_t|\mathbf{x}_t^m) = p_{\boldsymbol{\nu}}(\mathbf{z}_t|\mathbf{x}_t^m) = \sum_{i=1}^{I_{\mathbf{x}}} \omega_{\mathbf{x}_t^m,i} \cdot p_i(\mathbf{z}_t|\mathbf{x}_t^m) \tag{3.6}$$

$$p_i(\mathbf{z}_t|\mathbf{x}_t^m) = \frac{1}{2\pi\sqrt{|\Sigma_{\mathbf{x}_t^m,i}|}} e^{-\frac{1}{2}(\mathbf{z}_t-\boldsymbol{\mu}_{\mathbf{x}_t^m,i})^T \Sigma^{-1}_{\mathbf{x}_t^m,i}(\mathbf{z}_t-\boldsymbol{\mu}_{\mathbf{x}_t^m,i})} \tag{3.7}$$

Next, the particle weights are normalized and the expected value is computed using Equations 3.8 and 3.9 respectively. Finally, the coefficient of variation (CV) and effective sample size (ESS) are computed [47] and resampling is performed if necessary. The sampling method that we have chosen is referred to as "select with replacement" by Rekleitis in [48].

$$w_t^m = \frac{w_t^m}{\sum_{\hat{m}=1}^{M} w_t^{\hat{m}}} \tag{3.8}$$

$$E(\mathbf{x}_t) = \sum_{m=1}^{M} w_t^m \cdot \mathbf{x}_t^m \tag{3.9}$$

The CV and ESS are calculated according to Equations 3.10 and 3.11. Throughout this work, resampling is performed when the ESS is determined to be less than $0.5 \times M$, i.e. half of the particle weights have gone to zero.

$$ESS = \frac{M}{1 + CV} \tag{3.10}$$

$$CV = \frac{1}{M} \sum_{m=1}^{M} (M \cdot w_t^m - 1)^2 \tag{3.11}$$

The MNMAPF was implemented in both the MATLAB and C languages. In MATLAB, the measurement noise model data is stored in a number of matrices including a two-dimensional matrix indicating the number of clusters found at each location, a two-dimensional matrix indicating the weight value for each cluster at all locations, two three-dimensional matrices storing the x and y mean values for each cluster at all locations, and a four-dimensional matrix storing the 2×2

Table 3.1: Ground truth range covered by the recordings and corresponding velocities in cm/s.

Trial	Range	Velocity
1	(480, 570) - (480, 710) cm	20 cm/s
2	(460, 630) - (320, 630) cm	16 cm/s
3	(600, 390) - (390, 630) cm	76 cm/s
4	(390, 600) - (630, 390) cm	70 cm/s

covariance matrix for each cluster at all locations. In the C implementation, this data is stored in a number of text files. At this time, the basic particle filter algorithm is much more efficient that the MNMAPF partially due to the method used to search for the nearest location. However, the MNMAPF will always be somewhat slower than the BPF due to the increased complexity that a multi-modal measurement noise model requires.

3.4 Error Metric

The metric that will be used to compare filter performance throughout this work is referred to as the average error e and is calculated using the Euclidean distance between a ground truth location and its corresponding filter output. The calculation is performed as shown in Equation 3.12 where x_n and y_n are the nth filter output and $\hat{x}_n$ and $\hat{y}_n$ are the corresponding ground truth location.

$$e = \frac{1}{N} \sum_{n=1}^{N} \sqrt{(x_n - \hat{x}_n)^2 + (y_n - \hat{y}_n)^2} \tag{3.12}$$

3.5 Dynamic Track Collection

Four tracks are defined within the trackable area of the Riggs facility. Table 3.1 gives the ground truth coordinates of the tracks and the average velocity of the tag while traversing the track. Figure 3.1 shows a plot of each track within the test facility. Five recordings are made of tracks 1, 2 and 4 and four of track 3. Tracks 3 and 4 cover the same ground truth coordinates; track 3 runs northwest and track 4 runs southeast.

Tracks 1 and 2 are collected by dragging the UWB tag across the top of the tag stand shown in Figure 2.13. The tag stand is placed at a known ground truth location within the trackable area in the same manner as described for model data collection in Section 2.3. Tracks 3 and 4 are collected

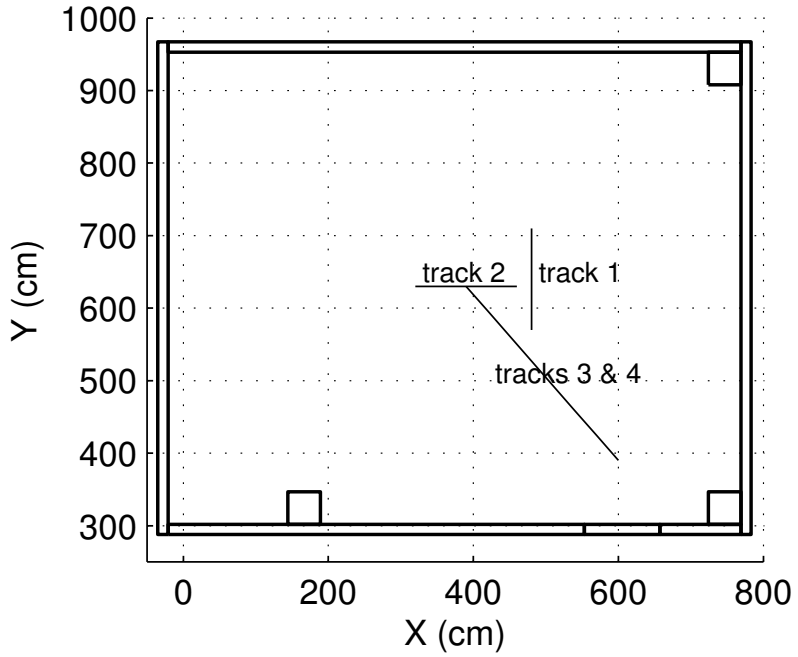

Figure 3.1: Plot of the ranges covered by tracks 1 - 4.
Experiments recorded in the Riggs facility.

by placing the UWB tag on a cart. This cart is then moved along a known ground truth path. The UWB tags are left in place for a period of time at the beginning and end of the path to allow for starting and stopping of measurement recording. Figure 3.2 shows the raw measurement data in the Y direction collected for Track 1. The measurements corresponding to times when the tag is stationary are shown in ellipses 1 and 3. The measurements corresponding to times when the tag is in motion in the y direction are shown in ellipse 2.

To ensure accurate error calculation for measurement and particle filter outputs, the ground truth for the dynamic tracks must also be accurate. Therefore, the stationary periods within each recording must be removed (those within ellipses 1 and 3 of Figure 3.2). This is done by fitting three lines to the measurements. First, a line is fit to the first few points of the recording which are always stationary. Second, a line is fit to the last few points of the recording which should also always be stationary. Third, a line is fit to the middle few points which should correspond to tag motion. Finally, points between the intersection of the first and middle lines and the intersection of the middle and last lines are stored as the portion of the recording that is in motion. Figure 3.3 shows these lines for a set of measurements from Track 1.

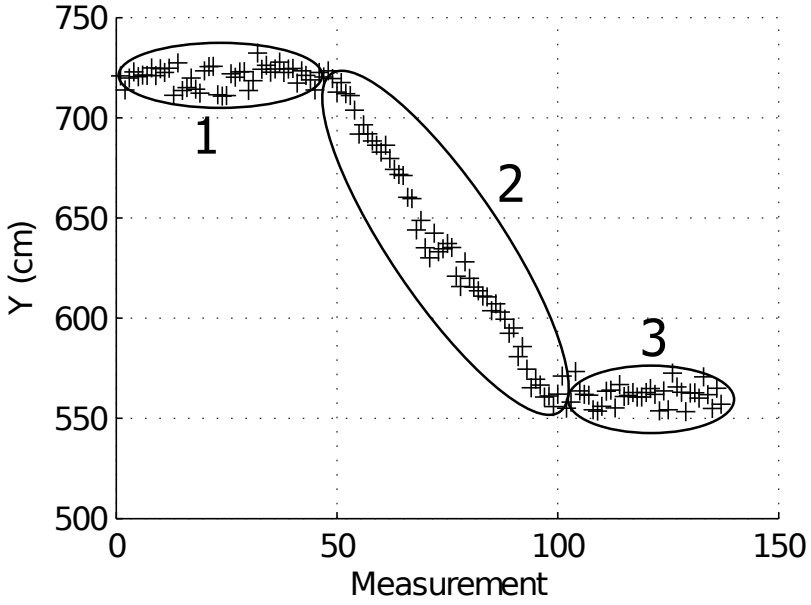

Figure 3.2: Raw measurement data in the y direction collected over Track 1. Ellipse 2 shows the measurements taken while the tag is in motion. Ellipses 1 and 3 show the measurements taken while the tag is stationary.

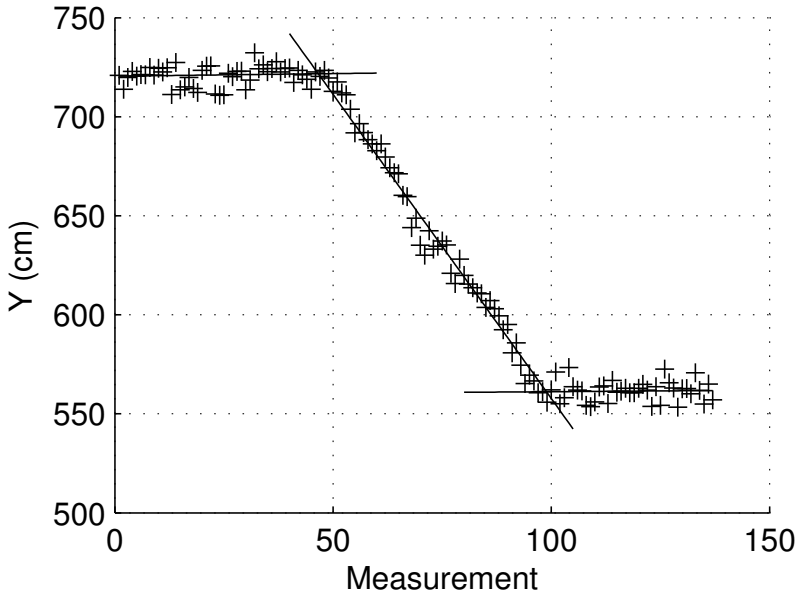

Figure 3.3: Plot of the line fitting for removal of measurements before and after the dynamic motion of the tag over Track 1.

The intersections of the lines are visually identified and the measurements closest to the intersections are selected as the start and end measurements of the recording. Because the tag is moved at constant velocity (as close as manually possible), each measurement is associated with a ground truth location by dividing the path traversed evenly by the number of measurements.

3.6 Dynamic and Measurement Noise

As discussed in Section 3.2, a two-dimensional constant velocity dynamic model is used in this work. This model requires a dynamic noise value as input. The dynamic noise is a sample from a zero mean, normally distributed random variable with standard deviation σ_d. It is added to the velocity component of the state space variable and is, therefore, noise on acceleration. Because the velocity of the tag is not known a priori, the particle states are initialized with zero velocity. The σ_d value affects how quickly the filter can react to changes in tag motion. A larger value of σ_d allows the dynamic model to react quickly to changes in velocity, while a lower value makes the model react more slowly. Figure 3.4 shows the effect that increasing σ_d has on the output of a basic particle filter. When σ_d is small, the filter output does not move much from the initial location. As σ_d increases, more particles reach the true velocity of the system quicker and the filter output moves more with each measurement. Large σ_d values will force the filter output to closely match the raw measurements.

The measurement noise covariance matrix Σ_n used throughout this work is shown in Equation 3.13. The value 49 was chosen for both variance values because that is the average variance of the clusters found in the portion of the test area where the tracks were taken. This results in σ_d values of 7. This matrix is used in the basic particle filter as shown in Equation 1.20.

$$\Sigma_n = \begin{bmatrix} 49 & 0 \\ 0 & 49 \end{bmatrix} \tag{3.13}$$

3.7 Filtering Results

Figure 3.5 shows the average output for ten iterations of the BPF and MNMAPF for one recording of Track 1. The MNMAPF has an average error 3 cm less than the BPF output.

Figure 3.6 shows the average output for ten iterations of the BPF and MNMAPF for one

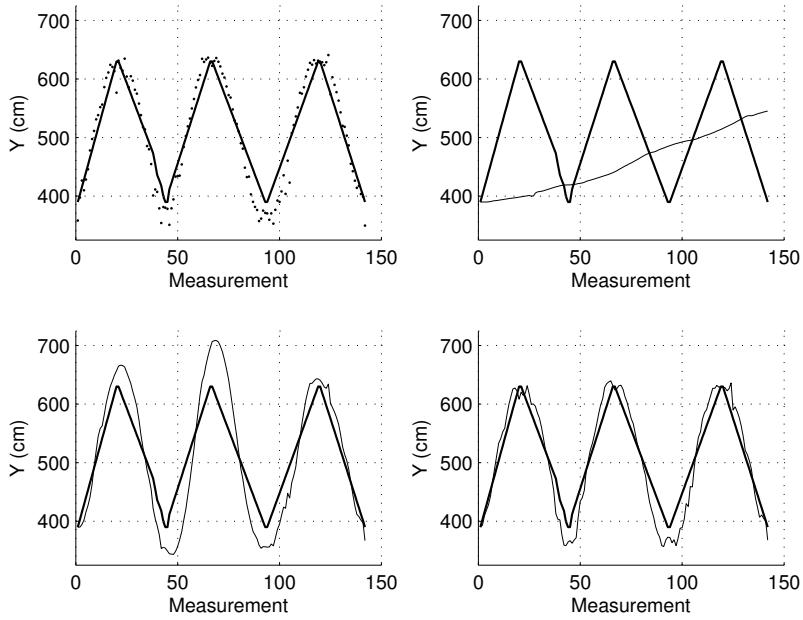

Figure 3.4: Plot of raw measurements (top left) and plots of BPF output with varying dynamic noise values, 0.1 (top right), 2.0 (bottom left), and 5.0 (bottom right). Ground truth indicated by thick line. BPF output indicated by thin line.

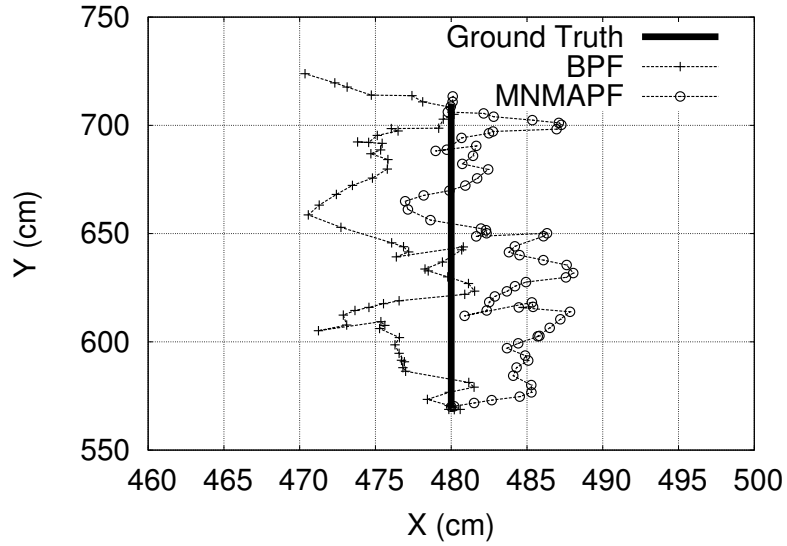

Figure 3.5: Plot of BPF ($\sigma_d = 0.7$) and MNMAPF ($\sigma_d = 0.4$) outputs for Track 1 with 9.3 cm and 6.4 cm average error respectively.

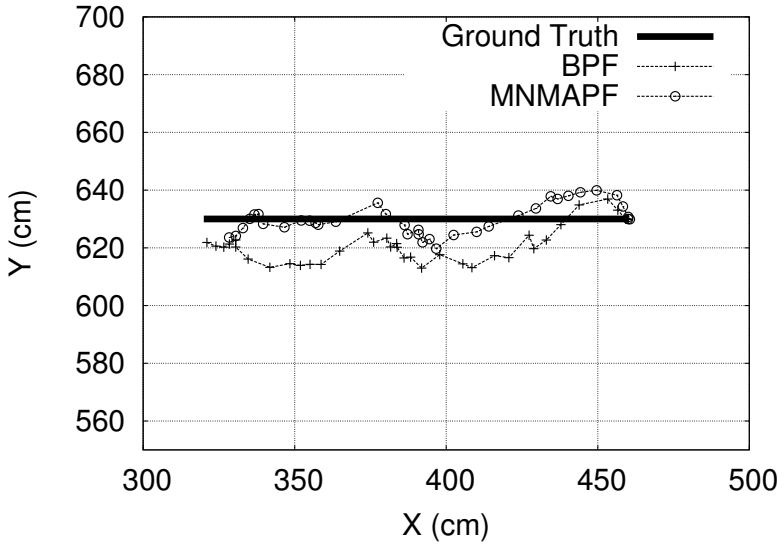

Figure 3.6: Plot of BPF ($\sigma_d = 1.3$) and MNMAPF ($\sigma_d = 1.1$) outputs for Track 2 with 11.0 cm and 6.8 cm average error respectively.

recording of Track 2. This example shows one benefit of the map-based measurement noise model. It can correct for overall biases in the measurements at a certain location. This can be seen by the overall shift that is seen in the left half of the filter output. The MNMAPF output tracks much closer than the BPF in this area. The average error is over 5 cm lower for this example.

Figures 3.7 and 3.8 again show the average output for ten iterations of the BPF and MNMAPF for one recording each of Tracks 3 and 4 respectively. The MNMAPF's ability to adjust to measurement biases can again be seen in the large reduction in error in the southeast portion of both examples. The MNMAPF tracks much closer to the ground truth in these locations. The average error improvement is 6 cm and 11 cm respectively.

3.8 Performance Summary

Figure 3.9 shows the average error over all recordings of the four tracks after 300 iterations of the BPF and MNMAPF over a range of σ_d values along with the raw measurement error. The plot shows that the MNMAPF achieves a lower average error value than the BPF and also a lower average error than the raw measurements. The average minimum MNMAPF error over the 19 recordings is approximately 17 cm which is a 3 cm, or 15%, improvement on the average raw measurement error

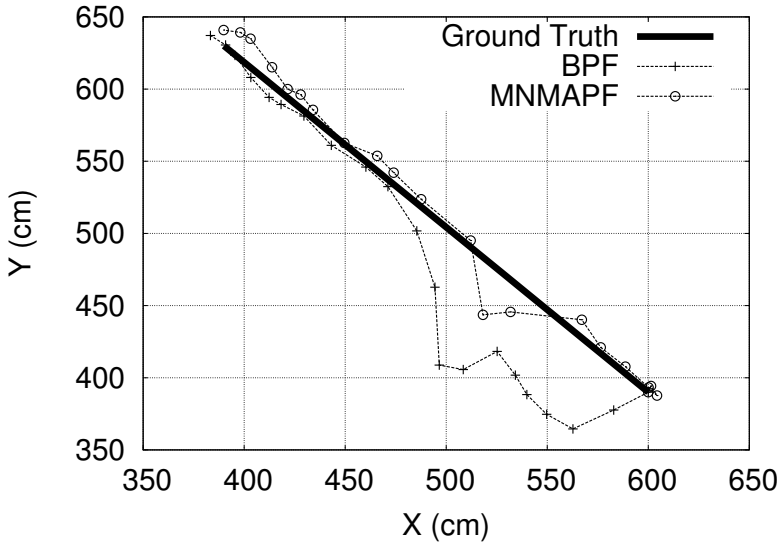

Figure 3.7: Plot of BPF ($\sigma_d = 8.0$) and MNMAPF ($\sigma_d = 8.5$) outputs for Track 3 with 34.8 cm and 28.8 cm average error respectively.

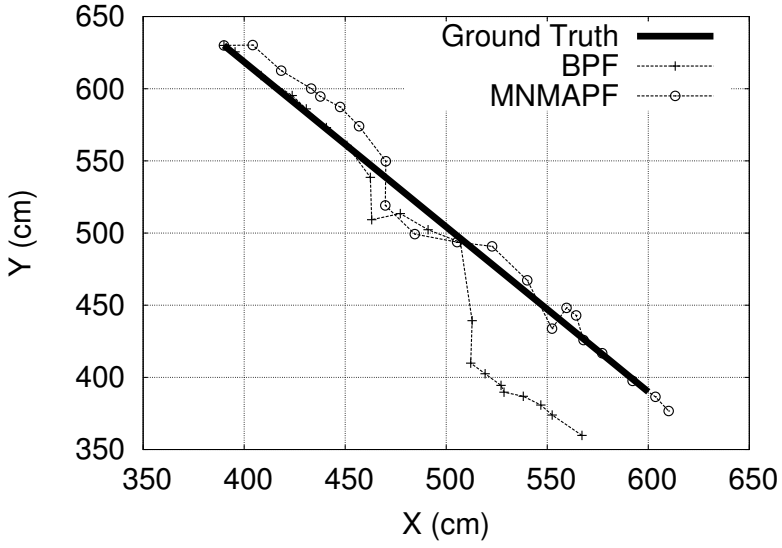

Figure 3.8: Plot of BPF ($\sigma_d = 7.6$) and MNMAPF ($\sigma_d = 7.5$) outputs for Track 4 with 28.9 cm and 17.5 cm average error respectively.

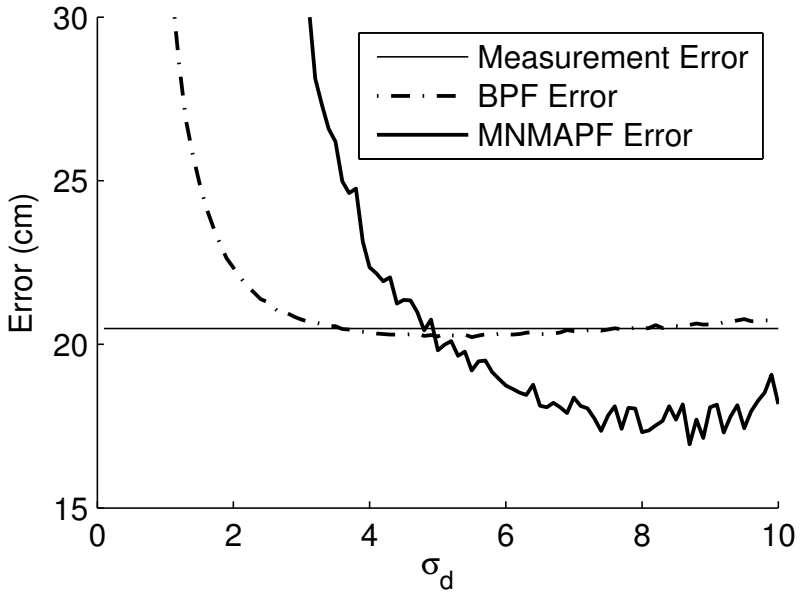

Figure 3.9: Plot of average error for varying σ_d.

of 20 cm. The low average raw measurement error value is a product of the fact that the portion of the test area where recordings were taken has the lowest average raw measurement error of the entire facility.

3.9 Particle Filter Conclusions

This chapter has presented a method for integrating a map of UWB measurement noise into a particle filter framework to improve indoor position tracking accuracy. A 15% reduction in tracking error is shown through the use of the measurement noise map in the context of a particle filter.

A limitation of our method is the requirement that the measurement noise map be re-calculated after a significant change to the positioning system installation or environment occurs. Because of this, it is expected that this type of map would be generated for a system once and used for a long period of time. Furthermore, the author acknowledges that a significant time commitment is required to generate the measurement noise map. The development of more automated methods to generate the measurement noise map could significantly reduce this time commitment and allow for the measurement noise model to be recalculated on a more frequent basis if necessary. It may be

that floorplan and sensor geometry information could be used to semi-automate this process similar to the techniques shown in [53, 73]. The next chapter looks at improving indoor position tracking accuracy by optimizing system configuration using floorplan and sensor geometry information.

Chapter 4

Configuration Optimization

As described previously in Chapter 2, a number of possible sources of noise effect the performance of UWB indoor position tracking systems including NLOS, multipath and synchronization. In Chapter 3, the measurement noise map augmented particle filter (MNMAPF) was presented which uses a map of environment noise to improve overall system tracking performance without considering the underlying causes of measurement error. In this chapter, a metric is proposed that can be used to quantify expected system performance based on sensor location, sensor orientation and facility floorplan. This metric can also be used to identify areas within an installation that are more susceptible to error. Using this metric, a procedure is developed to determine the parameters, i.e. sensor position, sensor orientation and potentially others, of the physical installation of the UWB tracking system that will produce minimum measurement error based on sensor geometry and physical facility constraints.

4.1 Related Work

A number of other works have considered optimal sensor placement to minimize position error. A bound on localization performance for a single location is derived by Jourdan, et al. in [74]. This bound is referred to as the position error bound (PEB). The PEB takes into account the distance from the sensor to the location of the object being tracked as well as the LOS/NLOS conditions. Range measurements are modeled as the true distance plus a bias term plus a sample from a zero-mean Gaussian random variable. The bias term is added to account for NLOS conditions

between the transmitter and receiver. In LOS conditions, this bias term goes to zero. Furthermore, the variance of the Gaussian random variable increases as distance increases. This effectively weights range measurements that are used for localization according to their quality. In [75], the PEB is extended to multiple locations in a facility through the concept of localization accuracy outage. Localization accuracy outage is a threshold on PEB values that gives an idea of the quality of localization throughout an area. PEB and localization accuracy outage are also presented in [76]. Optimization of sensor placement using the PEB is considered by Jourdan and Roy in [77]. An iterative coordinate-descent algorithm, referred to as RELOCATE, is developed that determines the optimal sensor locations to minimize the average PEB at multiple locations. Similar to the PEB-based work, Martínez and Bullo develop a method for determining optimal sensor placement using the Fisher information matrix in [78]. Sinha, et al. [79] use Newton-Raphson method in combination with a genetic algorithm to find the global maximum of their objective function obtained from the Fisher information measure. Hegazy and Vachtsevanos [80] present a method for determining the minimum number of sensors required for localization and an optimal sensor placement for a single location. The placement is optimal in the sense that it minimizes the localization error bound by minimizing the condition number of the matrix of sensor positions. This work performs localization using received signal strength measurements in simulation only. Similar work has been performed for GPS by McKay and Pachter in [81].

All of the related work is performed in simulation and no comparisons have been made to the performance of any real positioning systems. Furthermore, none of the methods take into account sensor orientation relative to the object being tracked, which is an important element of a real world localization system, especially one using angle-of-arrival techniques.

4.2 Facility-Wide Error

Using the data collected to generate the measurement noise map described in Section 2.7, a plot of the normalized average Euclidean error, e_{avg}, was generated as shown in Figure 4.1. Error was calculated as the Euclidean distance from the measurement to the known ground truth location, as shown in Equation 3.12, and averaged over 500 measurements at each location. The average error found across the facility is approximately 60 cm. The minimum average error is 4 cm and the maximum average error is 1922 cm. For ease of visualization, average error at each location is

capped at 100 cm, i.e. everything greater than 100 cm is truncated to 100 cm. Normalization is performed by first subtracting the minimum facility-wide average error from each location and then dividing by the 100 cm error cap leaving the values ranging between 0 and 1. Darker areas of Figure 4.1 indicate more error. From Figure 4.1, it can be seen that some areas of the facility are prone to larger error magnitudes than others. The eight UWB receiver positions are indicated by the filled squares and the orientation of each receiver is indicated by the line projecting from the square.

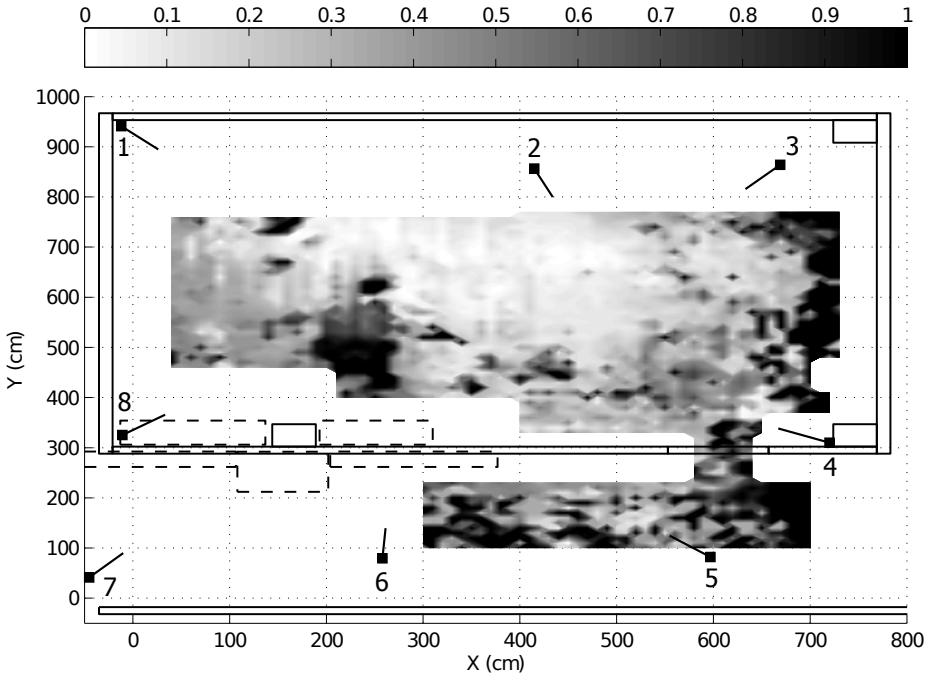

Figure 4.1: Normalized average error across the facility.

Figure 4.2 is a visually segmented version of Figure 4.1 based on average error with numbered segments. Each of these segments identifies an area that contains a certain quality of measurements denoted as either poor, average or good in terms of average error. Table 4.1 indicates the quality of measurement identified in each segment of Figure 4.2. The measurement error clearly varies in quality across the facility.

Because the measurement error varies significantly depending on the location of the transmitter tag within the facility, it is believed that features of the test facility itself, as well as the UWB tracking system's physical installation, are major contributing factors to measurement error. Therefore, the author seeks to find facility and environment-based metrics that account for this

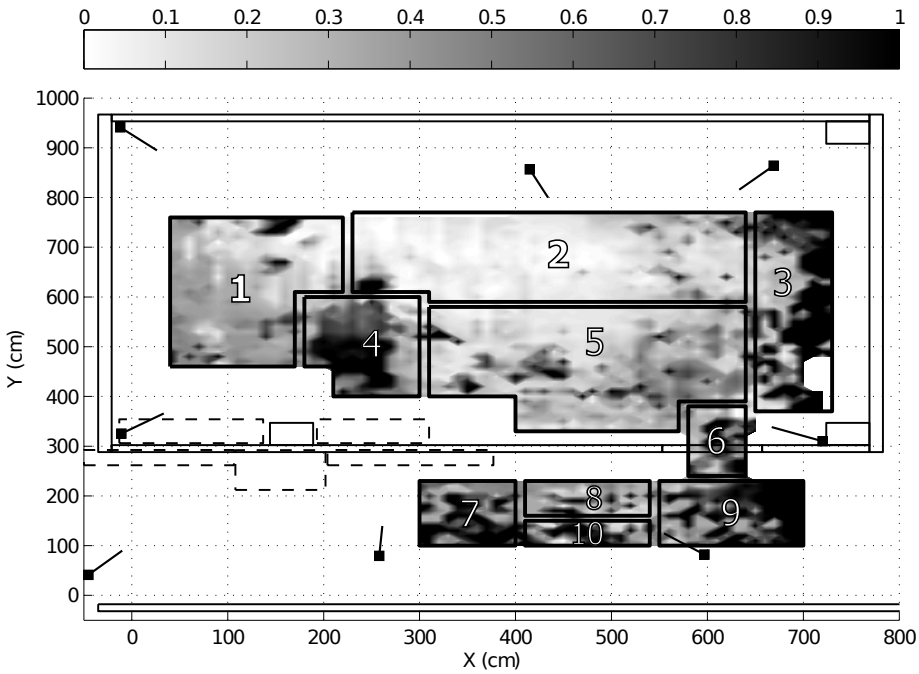

Figure 4.2: Average error across the facility, visually segmented. Numbers near filled squares indicate the sensor identification number.

Table 4.1: Quality of measurements based on average error for each segment identified in Figure 4.2.

	Segment									
	1	2	3	4	5	6	7	8	9	10
Good		X								
Average	X				X			X		
Poor			X	X		X	X		X	X

variance in measurement error.

4.3 Sensor Set Selection

The UWB localization system used in this work estimates the location of transmitter tags by determining the angle-of-arrival (AOA) and time-difference-of-arrival (TDOA) of an UWB pulse at a number of fixed receivers. Using these values, multiangulation or multilateration is performed to estimate the transmitter tag's position. Therefore, as few as two receivers can be used to calculate the position estimate [82]. A set of eight receivers or sensors, $S = \{s_i\},\ i = 1, \ldots, 8$, is installed within the test facility. The position estimation procedure can be performed using more than the minimum number of receivers and, in many cases, position estimation is improved when more measurements are used to estimate position. Due to computational time requirements, the system limits the number of measurements to only five sensors. The five sensors that will be used are selected based on the received signal strength measurement at each receiver. More specifically, the five receivers that measure the greatest received signal strength value are used to estimate transmitter position. Because of this, all metric calculations performed in this section include information from only the five "best" sensors relative to the current transmitter position. This best set of five sensors will be denoted as S_b.

For the experiments reported in this chapter, we simulate the process of selecting S_b as follows. The best set of five sensors, S_b, is determined by calculating the Euclidean distance from all eight sensors to the current transmitter location and adding to it a penalty for the portion of transmission that is through a wall or other obstacle. This value will be referred to as radio frequency (RF) range, $\tilde{r}$. The Euclidean distance $d_{c,i}$ between the current transmitter location, (x_c, y_c, z_c) cm, and each sensor's location, (x_i, y_i, z_i) cm, is calculated as shown in Equation 4.1.

$$d_{c,i} = \sqrt{(x_c - x_i)^2 + (y_c - y_i)^2 + (z_c - z_i)^2} \tag{4.1}$$

The RF range is an estimate of the range measurement that the system would generate between a tag location and a fixed sensor. This estimate takes into account non-line-of-sight (NLOS) conditions. It is calculated as shown in Equation 4.2 where δ is the through-wall distance (explained in more detail in Section 4.4.2), V is the speed of light in concrete, and C is the speed of light in air. Therefore, the best five sensors at location (x_c, y_c, z_c) cm are those that produce the five lowest

values of $\tilde{r}$.

$$\tilde{r}_{c,i} = d_{c,i} + \left(\frac{\delta_{c,i}}{V} - \frac{\delta_{c,i}}{C} \right) C \tag{4.2}$$

The value of the speed of light in air C used in this work is $299,792,458$ m/s. The value of the speed of light in concrete is calculated from C using the real portion of the refractive index, 2.55, reported by Sato, et al. in [83]. This yields a value of $V = 117,565,670$ m/s for the speed of light through concrete. This value is simply an estimate used for metric calculation. It is not intended to be an exact representation of the NLOS range measurement.

4.4 Metrics

It is widely known that sensor geometry [76] and NLOS conditions [58, 40, 54, 51] affect radio frequency position estimation. Therefore, a number of metrics have been identified that can be calculated based on facility floorplan and sensor location information. These metrics are linked with measurement error and account for sensor geometry and NLOS conditions.

4.4.1 RF Range

Gezici, et al. [84] have shown that the variance of radio frequency range estimates increases with distance using the Cramer-Rao lower bound (CRLB). In turn, the bound on position estimation error will also increase as the distance to the sensors used to estimate position increases. Therefore, the RF range $\tilde{r}_{c,i}$ to the sensors in set S_b used in calculating the position estimate will affect the position estimation error. The total RF range metric at the current transmitter location $\tilde{r}_c$ is calculated as shown in Equation 4.3 where $\tilde{r}_{c,S_b(i)}$ is the distance from the current transmitter location to the ith sensor of set S_b and is calculated as shown in Equation 4.2. Figure 4.3 gives plots of the RF range for each sensor at all of the locations within the Riggs facility. Notice that this metric takes into account not only distance from each sensor but also NLOS conditions.

$$\tilde{r}_c = \sum_{i=1}^{5} \tilde{r}_{c,S_b(i)} \tag{4.3}$$

Figure 4.4 is a map of the total RF range to the best five sensors for locations within the test facility. The darker areas indicate locations with the greatest total RF range. It can be seen

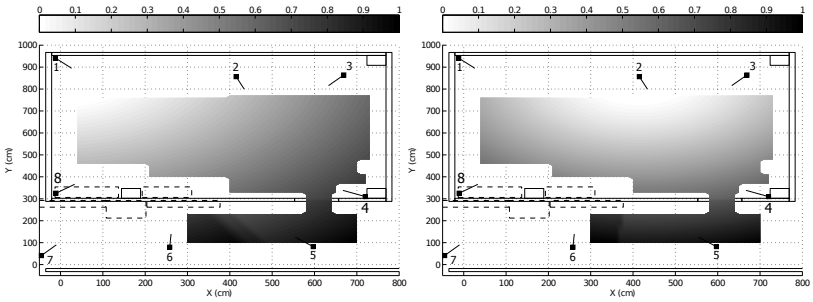

(a) Sensor 1

(b) Sensor 2

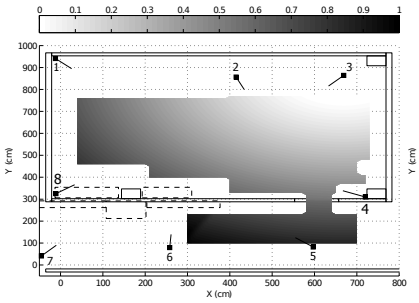

(c) Sensor 3

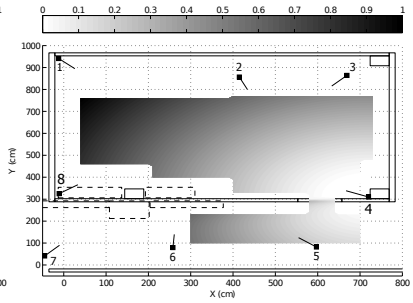

(d) Sensor 4

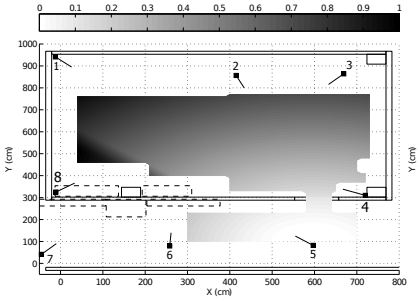

(e) Sensor 5

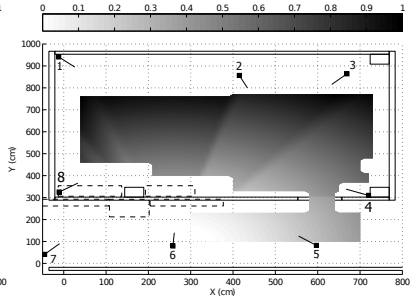

(f) Sensor 6

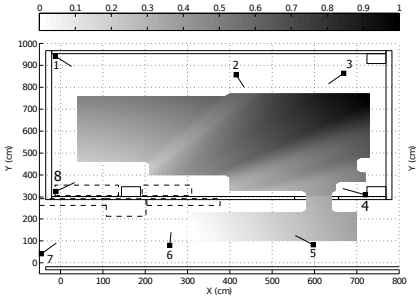

(g) Sensor 7

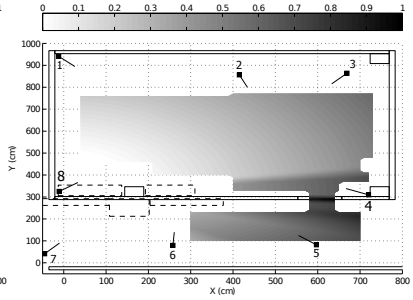

(h) Sensor 8

Figure 4.3: The total RF range for each sensor individually.

that, similar to the average error plot shown in Figure 4.1, the areas with the greatest RF range to all sensors are concentrated around the edge of the facility. Specifically, the total RF range metric has low values in areas corresponding to segments 2 and 5 of Figure 4.2.

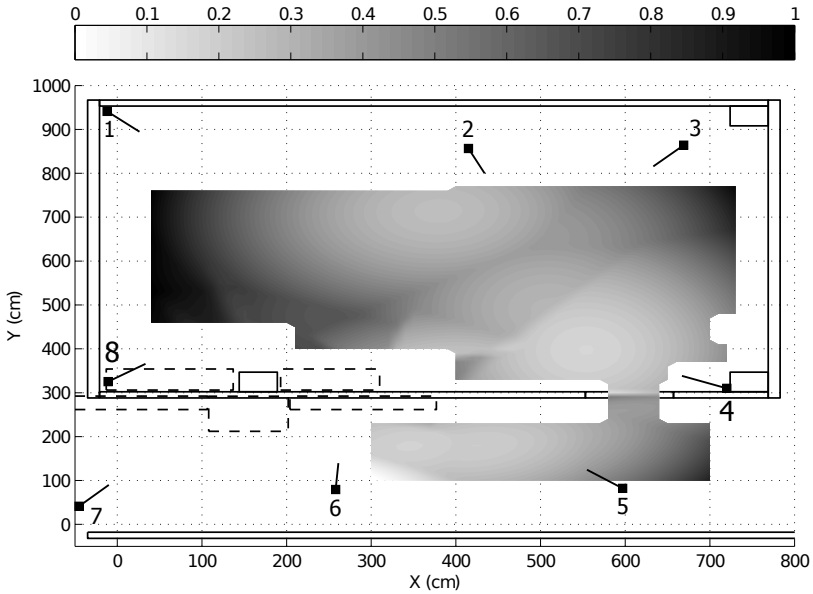

Figure 4.4: Total RF range for the best five sensors at each position.

4.4.2 Through-Wall Distance Metric

NLOS propagation has been shown to generate positive range biases in UWB systems due to the slower rate of RF propagation through mediums other than air [54]. These range biases produce position estimation errors after multilateration or multiangulation. Sensors with a clear line-of-sight (LOS) path to the transmitter tag will generate more accurate range estimates than obstructed sensors, all other things being equal. NLOS conditions within the test facility are quantified by calculating the total obstructed distance between a transmitter and each of the best five receivers. This metric is referred to as through-wall distance, $d_{tw,c}$. First, the number of obstructions, W_i, that the line between the current transmitter location, (x_c, y_c, z_c), and a particular sensor, i in S_b, passes through is determined geometrically. Then, the point where the line enters obstruction j, $(x_{S_b(i),j,e}, y_{S_b(i),j,e}, z_{S_b(i),j,e})$ and the point where the line leaves obstruction j, $(x_{S_b(i),j,l}, y_{S_b(i),j,l}, z_{S_b(i),j,l})$, is determined. The distance between the entering and leaving points is

calculated and summed for each obstruction j and sensor i in S_b according to Equation 4.4.

$$d_{tw,c} = \sum_{i=1}^{5} \sum_{j=1}^{W_i} \sqrt{(x_{S_b(i),j,e} - x_{S_b(i),j,l})^2 + (y_{S_b(i),j,e} - y_{S_b(i),j,l})^2 + (z_{S_b(i),j,e} - z_{S_b(i),j,l})^2} \quad (4.4)$$

Obstructions include walls and furniture. Figure 4.1 denotes walls with solid lines and other obstructions with dashed lines. Figure 4.5 shows the total through-wall distance to locations within the Riggs facility for each of the eight installed sensors. Locations with higher through-wall distances are shown darker. It can be seen from these figures that sensors on the other side of a wall or obstruction produce a higher value of through-wall distance, as expected.

A more complete picture of the through-wall distance metric can be seen by summing the through-wall distance of the best five sensors for each location and displaying in a similar manner. Figure 4.6 shows a plot of the total through-wall distance metric across the test facility for the best five sensors. It can be seen from this figure that a large portion of the test area has zero through-wall distance. However, other areas, such as between 300 and 400 cm in the x direction and 100 and 250 cm in the y direction, have much higher through-wall distance values. The area corresponding to segment 7 of Figure 4.2 clearly suffers from severe NLOS conditions based on the high values of $d_{tw,c}$ shown.

4.4.3 Position Dilution of Precision (PDOP) Metric

Geometric dilution of precision (GDOP) is a measure of observation geometry that has been used extensively to quantify position error in the Global Positioning System (GPS) [85]. More specifically, GDOP describes amount of change that occurs in the position estimate due to a small change in measured range data [86]. A small value of GDOP means that a small change in a range measurement yields a small change in the position estimate. A large value of GDOP means that a small change in a range measurement yields a large change in the position estimate. GDOP can take into account more variables than position, e.g. time. Position dilution of precision (PDOP) is limited to the position only. The lower the value of PDOP the better the sensor geometry. The PDOP metric for each transmitter location c used in this work is calculated according to Equations 4.5 - 4.7 where $(x_{S_b(i)}, y_{S_b(i)}, z_{S_b(i)})$ is the position of sensor i, (x_c, y_c, z_c) is the current position of the transmitter, $R_{S_b(i),c}$ is the distance between the current transmitter location and sensor i of S_b

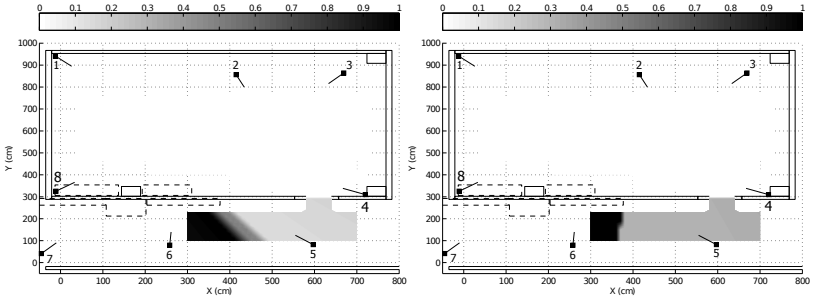

(a) Sensor 1

(b) Sensor 2

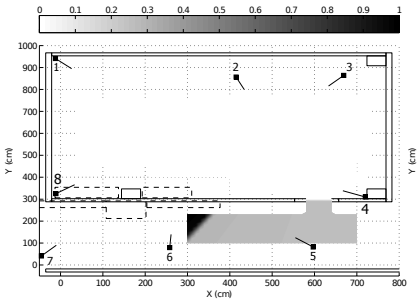

(c) Sensor 3

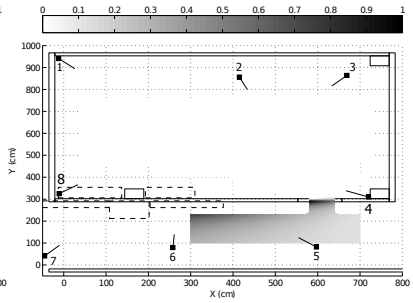

(d) Sensor 4

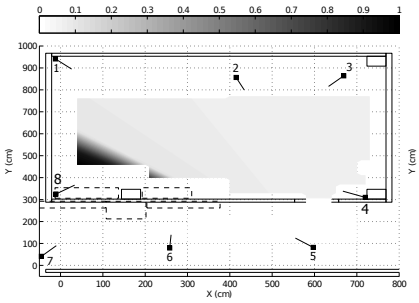

(e) Sensor 5

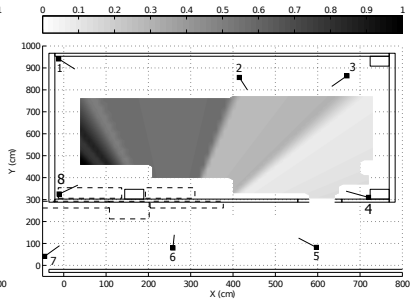

(f) Sensor 6

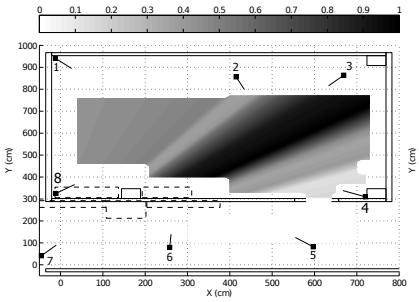

(g) Sensor 7

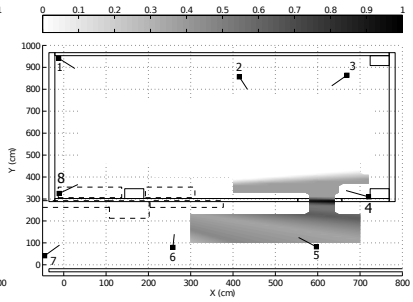

(h) Sensor 8

Figure 4.5: The total through-wall distance for each sensor individually.

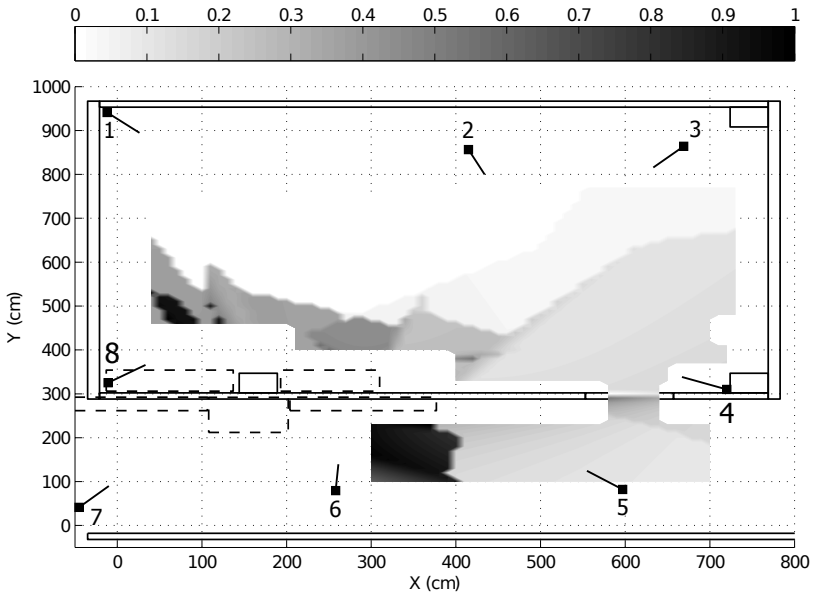

Figure 4.6: Total through-wall distance for the best five sensors at each position.

and $trace_3(\cdot)$ indicates only the first three elements of the trace [87]. There are five rows in matrix H_c of Equation 4.6 due to the five sensors in S_b. As can be seen from these equations, the PDOP metric is solely based on the position of the sensor in reference to the transmitter.

$$R_{S_b(i),c} = \sqrt{(x_{S_b(i)} - x_c)^2 + (y_{S_b(i)} - y_c)^2 + (z_{S_b(i)} - z_c)^2} \tag{4.5}$$

$$H_c = \begin{bmatrix} \frac{(x_{S_b(1)} - x_c)}{R_{S_b(1),c}} & \frac{(y_{S_b(1)} - y_c)}{R_{S_b(1),c}} & \frac{(z_{S_b(1)} - z_c)}{R_{S_b(1),c}} & 1 \\ \frac{(x_{S_b(2)} - x_c)}{R_{S_b(2),c}} & \frac{(y_{S_b(2)} - y_c)}{R_{S_b(2),c}} & \frac{(z_{S_b(2)} - z_c)}{R_{S_b(2),c}} & 1 \\ \frac{(x_{S_b(3)} - x_c)}{R_{S_b(3),c}} & \frac{(y_{S_b(3)} - y_c)}{R_{S_b(3),c}} & \frac{(z_{S_b(3)} - z_c)}{R_{S_b(3),c}} & 1 \\ \frac{(x_{S_b(4)} - x_c)}{R_{S_b(4),c}} & \frac{(y_{S_b(4)} - y_c)}{R_{S_b(4),c}} & \frac{(z_{S_b(4)} - z_c)}{R_{S_b(4),c}} & 1 \\ \frac{(x_{S_b(5)} - x_c)}{R_{S_b(5),c}} & \frac{(y_{S_b(5)} - y_c)}{R_{S_b(5),c}} & \frac{(z_{S_b(5)} - z_c)}{R_{S_b(5),c}} & 1 \end{bmatrix} \tag{4.6}$$

$$PDOP_c = \sqrt{trace_3((H_c^T H_c)^{-1})} \tag{4.7}$$

Figure 4.7 is a map of the PDOP for the best five sensors for each location within the Riggs facility. The darker areas indicate locations with the greatest PDOP. It can be seen from this figure that the greatest PDOP values are found in the area corresponding to segment 4 of Figure 4.2.

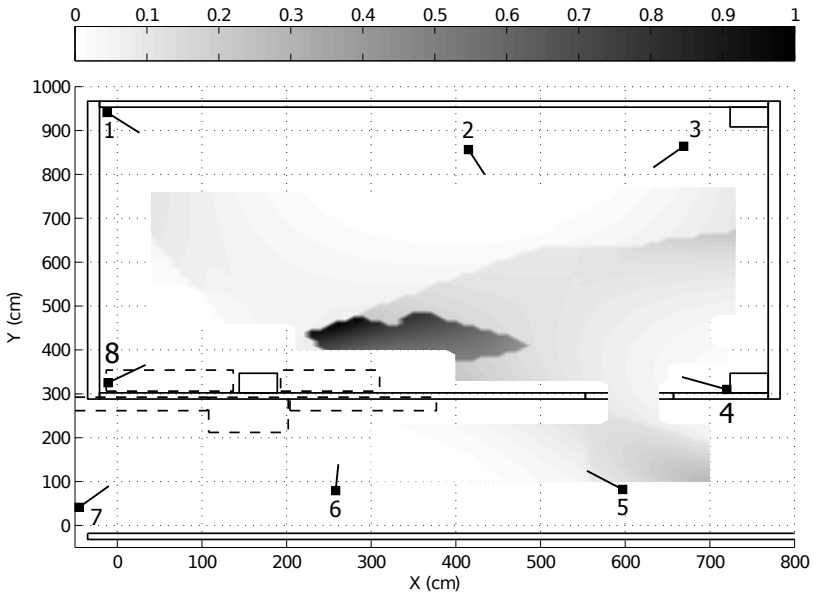

Figure 4.7: PDOP for the best five sensors at each position.

4.4.4 Sensor Orientation

The UWB position tracking system used in this work estimates transmitter tag position using a combination of AOA and TDOA measurements [82]. The AOA measurements are performed using an antenna array located within the receiver. Therefore, sensor orientation affects measurement error. Each sensor has three orientation angles referred to as yaw θ, pitch γ and roll. Yaw is the angle of rotation around the vertical or z axis as shown in Figure 4.8a. Pitch is the angle of rotation around the horizontal axis as shown in Figure 4.8b. In this case, zero degrees in pitch lies within a plane parallel to the floor of the test facility. Roll is held constant at zero degrees for all sensors as required by the system installation instructions. The following sections describe the calculation of pitch and yaw angle metrics that are based on the absolute angle between the sensor orientation and the location of the UWB transmitter tag.

4.4.5 Yaw Metric

Yaw angle is a component of the sensor orientation. However, the yaw metric that is used in this work is based on the absolute angle between the sensor yaw and the line connecting the transmitter to receiver. Figure 4.8a denotes the yaw metric as Υ. For each location within the test

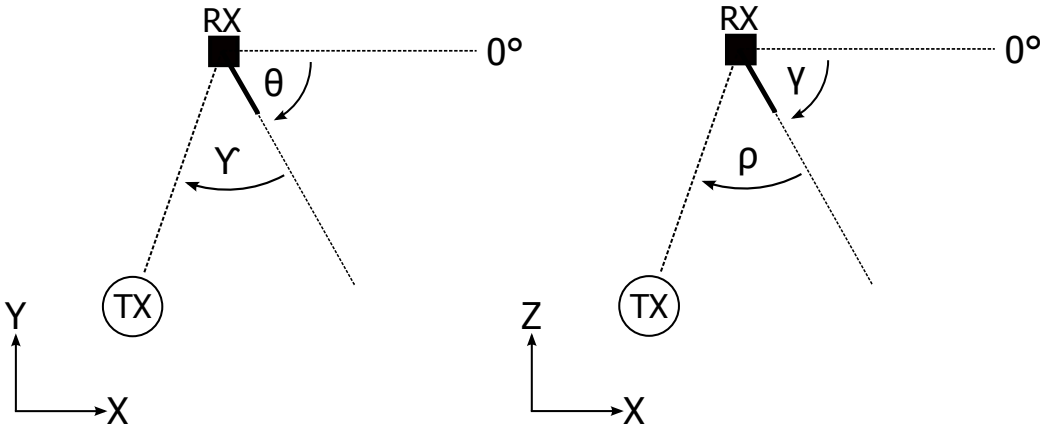

(a) Yaw angle (b) Pitch angle

Figure 4.8: Diagrams showing definitions of sensor yaw and pitch.

facility, the total yaw metric is calculated by summing the yaw metric for each of the five best sensors as shown in Equation 4.8 where $\Upsilon_{c,S_b(i)}$ is the angle between the current transmitter location and the yaw angle of each of the best five sensors. Figure 4.9 shows the total yaw metric calculated at each location within the test facility. It can be seen from this figure that the area with the minimum total yaw is located near the center of the main room and corresponds with segments 2 and 5 of Figure 4.2. Furthermore, the highest values of the yaw metric correspond to segment 9. Much of the rest of the test facility shows average values of the yaw metric.

$$\Upsilon_c = \sum_{i=1}^{5} \Upsilon_{c,S_b(i)} \tag{4.8}$$

4.4.6 Pitch Metric

Pitch angle is another component of the sensor orientation. Again, the pitch metric that is used in this work is based on the absolute angle between the sensor pitch and the line connecting the transmitter to receiver. Figure 4.8b denotes the pitch metric as ρ. For each location within the test facility, the total pitch metric is calculated by summing the pitch metric for each of the five best sensors as shown in Equation 4.9 where $\rho_{c,S_b(i)}$ is the angle between the current transmitter location and the pitch angle of each of the best five sensors. Figure 4.10 shows the total pitch metric calculated across the test facility. It can be seen from this figure that the areas with the highest values of the total pitch metric are located within the hallway and correspond to segments 6, 8, 9

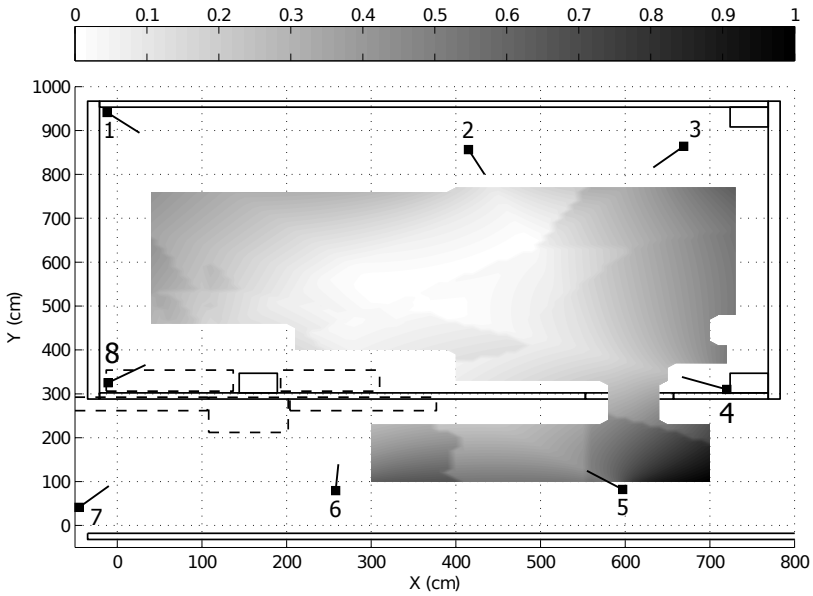

Figure 4.9: Total yaw metric for the best five sensors at each position.

and 10 from Figure 4.2.

$$\rho_c = \sum_{i=1}^{5} \rho_{c,S_b(i)} \tag{4.9}$$

4.5 Metric Combination

The five metrics described in the previous sections have been shown to correspond with segments of the average error figure. Table 4.2 summarizes which metrics best explain the segments shown in Figure 4.2. None of the metrics identified specifically correspond to segment 1 of Figure 4.2. However, segment 1 is of average quality and the PDOP, total yaw, and total pitch metrics all have average values in the area corresponding to segment 1. Figure 4.11 brings together the plots of each of the five metrics along with the segmented normalized average measurement error plot shown previously.

Although PDOP helps explain Segment 4, it was found that a calibration error accounted for the increased measurement error in this area. The calibration error affected the position and orientation angles stored in the system for sensor 1. After discovering the calibration error, data was recollected in the area of segment 4 and the old data was replaced. Figure 4.12 shows the

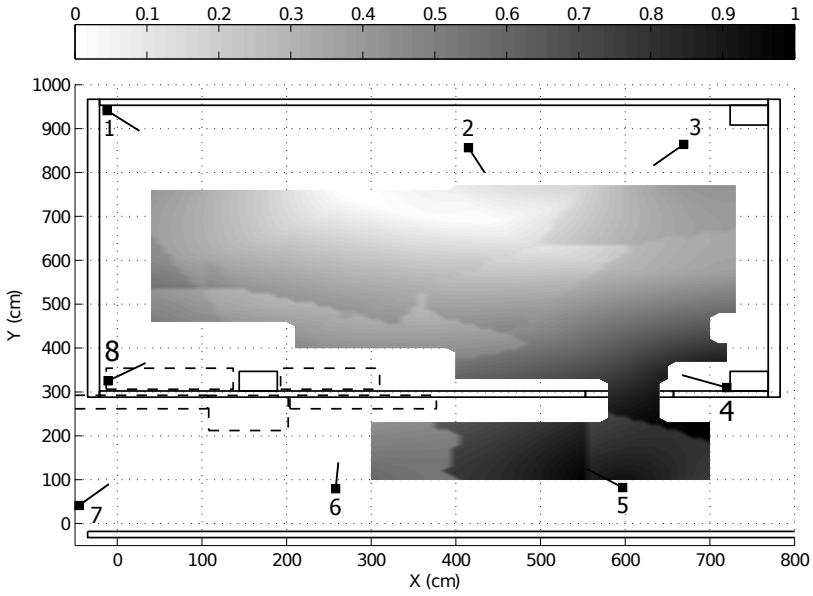

Figure 4.10: Total pitch metric for the best five sensors at each location.

Table 4.2: Metrics considered to minimize system error and the affected segments.

Metric	**Affected Segments**
RF Range	2, 5
Through-Wall Distance	7
PDOP	4
Yaw Angle	2, 5, 9
Pitch Angle	6, 8, 9, 10

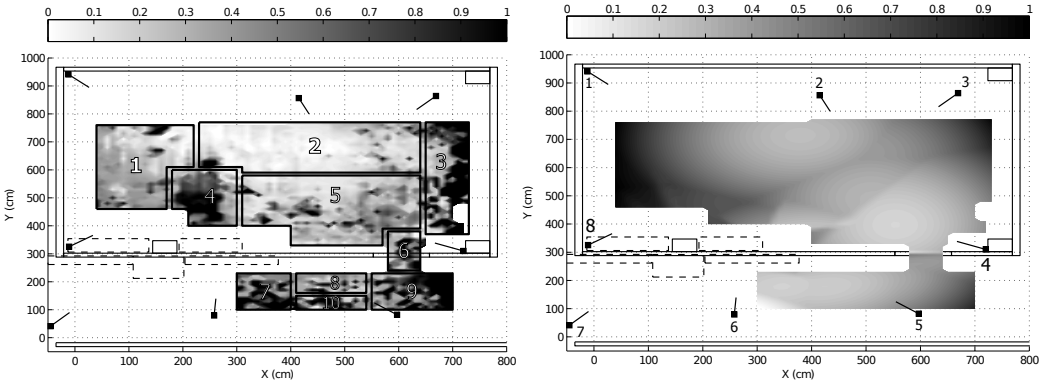

(a) Segmented normalized average error

(b) RF Range

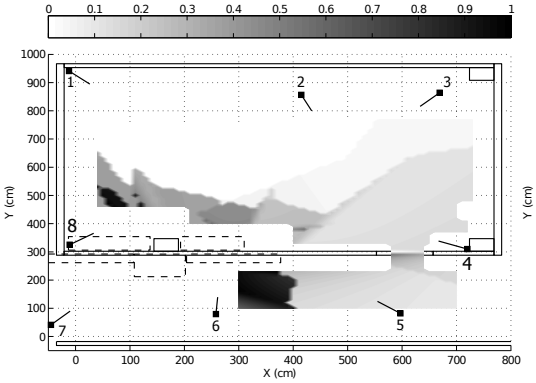

(c) Through-wall distance

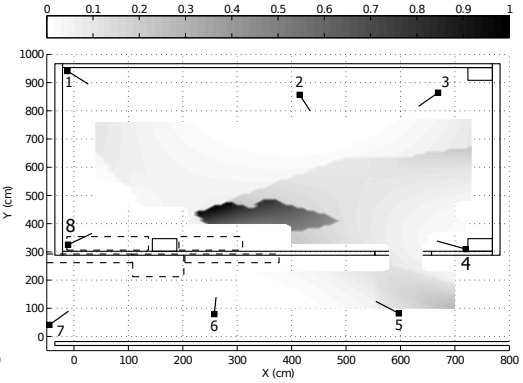

(d) PDOP

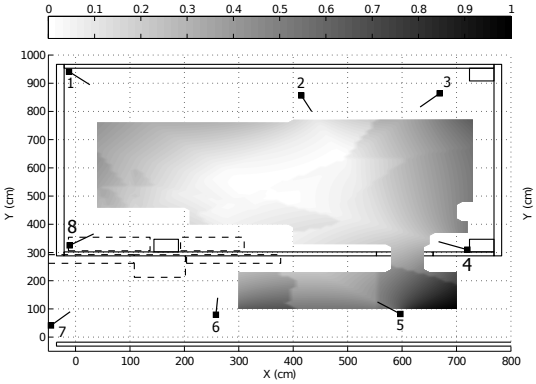

(e) Yaw angle

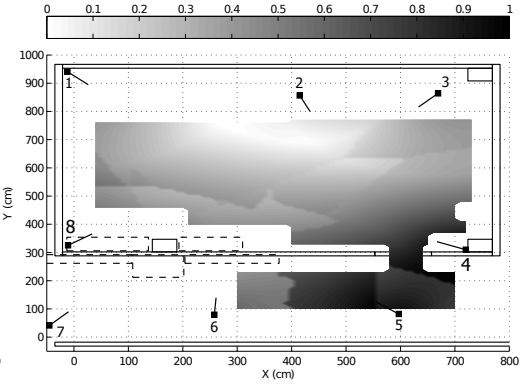

(f) Pitch angle

Figure 4.11: Summary plots of all metrics considered in this work along with the the segmented plot of normalized average measurement error.

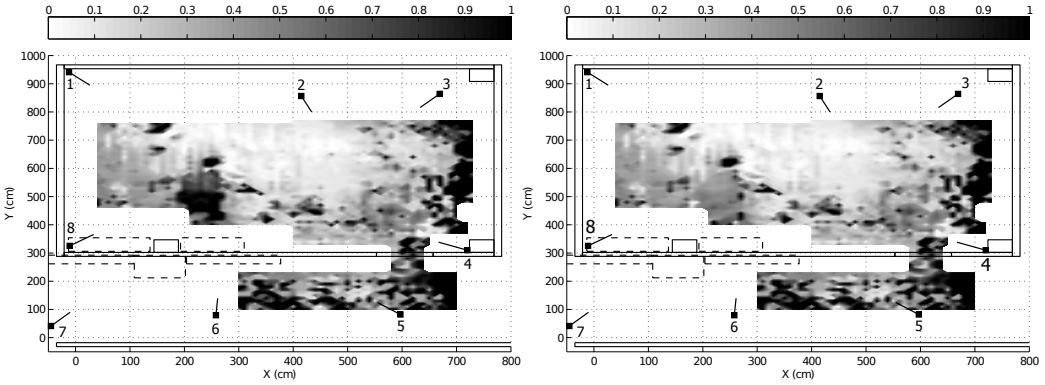

(a) Original normalized average error plot (b) New normalized average error plot

Figure 4.12: Plots of normalized average measurement error before and after correcting for a sensor calibration error.

normalized average error plot at each location within the test facility before and after correcting for the calibration error. It can be seen from this figure that the measurement error of segment 4 has been lowered although it is still of average quality.

Because each of the metrics appears to contribute to variance in measurement error in some part of the test facility, a combined metric, m_c, is desired to take advantage of the information that each metric provides. This metric is calculated using a weighted sum of each of the metrics as shown in Equation 4.10.

$$m_c = k_1\tilde{r}_c + k_2 d_{tw,c} + k_3 PDOP_c + k_4 \Upsilon_c + k_5 \rho_c \tag{4.10}$$

The set of optimal weight values, $\{k_1, k_2, k_3, k_4, k_5\}$, was selected using Equation 4.11 where e_{avg} is the average error at location (x, y) cm. This gives the optimal set of weights to minimize the difference between the normalized average error and the combined metric. Using a brute force approach to searching the space, the optimal set of weights was found to be $k_i = \{0.40, 0.85, 0.70, 0.05, 0.20\}$. The search space was a range from 0 to 1 in increments of 0.05 for all of $\{k_1, k_2, k_3, k_4, k_5\}$. Figure 4.13b shows the combined metric using the optimal weight values. It can be seen from this figure and the optimal weight values that each of the metrics is represented in the final combined metric. As can be seen by comparing Figures 4.12a and 4.12b, the combined

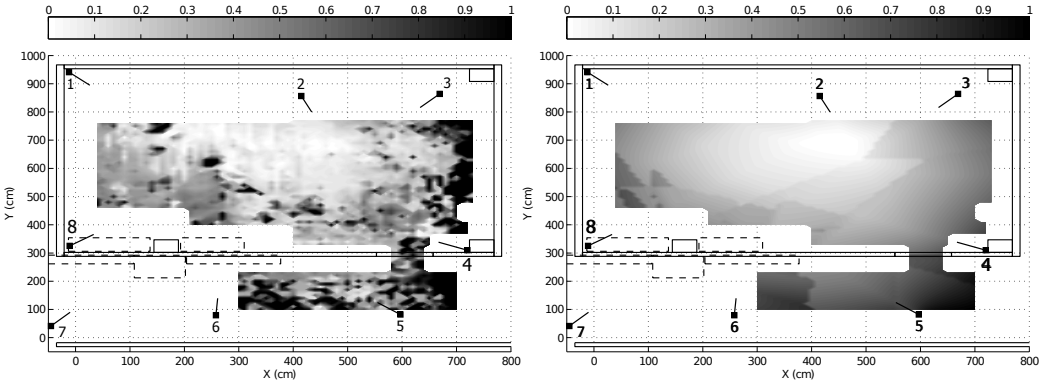

(a) New normalized average error plot

(b) Normalized combined error metric

Figure 4.13: Plots of the new normalized average measurement error and the normalized combined metric for the Riggs facility.

metric matches favorably with the actual observed measurement error.

$$\underset{\{k_1,k_2,k_3,k_4,k_5\}}{\operatorname{argmin}} \sum_x \sum_y |e_{avg} - m_c| \tag{4.11}$$

4.6 Parameter Optimization

Using the combined metric discussed in Section 4.5 and detailed in Equation 4.10, an optimal set of system configuration parameters can be determined. The parameters will be optimal in terms of producing a minimum total value for the combined metric at all locations of interest within the Riggs facility. The system configuration parameters that impact the combined metric are based on sensor placement, sensor orientation and facility floorplan, i.e. NLOS conditions. In this case, the Riggs facility floorplan is fixed and cannot be optimized. Furthermore, sensor location is restricted due to physical mounting limitations. Therefore, the only system configuration parameters that will be varied are the sensor pitch and yaw angles. It is important to note that this process could be used to determine optimal sensor placement as well as orientation.

By varying only the sensor yaw and pitch angles, the problem of determining the optimal system configuration parameters becomes a search of a 16 dimensional space including the yaw and pitch angles for all eight sensors installed within the facility. The goal of the search is to find the set of sensor yaw and pitch angles that produces the minimum value of the combined metric. This

problem is computationally restrictive to complete via a brute force approach for even a coarse resolution of angles. Therefore, a genetic algorithm has been implemented to determine the best sensor orientation parameters. Genetic algorithms take cues from evolution to solve problems on a computer [88]. Our problem is function optimization which requires minimizing the combined metric over a set of 16 sensor orientation input parameters. A genetic algorithm begins by specifying a set of C parameters referred to collectively as a chromosome. In our problem there are 16 elements in each chromosome. Then, an initial set of N chromosomes is generated in some manner, typically randomly. Our implementation generates 10,000 chromosomes and initializes each element randomly with a uniformly distributed random variable. Table 4.3 gives the range of acceptable values used for each element of a chromosome.

Table 4.3: Range of acceptable values for pitch and yaw (degrees).

	Sensor							
	1	2	3	4	5	6	7	8
Minimum Yaw	-90	-180	-180	90	0	0	0	-90
Maximum Yaw	0	0	0	270	180	180	90	90
Minimum Pitch	-90	-90	-90	-90	-90	-90	-90	-90
Maximum Pitch	0	0	0	0	0	0	0	0

A set of chromosomes is referred to as a population. A measure of fitness is then calculated for each chromosome. The appropriate fitness measure is highly problem-specific. In our genetic algorithm implementation, the combined metric described in Section 4.5 is used as the fitness measure. In this case, the most fit members of the population will have the lowest fitness score. The terms "most fit" and "optimal" will be used interchangeably.

At this point, the next generation population is created through the use of two evolutionary mechanisms: selection (crossover) and mutation. Selection requires choosing two members of the population to mate and produce offspring. Analogous to "natural selection" the most fit members of the population will reproduce more often [89]. Although each chromosome has the possibility of reproducing, chromosomes with higher fitness scores are selected more frequently. This is often referred to as roulette-wheel or fitness proportionate selection. Crossover is part of the reproduction process where elements of the chromosomes of two parents are swapped creating two new child chromosomes [89]. In our implementation, crossover occurs in 70% of reproductions, i.e. a crossover rate of 0.7, and crossover occurs at a randomly selected element within the parent chromosomes.

Also a part of reproduction is chromosome mutation. Mutation is an evolutionary mechanism that maintains diversity by randomly changing an element of a chromosome. However, this process occurs infrequently. In our implementation, the mutation rate is 0.001. Mutation is performed by randomly re-initializing selected chromosomes with a uniformly distributed random variable, again according to the limits shown in Table 4.3. The selection (crossover) and mutation processes are repeated until a new population of size N is created. A new generation has now been created. The entire process is repeated with the new generation starting with calculation of the fitness measure. Many different methods exist to determine when the iteration process should complete, i.e. the algorithm has converged. In our implementation, the process is simply run for 200 generations. The C implementation of this algorithm developed for this work took approximately 250 minutes to evolve through 200 generations of chromosomes. The chromosome with the lowest fitness score in the final generation is chosen as the optimal solution. Figure 4.14 shows the evolution of the average and minimum fitness scores for our genetic algorithm implementation. It can be seen that both the mean and minimum fitness scores steadily decrease. Table 4.4 shows the values of yaw and pitch angle found to be optimal by the genetic algorithm.

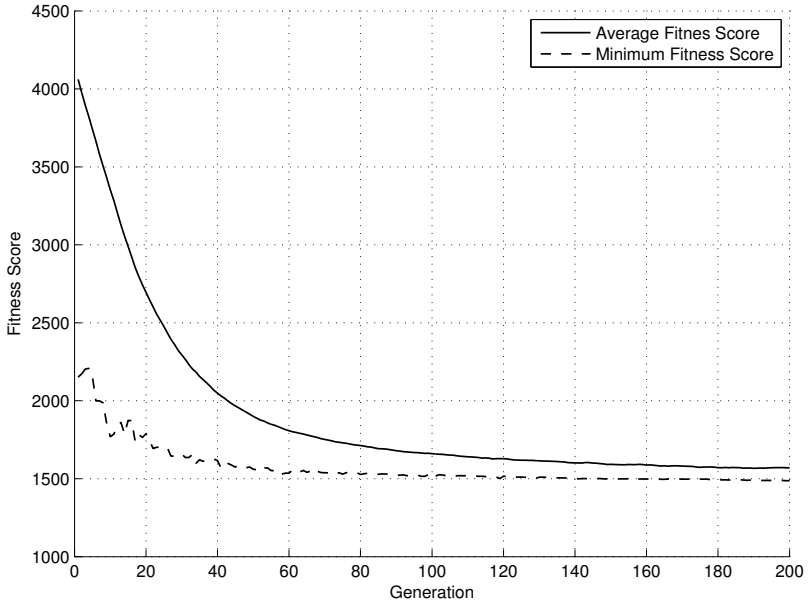

Figure 4.14: Trajectory of the genetic algorithm fitness score for 200 generations. The number of chromosomes is set to 10,000 with a crossover rate of 0.7 and a mutation rate of 0.001. Mutation is performed using uniform mutation. The chromosomes are randomly initialized.

Table 4.4: Pitch and yaw angles found to be optimal by the genetic algorithm (degrees).

Sensor	**1**	**2**	**3**	**4**	**5**	**6**	**7**	**8**
Proposed Yaw	-46.6	-87.1	-123.0	146.8	101.1	49.9	14.3	39.5
Proposed Pitch	-22.6	-30.9	-26.8	-28.0	-29.0	-25.9	-21.8	-25.0

Using the optimal parameters found by the genetic algorithm, the combined metric can be recalculated across the test facility. Figure 4.15 shows the combined, total yaw and total pitch metrics for the current system configuration on the left side and the same metrics for the optimal parameters on the right. It can be seen from these figures that the minimum area for the combined metric has shifted more towards the center of the facility. Furthermore, the sum of the combined metric has been reduced from 2250 to 1519 or by more than 30%. The total yaw metric figures show how the area with minimum total yaw has been significantly increased in size. The total pitch metric figures show a significant overall reduction in the total pitch metric across the facility as well as shift in the minimum value area towards the center of the facility.

4.7 Verification

The output of the genetic algorithm is a set of sensor orientation angles that gives a minimum value for the combined metric that has been developed. In order to verify that an overall reduction in the combined metric across the test facility will result in reduced measurement error in a real world installation of the UWB positioning system, the physical sensor orientations of the system installed in the test facility need to be changed to match as closely as possible the sensor orientation angles that were output from the genetic algorithm. Table 4.5 gives the sensor orientation angles for the current system configuration, the sensor orientation angles output by the genetic algorithm (proposed) and the sensor orientation angles for the new system configuration. The angles do not match exactly due to physical constraints of the system install. However, great care was taken to get the angles as close as possible to the optimal result.

After adjusting the sensor orientation angles, new data was collected in locations spread throughout the test facility. Data was re-collected at 90 locations within the test facility. Figure 4.16 shows the locations where data was re-collected. The average error for these locations in the original data collection was found to be 47 cm. The average error for these locations in the new

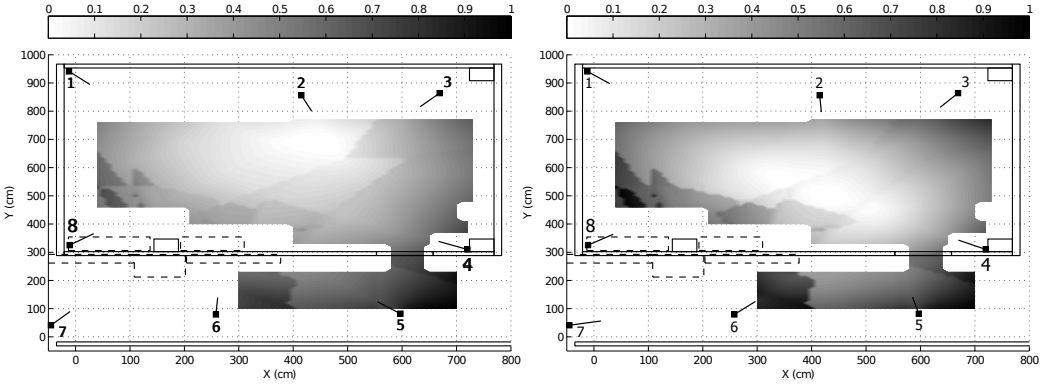

(a) Current combined metric

(b) Proposed combined metric

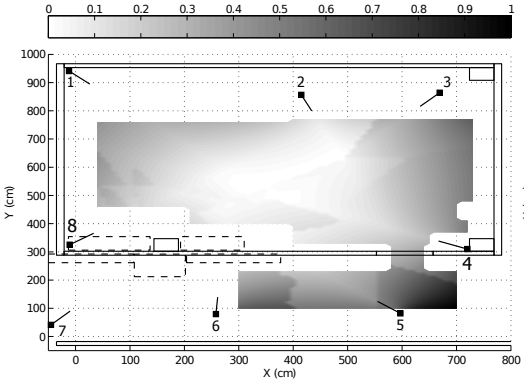

(c) Current total yaw

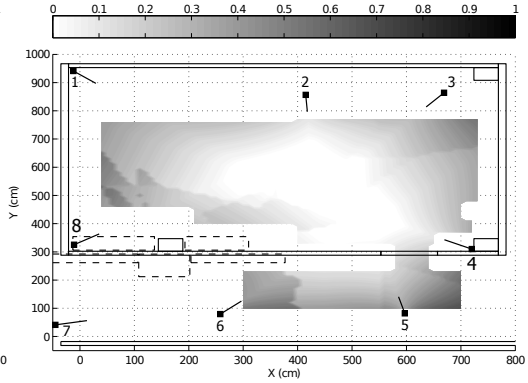

(d) Proposed total yaw

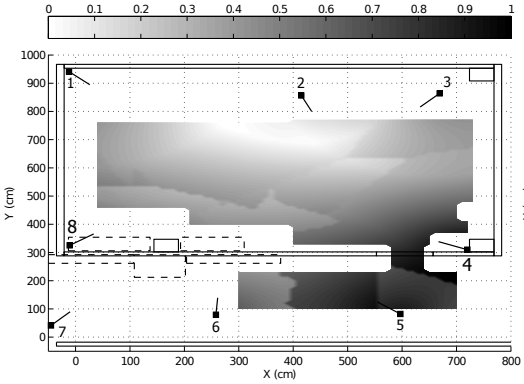

(e) Current total pitch

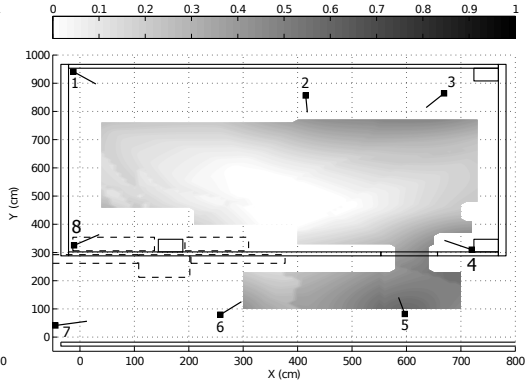

(f) Proposed total pitch

Figure 4.15: Combined metric, total yaw and total pitch for current system setup (left) and proposed configuration (right).

Table 4.5: Pitch and yaw angles for current and proposed system configuration (degrees).

Sensor	1	2	3	4	5	6	7	8
Current Yaw	-50.4	-71.5	-126.6	151.9	134.7	87.0	54.1	42.4
Proposed Yaw	-46.6	-87.1	-123.0	146.8	101.1	49.9	14.3	39.5
New Yaw	-44.6	-86.8	-123.6	138.9	94.3	53.9	21.2	42.1
Current Pitch	-28.7	-53.0	-36.7	-17.8	-14.4	-24.8	-27.7	-16.3
Proposed Pitch	-22.6	-30.9	-26.8	-28.0	-29.0	-25.9	-21.8	-25.0
New Pitch	-18.1	-29.5	-30.7	-23.2	-23.2	-28.2	-20.7	-21.0

data collection after sensor orientation adjustment was found to be 21 cm. This is a reduction in measurement error of approximately 55%. Of the 90 locations re-surveyed, 75 were found to have a lower average error than in the initial system configuration. Figure 4.17 is a histogram of the change in average error from the original configuration to the optimized configuration, i.e. original error value - new error value. It can be seen from this figure that most of the locations, specifically 60 out of the 90, have a positive change in error between 0 and 50 cm which corresponds to a decrease in average error after sensor orientation optimization.

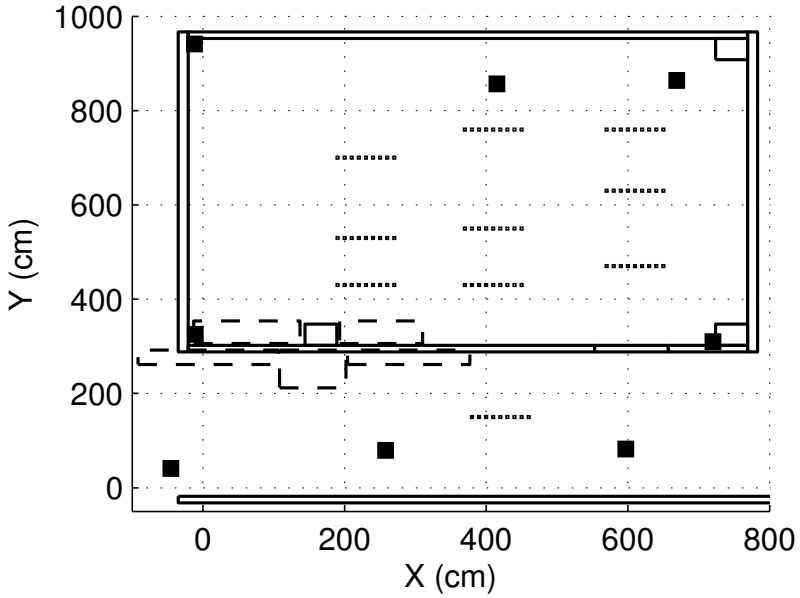

Figure 4.16: Locations of data re-collection for comparison to previous system configuration.

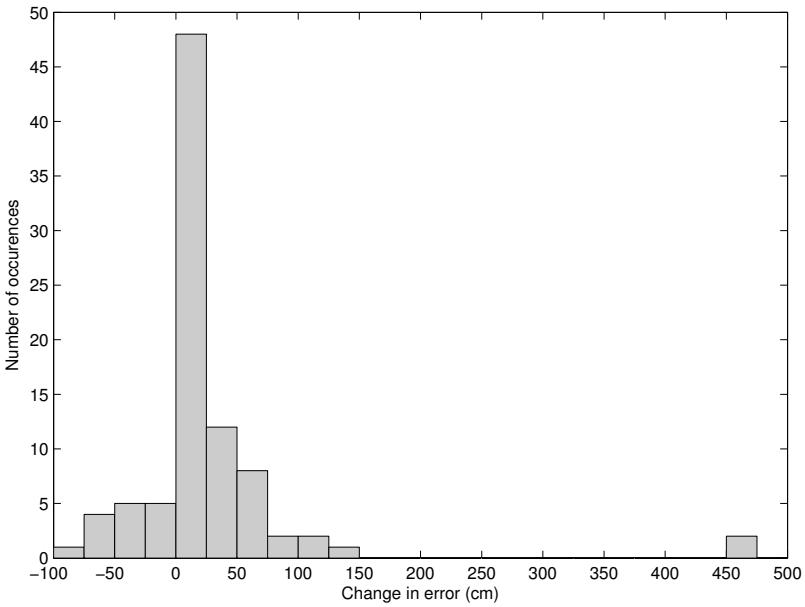

Figure 4.17: Histogram of the change in error from the original system configuration to the optimized configuration.

4.8 Optimization Conclusions

In this chapter, a combined metric was developed using a weighted sum of a set of five individual metrics. These metrics are calculated based on sensor location, sensor orientation and facility floorplan. The combined metric was designed to match the average measurement error that was found in the initial data collection. A genetic algorithm was then implemented to determine the optimum sensor orientation angles to reduce the combined metric value. To verify that the combined metric corresponds to measurement error, the physical installation of the UWB positioning system within the Riggs facility was adjusted to closely match the output angles of the genetic algorithm. The average measurement error was then recalculated at a sampling of locations throughout the test facility and a 55% reduction was found.

It is important to note that, although the genetic algorithm presented in this chapter was used to optimize only the orientation angles, the algorithm could be expanded to search for optimal sensor placement as well. This would increase the search space of the algorithm significantly but the algorithm should still be able to achieve an optimal sensor configuration without a significant increase in run time of the algorithm. Furthermore, it is mentioned that this algorithm is set up such that it optimizes sensor orientation for the specific locations that are considered. An extension of

this would be using the algorithm to prioritize areas within a facility that the system *must* perform as accurately as possible. In this case, sensor placement and orientation would be geared towards minimizing the combined error metric in the high priority areas at the expense of other areas within the facility.

Chapter 5

Conclusions

This work presents a study of the environment noise in a real world installation of an UWB indoor position tracking system. Through two measurement campaigns, measurement noise in such a system has been shown to be location dependent and multi-modal. To account for this multi-modality, noise at a specific location is modeled using a sum of Gaussians. Evidence has been shown that the measurement noise is stable over time and locally similar.

Using data from the Riggs facility, a method is presented for integrating a map of UWB measurement noise into a particle filter framework to improve indoor position tracking accuracy. A 15% reduction in tracking error is shown through the use of the measurement noise map in the context of a particle filter.

Finally, a metric for measurement accuracy based on sensor location, sensor orientation and facility floorplan was developed. The metric was designed to reflect the expected quality of measurements that will be found at locations within a facility. It was found that the metric produced a map that matched well against the manual observation of measurement noise throughout the Riggs facility. A genetic algorithm was then implemented to improve the system configuration. Specifically, the genetic algorithm determined the optimum sensor orientation angles by minimizing the overall metric value. Finally, the utility of the metric was verified by adjusting the sensor orientation angles to closely match the output angles of the genetic algorithm and re-collecting data in a smaller subset across the facility. The average measurement error was found to have been reduced by 55%.

5.1 Recommendations for Future Work

This research leaves many open questions related to the improvement of UWB indoor position tracking. The author believes that augmentation of UWB local positioning systems is a fertile area of future research. For example, data from devices such as laser detection and ranging (LADAR) systems could be used to create a sort of differential local positioning system analogous to differential GPS systems that are currently in use.

A limitation of our map aided particle filtering method is the requirement that the measurement noise map be re-calculated after a significant change to the positioning system installation or environment occurs. Because of this, it is expected that this type of map would be generated for a system once and used for a long period of time. Furthermore, the author acknowledges that a significant time commitment is required to generate the measurement noise map. The development of more automated methods to generate the measurement noise map could significantly reduce this time commitment and allow for the measurement noise model to be recalculated on a more frequent basis if necessary. It may be that floor plan and sensor geometry information could be used to semi-automate this process similar to the techniques shown in [53, 73].

It would be valuable to expand the genetic algorithm to search for the most fit sensor locations along with sensor orientation. In this work, the sensor locations were limited due to facility constraints. Optimizing not only sensor orientation but also position will lead to the best possible facility-wide install. It is worth noting that the combined metric used can be tailored such that areas that are of high priority can be can be configured to have the lowest possible metric value in that area which will lead to lower values of average error in that area. However, other areas will likely suffer from higher measurement error.

The applications of local positioning systems specifically those intended to function indoors are increasing with increases in system accuracies. Highly accurate systems ($<$ 1mm accuracy) have already been developed that function in controlled situations and are used in surgical applications [90]. This system is highly accurate but also functions in a highly controlled environment. More robust systems, such as the one used in this work, have yet to achieve such high accuracy. Other applications include telepresence and entertainment systems. A number of entertainment systems such as Microsoft's Kinect, the Nintendo Wii^{TM} have been developed that use motion to perform actions within a virtual world. With increased accuracy, UWB indoor positing tracking systems

could be used in a similar manner.

NLOS and multipath conditions will continue to impact the performance of indoor positioning systems. More sophisticated methods that counteract these situations will be needed to make systems more robust to these types of errors and to improve general system accuracies to the 1 cm level. Further work into modeling the effects of various building materials on UWB signals such as that presented in [15] could lead to higher indoor accuracy indoor.

Bibliography

[1] W. Suski, S. Banerjee, and A. Hoover, "System-level noise of an ultra-wideband tracking system," Dec. 2012, accepted for publication at the *Int'l Conf. on Information Science, Signal Processing and their Applications*.

[2] N. Samama, *Global Positioning: Technologies and Performance*. Wiley-Interscience, 2008.

[3] W. Lechner and S. Baumann, "Global navigation satellite systems," *Computers and Electronics in Agriculture*, vol. 25, pp. 67 – 85, 2000.

[4] M. Grewal, L. Weill, and A. Andrews, *Global Positioning Systems, Inertial Navigation, and Integration*. Wiley-Interscience, 2007.

[5] E. Kaplan and C. Hegarty, *Understanding GPS: Principles and Applications*, 2nd ed. Artech House, 2005.

[6] B. Parkinson and J. S. Jr., Eds., *Global Positioning System: Theory and Applications*. American Institute of Aeronautics and Astronautics, Inc., 1996, vol. 164.

[7] O. Shimizu, K. Tenmoku, Y. Doi, and K. Mito, "Vehicle location detecting system," U.S. Patent 5,119,301, June 2, 1992.

[8] B. Davies, "Satellite based on-board vehicle navigation system including predictive filtering and map-matching to reduce errors in a vehicular position," U.S. Patent 6,615,135 B2, September 2, 2003.

[9] S. Taghipour, M. Meybodi, and A. Taghipour, "An algorithm for map matching for car navigation system," in *3rd Int'l Conf. on Information and Communication Technologies: From Theory to Applications*, April 2008, pp. 1 – 5.

[10] H. Liu, H. Darabi, P. Banerjee, and J. Liu, "Survey of wireless indoor positioning techniques and systems," *IEEE Trans. on Systems, Man, and Cybernetics, Part C: Applications and Reviews*, vol. 37, no. 6, pp. 1067 – 1080, 2007.

[11] D. Ganjali, "Filtering noise caused by sensor selection for an ultra-wide band position tracking system," Master's thesis, Clemson University, 2009.

[12] R. Kyker, "Local positioning system," in *Proc. of WESCON*, 1995, pp. 756 – 761.

[13] FCC, "Revision of part 15 of the commissions rules regarding ultra-wideband transmission systems," Report and order, adopted February 14, 2002, released July 15, 2002.

[14] L. Yang and G. B. Giannakis, "Ultra-wideband communications: An idea whose time has come," *IEEE Signal Processing Magazine*, vol. 21, pp. 26 – 54, November 2004.

[15] J. Lee and S. Choi, "Through-material propagation characteristic and time resolution of uwb signal," in *Int'l Workshop on Ultra Wideband Systems*, May 2004, pp. 71 – 75.

[16] M. Win and R. Scholtz, "On the robustness of ultra-wide bandwidth signals in dense multipath environments," *IEEE Communications Letters*, vol. 2, no. 2, pp. 51–53, February 1998.

[17] "Ubisense series 7000 sensor fact sheet," Ubisense Inc., January 2011. [Online]. Available: http://www.ubisense.net/en/resources/factsheets/series-7000-sensor.html

[18] Zebra Enterprise Solutions, "Dart UWB hub & sensors," January 2011. [Online]. Available: http://zes.zebra.com/index.js

[19] "Plus system datasheet," Time Domain, May 2011. [Online]. Available: http://www.plus-ls.com/datasheets/plus-system.php

[20] "UWB precise positioning," Thales Research and Technology (UK) Ltd, May 2011. [Online]. Available: http://www.thalesresearch.com/Capabilities/Navigation/Pages/Indoor%20Positioning.aspx

[21] M. Mahfouz, C. Zhang, B. Merkl, M. Kuhn, and A. Fathy, "Investigation of high-accuracy indoor 3-D positioning using UWB technology," *IEEE Trans. on Microwave Theory and Techniques*, vol. 56, no. 6, pp. 1316 – 1330, 2008.

[22] C. Zhang, M. Kuhn, B. Merkl, A. Fathy, and M. Mahfouz, "Real-time noncoherent UWB positioning radar with millimeter range accuracy: Theory and experiment," *IEEE Trans. on Microwave Theory and Techniques*, vol. 58, no. 1, pp. 9 – 20, 2010.

[23] D. Yang, A. Fathy, H. Li, M. Mahfouz, and G. Peterson, "Millimeter accuracy UWB positioning system using sequential sub-sampler and time difference estimation algorithm," in *Proc. of the IEEE Radio and Wireless Symposium*, 2010.

[24] Z. Low, J. Cheong, C. Law, W. Ng, and Y. Lee, "Pulse detection algorithm for line-of-sight (LOS) UWB ranging applications," *IEEE Antennas and Wireless Propagation Letters*, vol. 4, pp. 63 – 67, 2005.

[25] J. Yan, C. Tiberius, P. Teunissen, G. Bellusci, and G. Janssen, "A framework for low complexity least-squares localization with high accuracy," *IEEE Trans. on Signal Processing*, vol. 58, no. 9, pp. 4836 – 4847, 2010.

[26] R. Fontana, E. Richley, and J. Barney, "Commercialization of an ultra wideband precision asset location system," in *Proc. of the IEEE Conf. on Ultra Wideband Systems and Technologies*, 2003, pp. 369 – 373.

[27] Z. Guoping and S. Rao, "Position localization with impulse ultra wide band," in *Proceedings of the IEEE/ACES Int'l Conf. on Wireless Communications and Applied Computational Electromagnetics*, 2005, pp. 17 – 22.

[28] B. Waldmann, R. Weigel, and P. Gulden, "Method for high precision local positioning radar using an ultra wideband technique," in *IEEE MTT-S Int'l Microwave Symposium Digest*, 2008, pp. 117 – 120.

[29] B. Waldmann, A. Goetz, and R. Weigel, "An ultra wideband positioning system enhanced by a short multipath mitigation technique," in *Proceedings of the IEEE MTT-S Int'l Microwave Workshop on Wireless Sensing, Local Positioning, and RFID*, 2009, pp. 1 – 4.

[30] C. Correal, S. Kyperountas, Q. Shi, and M. Welborn, "An UWB relative location system," in *Proc. of the IEEE Conf. on Ultra Wideband Systems and Technologies*, 2003, pp. 394 – 397.

[31] R. Zetik, J. Sachs, and R. Thomä, "UWB localization - active and passive approach," in *Proc. of the IEEE Instrumentation and Measurement Technology Conf.*, 2004, pp. 1005 – 1009.

[32] C. Meier, A. Terzis, and S. Lindenmeier, "A robust 3D high precision radio location system," in *Proc. of the IEEE Int'l Microwave Symposium*, 2007, pp. 397 – 400.

[33] M. Oh, J. Park, and J. Kim, "IR-UWB packet-based precise ranging system for u-home networks," *IEEE Trans. on Consumer Electronics*, vol. 55, pp. 119 – 125, 2009.

[34] G. MacGougan, K. O'Keefe, and R. Klukas, "Tightly-coupled GPS/UWB integration," *Journal of Navigation*, vol. 63, no. 1, pp. 1 – 22, 2010.

[35] C. Steiner and A. Wittneben, "Low complexity location fingerprinting with generalized UWB energy detection receivers," *IEEE Trans. on Signal Processing*, vol. 58, no. 3, pp. 1756 – 1767, March 2010.

[36] B. Denis, L. Ouvry, B. Ulguen, and F. Tchoffo-Talom, "Advanced Bayesian filtering techniques for UWB tracking systems in indoor environments," in *Proc. of the IEEE Int'l Conf. on Ultra-wideband*, 2005, pp. 638 – 643.

[37] M. Jing, Z. Nai-tong, and Z. Qin-yu, "IR-UWB waveform distortion analysis in NLOS localization system," *Information Technology Journal*, pp. 139 – 145, 2010.

[38] W. Chung and D. Ha, "An accurate ultra wideband (UWB) ranging for precision asset location," in *Proc. of the Int'l Conf. on Ultra Wideband Systems and Technologies*, 2003, pp. 389 – 393.

[39] G. Shen, R. Zetik, O. Hirsch, and R. Thomä, "Range-based localization for UWB sensor networks in realistic environments," *EURASIP Journal on Wireless Communications and Networking*, 2010.

[40] C. Morelli, M. Nicoli, V. Rampa, and U. Spagnolini, "Hidden markov models for radio location in mixed LOS/NLOS conditions," *IEEE Trans. on Signal Processing*, vol. 55, no. 4, pp. 1525 – 1542, 2007.

[41] K. Yu and I. Oppermann, "Performance of UWB position estimation based on time-of-arrival measurements," in *Proceedings of the Int'l Workshop on Ultra Wideband Systems*, 2004, pp. 400 – 404.

[42] G. Welch and G. Bishop, "An introduction to the kalman filter," UNC-Chapel Hill, Tech. Rep. TR95-041, November 2000.

[43] R. Kalman, "A new approach to linear filtering and prediction problems," *Transactions of the ASME–Journal of Basic Engineering*, vol. 82, no. Series D, pp. 35 – 45, 1960.

[44] G. Welch and G. Bishop, "An introduction to the Kalman filter," Department of Computer Science, University of North Carolina at Chapel Hill, Tech. Rep. TR 95-041, 2006.

[45] S. Julier and J. Uhlman, "Unscented filtering and nonlinear estimation," *Proc. of the IEEE*, vol. 92, no. 3, pp. 401 – 422, 2004.

[46] P. Djuric, J. Kotecha, J. Zhang, Y. Huang, T. Ghirmai, M. Bugallo, and J. Miquez, "Particle filtering," *IEEE Signal Processing Magazine*, Sept. 2003.

[47] J. S. Liu, R. Chen, and T. Logvinenko, "A theoretical framework for sequential importance sampling and resampling," in *Sequential Monte Carlo in Practice*, A. Doucet, N. de Freitas, and N. Gordon, Eds. Springer-Verlag, Jan. 2001.

[48] I. M. Rekleitis, "A particle filter tutorial for mobile robot localization," Centre for Intelligent Machines, McGill University, Tech. Rep. TR-CIM-04-02, 2002.

[49] N. Patwari, J. Ash, S. Kyperountas, A. H. III, R. Moses, and N. Correal, "Locating the nodes," *IEEE Signal Processing Magazine*, vol. 22, no. 4, pp. 54 – 69, July 2005.

[50] A. Sayed, A. Tarighat, and N. Khajehnouri, "Network-based wireless location," *IEEE Signal Processing Magazine*, vol. 22, no. 4, pp. 24 – 40, July 2005.

[51] D. Dardari, A. Conti, U. Ferner, A. Giorgetti, and M. Z. Win, "Ranging with ultrawide bandwidth signals in multipath environments," *Proceedings of the IEEE*, vol. 97, no. 2, pp. 404 – 426, February 2009.

[52] R. Ye, S. Redfield, and H. Liu, "High-precision indoor UWB localization: Technical challenges and method," in *IEEE Int'l Conference on Ultra-Wideband*, September 2010, pp. 1 – 4.

[53] M. Nicoli, C. Morelli, and V. Rampa, "A jump markov particle filter for localization of moving terminals in multipath indoor scenarios," *IEEE Trans. on Signal Processing*, vol. 56, no. 8, pp. 3801 – 3809, August 2008.

[54] J. Youssef, B. Denis, C. Godin, and S. Lesecq, "Enhanced UWB indoor tracking through NLOS TOA biases estimation," in *IEEE Global Telecommunications Conference*, December 2008, pp. 1 – 5.

[55] ——, "Enhanced linearized location estimators with optimization-based combinations of radiolocation measurements," in *IEEE 20th Int'l Symposium on Personal, Indoor and Mobile Radio Communications*, September 2009, pp. 2055 – 2059.

[56] A. Giremus, J.-Y. Tourneret, and V. Calmettes, "A particle filtering approach for joint detection/estimation of multipath effects on GPS measurements," *IEEE Trans. on Signal Processing*, vol. 55, no. 4, pp. 1275 – 1285, April 2007.

[57] B. Denis, J.-B. Pierrot, and C. Abou-Rjeily, "Joint distributed synchronization and positioning in UWB *Ad Hoc* networks using TOA," *IEEE Trans. on Microwave Theory and Techniques*, vol. 54, no. 4, pp. 1896 – 1911, April 2006.

[58] Y. Qi, H. Kobayashi, and H. Suda, "Analysis of wireless geolocation in a non-line-of-sight environment," *IEEE Trans. on Wireless Communications*, vol. 5, no. 3, pp. 672 – 681, March 2006.

[59] A. Elkins, E. Muth, A. Hoover, A. Walker, T. Carpenter, and F. Switzer, "Physiological compliance and team performance," *Applied Ergonomics*, vol. 40, pp. 997 – 1003, 2009.

[60] A. Hoover and E. Muth, "Instrumenting for measuring," in *The PSI Handbook of Virtual Environments for Training and Education.* Praeger Security International Publishing, 2008, vol. 3, pp. 184 –195.

[61] C. Brown. (2010, April) Real-time location of jena's buses and trams with ubisense RTLS. [Online]. Available: http://www.ubisense.net/en/news-and-events/press-releases/real-time-location-of-jenas-buses-and-trams-with-ubisense-rtls.html

[62] "Ubisense precise location," Ubisense Inc., May 2011. [Online]. Available: http://www.ubisense.net/en/resources/factsheets/ubisense-precise-location.html

[63] *LocationEngineConfig User Manual*, Ubisense Inc., 2008.

[64] H. Sorenson and D. Alspach, "Recursive Bayesian estimation using Gaussian sums," *Automatica*, vol. 7, pp. 465 – 479, 1971.

[65] J. Kotecha and P. Djurić, "Gaussian sum particle filtering," *IEEE Trans. on Signal Processing*, vol. 51, no. 10, pp. 2602 – 2612, October 2003.

[66] M. Ester, H. Kriegel, J. Sander, and X. Xu, "A density-based algorithm for discovering clusters in large spatial databases with noise," in *Proc. of the 2nd Int'l Conf. on Knowledge Discovery and Data Mining*, 1996, pp. 226 – 231.

[67] S. Arulampalam, S. Maskell, N. Gordon, and T. Clapp, "A tutorial on particle filters for online nonlinear/non-Gaussian Bayesian tracking," *IEEE Trans. on Signal Processing*, vol. 50, no. 2, pp. 174 – 188, February 2002.

[68] A. Doucet, S. Godsill, and C. Andrieu, "On sequential Monte Carlo sampling methods for Bayesian filtering," *Statistics and Computing*, vol. 10, no. 3, pp. 197 – 208, 2000.

[69] F. Gustafsson, F. Gunnarsson, N. Bergman, U. Forssell, J. Jansson, R. Karlsson, and P.-J. Nordlund, "Particle filters for positioning, navigation, and tracking," *IEEE Trans. on Signal Processing*, vol. 50, no. 2, pp. 425 – 437, February 2002.

[70] R. Karlsson and F. Gustafsson, "Bayesian surface and underwater navigation," *IEEE Trans. on Signal Processing*, vol. 54, no. 11, pp. 4204 – 4211, November 2006.

[71] P. Davidson, J. Collins, and J. Takala, "Application of particle filters for indoor positioning using floor plans," in *IEEE Int'l Conf. and Exhibition on Ubiquitous Positioning, Indoor Navigation, and Location Based Service*, October 2010, pp. 1 – 4.

[72] C. Nerguizian, C. Despins, and S. Affès, "Geolocation in mines with an impulse response fingerprinting technique and neural networks," *IEEE Trans. on Wireless Communications*, vol. 5, no. 3, pp. 603 – 611, March 2006.

[73] T. Roos, P. Myllymaki, and H. Tirri, "A statistical modeling approach to location estimation," *IEEE Trans. on Mobile Computing*, vol. 1, no. 1, pp. 59 – 69, 2002.

[74] D. Jourdan, D. Dardari, and M. Win, "Position error bound for UWB localization in dense cluttered environments," in *IEEE Int'l Conf. on Communications*, June 2006, pp. 3705 – 3710.

[75] ——, "Position error bound and localization accuracy outage in dense cluttered environments," in *IEEE 2006 Int'l Conf. on Ultra-Wideband*, September 2006, pp. 519 – 524.

[76] ——, "Position error bound for uwb localization in dense cluttered environments," *IEEE Trans. on Aerospace and Electronic Systems*, vol. 44, no. 2, pp. 613 – 628, April 2008.

[77] D. Jourdan and N. Roy, "Optimal sensor placement for agent localization," *ACM Transactions on Sensor Networks*, vol. 4, no. 3, May 2008.

[78] S. Martínez and F. Bullo, "Optimal sensor placement and motion coordination for target tracking," *Automatica*, vol. 42, no. 4, pp. 661 – 668, 2006.

[79] A. Sinha, T. Kirubarajan, and Y. Bar-Shalom, "Optimal cooperative placement of GMTI UAVs for ground target tracking," in *Proc. of the IEEE Aerospace Conf.*, 2004, pp. 1859 – 1868.

[80] T. Hegazy and G. Vachtsevanos, "Sensor placement for isotropic source localization," in *Proc. of the 2nd Int'l Workshop on Information Processing in Sensor Networks*, April 2003.

[81] J. McKay and M. Pachter, "Geometry optimization for gps navigation," in *Proc. of the 36th Conf. on Decision and Control*, December 1997.

[82] "Series 7000 compact tag," Ubisense Inc., May 2011. [Online]. Available: http://www.ubisense.net/en/resources/factsheets/series-7000-compact-tag.html

[83] K. Sato, T. Manabe, J. Polivka, T. Ihara, Y. Kasashima, and K. Yamaki, "Measurement of the complex refractive index of concrete at 57.5 ghz," *IEEE Trans. on Antennas and Wave Propagation*, vol. 44, no. 1, pp. 35 – 40, January 1996.

[84] S. Gezici, Z. Tian, G. Giannakis, H. Kobayashi, A. Molisch, V. Poor, and Z. Sahinoglu, "Localization via ultra-wideband radios," *IEEE Signal Processing Magazine*, vol. 22, no. 4, pp. 70 – 84, July 2005.

[85] R. Langley, "Dilution of precision," *GPS World*, vol. 10, no. 5, pp. 52 – 59, May 1999.

[86] G. Dudek and M. Jenkin, *Computational Principles of Mobile Robotics*. Cambridge University Press, 2000.

[87] A. Dempster, "Dilution of precision in angle-of-arrival systems," *IEEE Electronic Letters*, vol. 42, no. 5, March 2006.

[88] S. Forrest, "Genetic algorithms: Principles of natural selection applied to computation," *Science*, vol. 261, no. 5123, pp. 872 – 878, August 1993.

[89] J. Holland, "Genetic algorithms," *Scientific American*, vol. 267, no. 1, pp. 66 – 72, July 1992.

[90] M. Mahfouz, M. Kuhn, G. To, and A. Fathy, "Integration of UWB and wireless pressure mapping in surgical navigation," *IEEE Trans. on Microwave Theory and Techniques*, vol. 57, pp. 2550 – 2564, October 2009.